



---

## PROPAGATION OF POLARIZATION MODULATED BEAMS THROUGH A TURBULENT ATMOSPHERE

TERENCE BARRETT  
BSEI

---

11/24/2014  
Final Report

DISTRIBUTION A: Distribution approved for public release.

Air Force Research Laboratory  
AF Office Of Scientific Research (AFOSR)/ RTB  
Arlington, Virginia 22203  
Air Force Materiel Command

# REPORT DOCUMENTATION PAGE

Form Approved  
OMB No. 0704-0188

Public reporting burden for this collection of information is estimated to average 1 hour per response, including the time for reviewing instructions, searching existing data sources, gathering and maintaining the data needed, and completing and reviewing this collection of information. Send comments regarding this burden estimate or any other aspect of this collection of information, including suggestions for reducing this burden to Department of Defense, Washington Headquarters Services, Directorate for Information Operations and Reports (0704-0188), 1215 Jefferson Davis Highway, Suite 1204, Arlington, VA 22202-4302. Respondents should be aware that notwithstanding any other provision of law, no person shall be subject to any penalty for failing to comply with a collection of information if it does not display a currently valid OMB control number. **PLEASE DO NOT RETURN YOUR FORM TO THE ABOVE ADDRESS.**

1. REPORT DATE (DD-MM-YYYY)		2. REPORT TYPE		3. DATES COVERED (From - To)	
4. TITLE AND SUBTITLE				5a. CONTRACT NUMBER	
				5b. GRANT NUMBER	
				5c. PROGRAM ELEMENT NUMBER	
6. AUTHOR(S)				5d. PROJECT NUMBER	
				5e. TASK NUMBER	
				5f. WORK UNIT NUMBER	
7. PERFORMING ORGANIZATION NAME(S) AND ADDRESS(ES)				8. PERFORMING ORGANIZATION REPORT NUMBER	
9. SPONSORING / MONITORING AGENCY NAME(S) AND ADDRESS(ES)				10. SPONSOR/MONITOR'S ACRONYM(S)	
				11. SPONSOR/MONITOR'S REPORT NUMBER(S)	
12. DISTRIBUTION / AVAILABILITY STATEMENT					
13. SUPPLEMENTARY NOTES					
14. ABSTRACT					
15. SUBJECT TERMS					
16. SECURITY CLASSIFICATION OF:		17. LIMITATION OF ABSTRACT	18. NUMBER OF PAGES	19a. NAME OF RESPONSIBLE PERSON	
a. REPORT	b. ABSTRACT			c. THIS PAGE	19b. TELEPHONE NUMBER (include area code)

**BSEI**  
1219 Honeysuckle Pass  
Victor, NY 14564  
(T) 585-869-5352 email: barrett506@aol.com  
POC: Terence W. Barrett, Ph.D.

**AFOSR GRANT FA9550110274 FINAL REPORT - 2014**

*Synopsis:* Atmospheric propagation losses can constitute a large fraction of the electromagnetic (EM) wave energy that is dissipated during EM beam propagation through earth's atmosphere. EM systems with short wavelengths such as lasers can lose a significant fraction of their beamed energy. It is well known that atmospheric losses arise primarily from: *turbulence*: through vorticity that causes radial and axial air density variations inside beams and result in scattering; *thermal blooming*: beam expansion from air heating; *extinction*: EM energy absorption in dense concentrations of particles (clouds, fog).

Propagation through turbulent atmospheres with minimum jitter/absorption is a major objective of the Air Force. The present models of the inner scale of turbulent/distributed volume atmospheres and the performance of adaptive optics designed to mitigate the effects of those atmospheres, are both presently inadequate, although there is ongoing effort to improve both.

The defeat/mitigation of atmospheric/ionospheric beam jitter, and beam redirection by polarization modulation (POLMOD) depends on the modulation rate/frequency,  $d\varphi/dt$ ,  $d\varphi^n / dt^n$ , or rate of phase modulation of inter-beam phase, exceeding that of molecular relaxation times of the media through which a beam passes. A polarization modulated beam is achieved by modulating the phase between two orthogonal beams that are combined. Ideally, one of the orthogonal beams of the combined beam would be independently phase modulated. In the tests reported here, a substitute method was used: two orthogonal with a wavelength offset,  $\Delta\lambda$ , were combined. The substitute method provided polarization modulation, but a limited form that is linear in phase change, with no axial (rotational) control and confined in frequency dependence to the availability of lasing lines,  $\lambda_1$  and  $\lambda_2$ , defining  $\Delta\lambda = \lambda_1 - \lambda_2$ . In other words, the substitute method is limited to linear phase modulation and the availability of lasing lines. Despite these limitations, these tests demonstrated partial and substantial mitigation of atmospheric/ionospheric beam jitter, and beam redirection.

The media substituting for the atmosphere and ionosphere were: a water vapor chamber, heated air, and static and rotated phase plates. The recording methods were either near-linear power meters or nonlinear CCD cameras. As two forms of jitter were distinguished – temporal (rapid amplitude changes over time) and spatial (i.e., changes in the pointing direction) – the two recording methods suitably addressed both independently: the power meters addressed temporal jitter recording and the cameras, spatial. A number of arbitrary beam combining methods were used, all non-optimum, as no optical beam combiners were available. No TeraHertz spectrometer was available to investigate the frequency/wavelength dependence (the  $\lambda_i$  dependence) of the results. Therefore, the frequency dependence of the results reported here is not known.

Nonetheless the results, obtained under the conditions described, indicate that POLMOD achieves partial mitigation of both kinds of jitter. In the case of temporal jitter with the medium represented by a phase plate, POLMOD reduces temporal jitter up to a maximum of 50%; and the spatial jitter up to a maximum of 33%. The partial success of mitigating jitter due to propagation through other media is also reported here.

The transmit (TX) modulation approach used in these tests to improving beam propagation through disturbed atmospheres is an alternative or an adjunct to adaptive optics. In the case of adaptive optics, *there is an accent on the spatial*. This accent on the spatial (using classical physics) may not be appropriate for laser weaponry and laser communications, *for which there is an accent on the temporal*. POLMOD is a temporal, semi-quantum approach. Whereas in astronomy and imaging, the objective is *to preserve spatial information*, in communications/weaponry the objective is *to preserve information sequence and point focus*. Whereas adaptive optics addresses *the receive side* of the channel, POLMOD/AXMOD addresses *the transmit side*. Therefore, POLMOD on the TX side offers either an alternative approach to the same problem, or can be used together with (improved) adaptive optics, on the RX side, each addressing one side of the channel.

Recently, there have been proposals to exploit photon spin angular momentum (SAM) associated with polarization, and orbital angular momentum (OAM) associated with the azimuthal phase of the complex electric field,

both for communications purposes<sup>1</sup>. POLMOD is essentially *modulated* SAM and axial modulation (AXMOD) is *modulated* OAM, but for purposes of mitigating channel/atmospheric/ionospheric effects, rather than communications. Both are made explicit in a Poincaré sphere and geometric (Clifford) algebra representation.

Section 5.0 of this report provides the evidence supporting the conclusion of this report regarding temporal and spatial jitter mitigation.

## 1.0 INTRODUCTION

## 2.0 THEORY: POINCARÉ SPHERE & BLOCH MODEL

- 2.1 POINCARÉ SPHERE
- 2.2 BLOCH MODEL
- 2.3 KOLMOGOROV TURBULENCE THEORY
- 2.4 ORBITAL ANGULAR MOMENTUM (OAM)
- 2.5 RELATIONSHIP TO ADAPTIVE OPTICS

## 3.0 MEDIA

## 4.0 LABORATORY TEST CONFIGURATIONS

## 5.0 TEST RESULTS

- 5.1 DATA ANALYSIS METHODS
- 5.2 DATA ANALYSIS

## 6.0 GEOMETRIC ALGEBRA

- 6.1 INTRODUCTION
- 6.2 KNOTTED BEAMS
- 6.3 TEMPORAL DEPENDENCE OF ANISOTROPY

## 7.0 SELF-INDUCED TRANSPARENCY (SIT), ELECTROMAGNETICALLY-INDUCED TRANSPARENCY (EIT) and POLMOD

- 7.1 SIT
- 7.2 EIT
- 7.3 POLMOD

## 8.0 REFERENCES

---

<sup>1</sup> Djordjevic and Arabaci (2010) have proposed exploitation of photon spin angular momentum (SAM) associated with polarization, and orbital angular momentum (OAM) associated with the azimuthal phase of the complex electric field (cf. Djordjevic et al, 2007; Djordjevic & Djordjevic, 2009; Djordjevic, 2011; Leach et al 2004; Gibson et al 2004; Paterson, 2005).

## 1. INTRODUCTION

A medium's susceptibility, hence the refractive index, the polarizability and the permittivity, has the attributes of a tensor (matrix) rather than a vector. In order for refraction (mediated by the real part of permittivity/dielectric constant) or absorption (mediated by the imaginary part of permittivity/dielectric constant) to occur, there must, to a degree, be a polarization compatibility or match between the refracting or absorbing medium and the incident radiation, i.e., the polarization of the refracting and absorbing medium must be approximately the same and aligned.

A finite time is necessary for the molecular constituents of a medium to become polarized by radiation-induced polarization and aligned, and then to either refract or absorb that incident radiation. It is well known that because of these mechanisms pulses of radiation short enough in time can challenge the absorption time of molecular media (the molecular relaxation time) and sometimes penetrate media normally absorbing. These effects are known as self-induced transparency (SIT) and electromagnetically induced transparency (EIT). They are both short pulse effects – see section 7.0, below.

The mitigation of atmospheric/ionospheric beam jitter, and beam redirection by polarization modulation (POLMOD) hinges on the following mechanisms:

(1) The refraction/absorption or capture of incident radiation by molecular systems of the medium/media through which the radiation passes requires a compatibility/alignment between the polarization of that radiation and the induced polarization of the systems.

(2) That alignment of the permanent and induced dipole polarization of the molecular systems with the polarization of the incident radiation is not instantaneous, but requires a response time – the dipole orientation time. Time-dependent polarization in response to an applied field is given by:

$$\mathbf{P}(t) = \epsilon_0 \int_{-\infty}^t \chi_\epsilon(t-t') \mathbf{E}(t') dt',$$

where  $\mathbf{P}$  is the polarization,  $\chi_\epsilon$  is the electric susceptibility and  $\mathbf{E}$  is the electric field. In the case of the molecular systems of interest – gases – the response frequency is in the TeraHertz ( $10^{12}$ ) range. The polarization is thus a convolution of the electric field at previous times with the time-dependent susceptibility. In the case of a permanent dipole the direction of polarization itself rotates. This rotation occurs on a timescale that depends on the torque and surrounding local viscosity of the molecules. Because the rotation is not instantaneous, dipolar polarizations lose the response to electric fields at the highest frequencies.

(3) Molecular polarizability is also frequency dependent. Electronic polarizability is present in all molecules and has a response time that is rapid ( $> 10^{14}$  s-1). The high frequency response can follow the undulations of electromagnetic radiation in the visible region and hence this response gives rise to refraction of light.

(4) Just as there is a system finite onset response time of alignment with incident polarized radiation, there is a finite offset/relaxation response time of alignment when that incident radiation is withdrawn, the frequency of which is also in the TeraHertz range.

(5) As molecular systems take a finite time to reach a preferred polarization alignment with the incident radiation and a finite time of relaxation when that preferred polarization alignment is

withdrawn, there will be a transient response to incident radiation of rapidly changing polarization, even if that radiation is not transient, but continuous.

(6) If the alignment period of the polarization of the changing incident radiation with the induced/permanent dipoles of the molecular system is short enough, there will be insufficient time for molecular absorption/refraction to occur, and mechanisms conventionally associated with medium pulse/transient-system induced transparencies will occur, even when the incident radiation is continuous.

(7) As optimum alignments of molecular dipoles with the polarization of incident radiation in a gas medium will be distributed statistically, any mitigation of absorption/refraction by the mechanism described in (6) is expected to be partial.

The central proposition of this research was that if the dwell time of the radiation in a polarization state compatible with that of a molecular system is shorter than the dipole orientation time, or the relaxation time of that system, *a form of* self-induced transparency (SIT), and/or electromagnetically induced transparency (EIT) will occur, *even although the incident radiation is constant wavelength.*

The main results of the present series of tests reported are:

- Jitter mitigation.
- Amplitude loss mitigation
- Beam pointing movement mitigation.

In the following section 2.0 a description of polarization modulated incident radiation is given in terms of the Poincaré sphere, and a description of a molecular system in terms of its molecular analog, the Bloch sphere model. The well-known Kolmogorov turbulence theory is examined from the point of view of transient theory rather than the steady state, and the relationship of polarization modulation to orbital angular momentum and adaptive optics described.

In section 3.0 the media substituting for the atmosphere and ionosphere are described. The media examined were: water vapor, heated air, and phase plates both static and rotating.

The laboratory test configurations are described in section 4.0 and the test results in section 5.0, together with data analysis methods. Section 5.0 of this report provides the evidence supporting the conclusion of this report regarding temporal and spatial jitter mitigation.

Polarization modulation is best described in terms of geometric (Clifford) algebra, rather than conventional vector/tensor analysis. Therefore section 6.0 is a brief introduction to geometric algebra and is applied to polarization modulated beams.

Section 7.0 describe the established methods of obtaining transparency, self-induced transparency and electromagnetically induced transparency, and their differences with respect to polarization modulation.

## 2.0 THEORY – POINCARÉ SPHERE & BLOCH MODEL.

### 2.1 POINCARÉ SPHERE

It is well-known that all static polarizations of a beam of radiation<sup>2</sup>, as well as all static rotations about the axis of the beam can be represented on a Poincaré sphere (Fig 2.1.1, 2.1.2A). Therefore, a vector representation of a beam, centered in the middle of the sphere and pointed to the underside of the surface of the sphere at a location on the surface, will represent a beam's static polarization. That static vector represents the *instantaneous* polarization and rotation angle of the beam. However, if one causes that vector to trace a trajectory *over time* on the surface of the sphere (i.e. the vector is moving), a *continual change (over time)* of a polarized beam, or a *polarization modulated* (and/or *rotation modulated*) beam (Fig 2.2.1B) is represented. If the beam is sampled by a detector device (which can be by absorption through the excitation of electronic or vibrational energy levels of a molecular system) at a rate which is *less than* the rate of modulation, then the sampled output from the detector device will be a mixing or mapping of two components of the wave, which are continuously changing with respect to each other, into one snapshot of the wave, at one location on the surface of the sphere and at one instantaneous polarization and axis rotation. If the polarization modulation  $\partial \phi / \partial t^n$  is by the first differential of the phase  $\phi$  (between two orthogonally polarized beams), i.e.,  $n = 1$  or  $\partial \phi / \partial t$ , the trajectory is of constant velocity (Fig 2.2.1C). Thus, from the viewpoint of a device sampling at a rate less than the modulation rate, a two-to-one mapping (over time) will have occurred, which is the signature of an  $SU(2)/Z_2$  field<sup>3</sup> (Barrett 1997-2008). Polarization modulation at higher differentials of phase provide trajectories of non-constant velocity

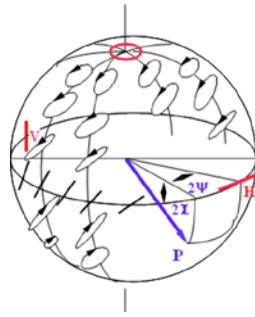


Fig 2.1.1 The Poincaré sphere, representing statically, all polarizations and rotations. Circularly polarized co-rotating is represented at the north pole; circularly polarized counter-rotating is represented at the south pole. Along the longitudinal lines are represented the varieties of elliptical polarizations. Around the equator latitude line are shown horizontally polarized linear, and vertically polarized linear configurations, as well as the variety of linear polarizations in between these. The angles  $2\psi$  and  $2\chi$  are shown for a combined beam. Another angle,  $\delta$ , is relevant and is the inter-beam phase of the combined beam's constituent beams and not represented here. These are static representations. However, *POLMOD* is a movement of the  $P$  vector on the sphere and is not static.

<sup>2</sup> “Static polarization” indicates a beam that is e.g., *always* linearly (or circularly or elliptically) polarized, which means all the waves are either vertically – or horizontally – aligned, or *always* circularly, or *always* elliptically polarized, where the wave moves in a circular (right or left) or elliptical pattern as it propagates, and can be represented as a single point on the surface of a Poincaré sphere. *In contrast*, polarization modulation results in a movement from point to point over time and along a trajectory as shown in Fig 2.1.2 C, below.

<sup>3</sup> This field is characterized by a generalization of Maxwell's equations – see Barrett, 2008.

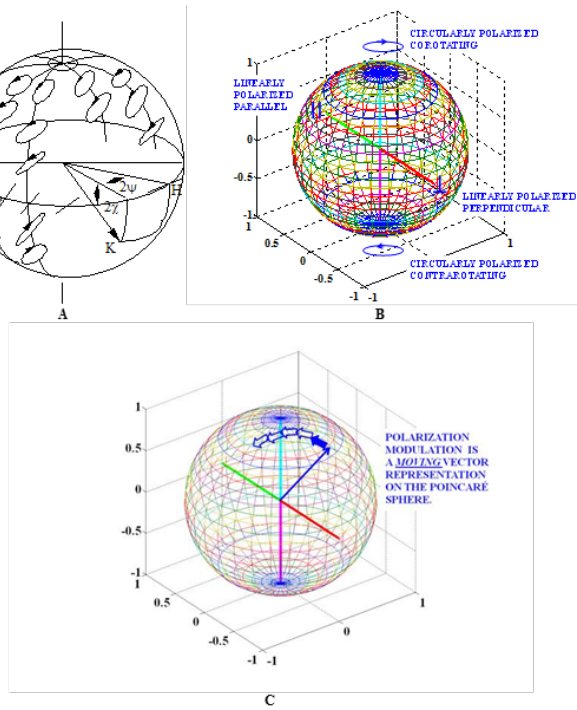


Fig 2.1.2 A Poincaré sphere representation for the combined beam. The equatorial region spans linearly polarized parallel to perpendicular. The longitudinal lines span circularly polarized corotating to contrarotating, passing through forms of elliptical polarization depending on latitude. A: The Poincaré sphere, with static polarizations and rotations represented. B Poincaré sphere representation of 4 static polarizations. C: A moving representation of a POLMOD beam. (White Paper).

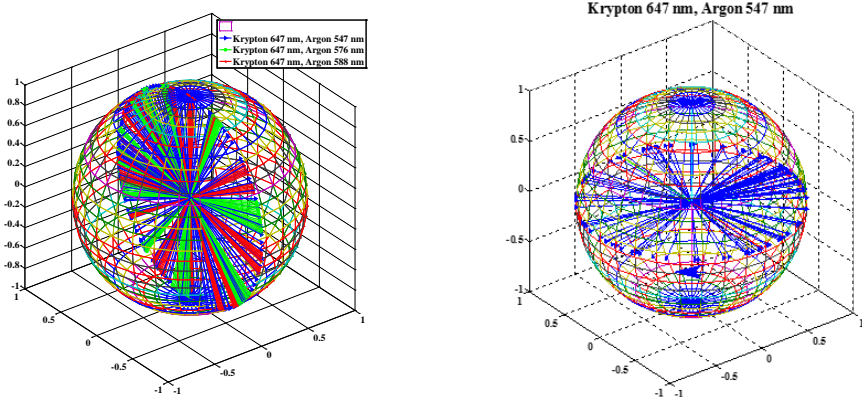


Fig 2.1.3 A: An arbitrary sole POLMOD beam (2 lasers *orthogonally polarized* of 2 different wavelengths) Poincaré sphere representation:  $\frac{\partial \chi}{\partial t}$ . Trajectories on the Poincaré sphere the Krypton laser at  $\lambda = 647$  nm, and the Argon laser at  $\lambda = (1) 457$ ; (2) 476; and (3) 488 nm. In comparison with B, notice that there are only longitudinal changes, while the latitude (axial rotation) is constant.

B: An arbitrary sole AXMOD beam (2 lasers *plane polarized* of 2 different wavelengths) Poincaré sphere trajectory representation:  $\frac{\partial \psi}{\partial t}$ . In comparison with A, notice that there are only latitudinal changes, while the longitude (polarization) is constant. (White Paper).

Using 3 lasers of different frequency in a combined beam, results in different trajectories on the Poincaré sphere (Fig 2.1.4)

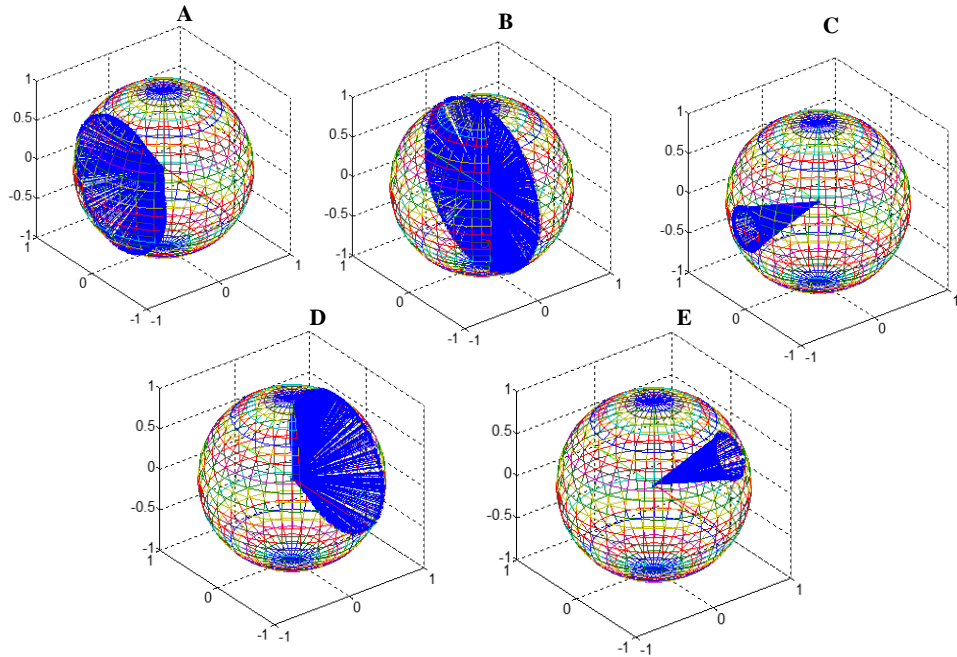


Fig 2.1.4 Amplitude Control of Trajectories on the Poincaré Sphere. Poincaré Sphere Representations over 1 picosecond, Three laser situation:  $f_1 = 31.6$ ,  $f_2 = 30.0$  and  $f_3 = 28.6$  THz. On one linearly polarized channel:  $a_1 \sin(2\pi f_1 t)$ . On second, orthogonally polarized channel:  $a_2 \sin(2\pi f_2 t) + a_3 \sin(2\pi f_3 t)$ .

- A:  $a_1 = 1$ ;  $a_2 = 1$ ;  $a_3 = 1$ .
- B:  $a_1 = 1$ ;  $a_2 = 0.5$ ;  $a_3 = 0.5$ .
- C:  $a_1 = 1$ ;  $a_2 = 4$ ;  $a_3 = 4$ .
- D:  $a_1 = 4$ ;  $a_2 = 1$ ;  $a_3 = 1$ .
- E:  $a_1 = 16$ ;  $a_2 = 1$ ;  $a_3 = 1$ .

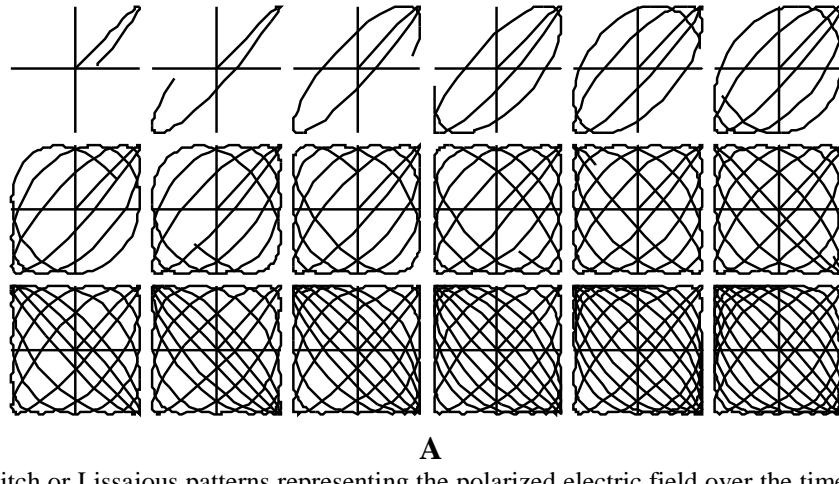
If the polarization-modulated-beam, or polarization-modulated-and-rotated-beam is viewed head-on, and the beam is sampled by two orthogonally polarized detectors, the beam traces out Bowditch<sup>4</sup> or Lissajous<sup>5</sup> patterns (Fig 2.1.5A) in the  $x, y$  directions. In the  $z$ -direction, the beam would appear as in Fig 2.1.5B.

Losses in transmission through the atmosphere/ionosphere are due to the rate of polarization modulation being less than the relaxation times of the absorption mechanisms of the atmosphere/ionosphere. Furthermore, the modulations, which result in trajectories of the moving vector  $\mathbf{K}$ , (see Fig 2.1.2A), on the sphere, are infinite in number. The moving  $\mathbf{K}$  is not confined to any specific wandering over the sphere. Moreover, those modulations at a rate of *multiples* of  $2\pi$  result in the return to a pass through, or pass by, a *single* location on the sphere and *are detected* at a frequency of *exactly and only*  $2\pi$ , if the detection is by a device or molecular system sampling at a rate of only  $2\pi$ . In other words, a relatively slow-rate sampling device or molecular system cannot detect the trajectory of a fast moving beam  $\mathbf{K}$ , departing from, and arriving back at, the location on the sphere representing the slow-rate detector. *To a relatively slowly sampling device*

<sup>4</sup> Nathaniel Bowditch, 1815.

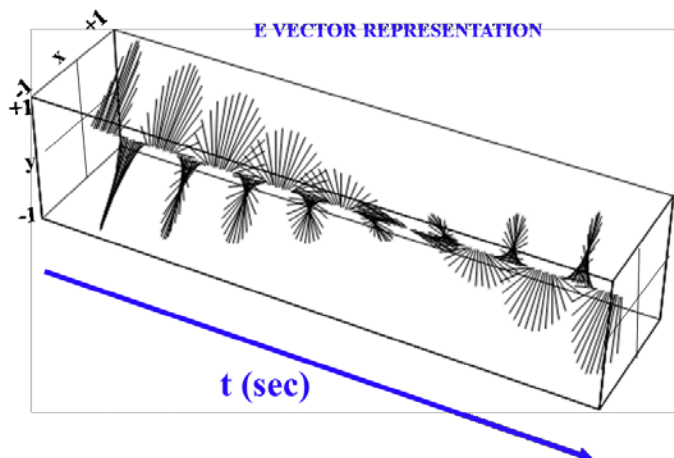
<sup>5</sup> Jules Antoine Lissajous, 1857.

or molecular system, a fast modulated beam can have “internal energies” quite undetected and unsuspected (Barrett, 2008).



A

Fig 2.1.5A: Bowditch or Lissajous patterns representing the polarized electric field over the time of one cycle of the beam, viewed in the plane of incidence, resulting from two orthogonally polarized fields, which are out of phase by the following degrees: 0, 21, 42, 64, 85, 106, (top row); 127, 148, 169, 191, 212, 233, (middle row); 254, 275, 296, 319, 339, 360 (bottom row). In these patterns, the plane polarizations (horizontal and vertical) are represented at 45° to the axes, and each pattern is the history of the beam up until one cycle (wavelength) of the beam is traversed.



B

Fig 2.1.5B: Representation of the  $\mathbf{E}$  field of a polarization modulated beam over  $2\pi$  in the  $z$ -direction. Note: this does not represent circular polarization. Circular polarization – whether right-handed, or left-handed – is defined as a constant 45° phase difference between the two orthogonal beams. Here, on the other the phase angle is *continuously changing polarization over time as indicated*. Now the beam, *at a special instant*, but only at an instant, will be circularly polarized if the two orthogonal beams are 45° out-of-phase. That is a special and unique case and represented at the two poles of the Poincaré sphere. *In the more general case*, the resultant beam, represented by vector  $\mathbf{K}$  in Fig 2.1.2C, can roam, moving anywhere on the Poincaré sphere, and not remain static at the poles of the sphere, which define the static conditions of circularly polarized light, right- and left-handed – see Fig 2.1.2A.

If the modulated or moving  $\mathbf{K}$  vector in Fig 2.1.2A is rotating continuously (i.e., through multiples of 0 –  $2\pi$ ) at a rate that is greater than, or a multiple of, the sampling rate of a detector

(statically positioned on the sphere), then observed from the vantage point of that detector,  $\mathbf{K}$  appears to be static (i.e., statically polarized) – yet it is not. It is as if the detector, positioned at a location on the Poincaré sphere only “opens its eyes to see” as the  $\mathbf{K}$  vector passes by that location. Therefore the static detector “believes” the  $\mathbf{K}$  vector is a pulse that is also statically polarized at that location – yet it is not, being polarization modulated and moving. Moreover, if the detector requires the  $\mathbf{K}$  vector to remain stationary at that location on the sphere for a certain period of time (in order that the beam that  $\mathbf{K}$  represents to be absorbed), then if  $\mathbf{K}$  does not remain for that certain period of time due to the modulation rate being higher than the detector’s sampling rate, the detector will not detect  $\mathbf{K}$  (i.e. elastically or inelastically scatter or absorb the beam). “The requirement for  $\mathbf{K}$  to remain stationary for a certain period” in a real detector or molecular system is due to the *relaxation time* of a detector or molecular system. In other words, it always takes a certain time for energy to be captured or parametrically up or down converted or passed to a “heat or thermal sink”.

A statically polarized detector is a *U(1) unipolarized, constant rotational axis, sampling device*. This kind of detector obeys Maxwell’s equations in their basic, i.e., U(1) form. On the other hand, the fast polarization (and rotation) modulated beam is a *multipolarized, multirotation axis, SU(2) beam*, that obeys a more complex form of Maxwell’s equations. In principle, the period of modulation can be faster than the electronic or vibrational or dipole relaxation times of any atom or molecule. *In other words, such modulated beams can be modulated at a rate greater than the relaxation or absorption time of electronic and vibrational states, permitting self-induced transparency.* This is the ideal condition to minimize turbulence and other losses.

More, specifically, let a beam be represented as  $\sum_n \psi_n = \sum_n \chi_n a_n \exp(i2\pi\nu t_n)$  where  $\chi_n$  is the polarizability induced by the n-th E-vector field  $a_n \exp(i2\pi\nu t_n)$ . Let an arbitrary polarized field be represented by two such beams but orthogonally polarized:

$$\begin{aligned} I(\tau) = \Psi\Psi^* &= |\psi_1 + \psi_2|^2 = |\chi_1 a_1 \exp(i2\pi\nu t) + \chi_2 a_2 \exp(i2\pi\nu(t + \tau))|^2 \\ &= \chi_1^2 a_1^2 + \chi_2^2 a_2^2 + (\chi_1 \chi_2) \cos(\theta) 2a_1 a_2 \cos(2\pi\nu\tau) \end{aligned}$$

where  $\theta = 90^\circ$  for orthogonally polarized beams; and  $\tau = t_1 - t_2$ . This composite beam resulting from the two beams, would be statically polarized and with a constant  $\tau$  dependency.

If the same field was the resultant from beams in which  $\tau$  is modulated, i.e., there is a  $d\tau/dt$ , then that resultant would not be statically polarized, but polarization modulated (POLMOD):

$$\begin{aligned} I\left(\frac{d\tau}{dt} = k \frac{d\varphi}{dt}\right) = \Psi\Psi^* &= |\psi_1 + \psi_2|^2 = |\chi_1 a_1 \exp(i2\pi\nu t) + \chi_2 a_2 \exp(i2\pi\nu(t + d\tau/dt))|^2 \\ &= \chi_1^2 a_1^2 + \chi_2^2 a_2^2 + (\chi_1 \chi_2) \cos(\theta) 2a_1 a_2 \cos(2\pi\nu\tau + d\tau/dt), \end{aligned}$$

where  $\varphi$  is phase. Ideally, this is the way one would obtain POLMOD. Technically, this is quite possible, but requires complex equipment.

An easier, but limited, way to obtain POLMOD is to combine and beat two orthogonally polarized beams of different wavelengths:

$$I\left(\frac{d\tau}{dt} = k \frac{d\varphi}{dt}\right) = \Psi\Psi^* = |\psi_1 + \psi_2|^2 = |\chi_1 a_1 \exp(i2\pi\nu_1 t) + \chi_2 a_2 \exp(i2\pi\nu_2 t)|^2$$

$$= ((\chi_1\chi_2) \cos(\theta) 2a_1a_2 \cos(2\pi\nu_3t) \sin(2\pi\nu_4t))^2,$$

where  $\nu_3 = \frac{\nu_1-\nu_2}{2}$  and  $\nu_4 = \frac{\nu_1+\nu_2}{2}$  and the beat frequency is  $\nu_{beat} = \nu_1 - \nu_2$ .

If the time constant required for both (i) polarization compatibility between incident radiation and molecule and (ii) for energy transfer to the detecting molecule to occur, is greater than  $1/\nu_{beat}$ , there will be a situation similar to that of pulse/transient self-induced transparency (i.e., SIT), with the incident radiation captured by the detecting molecule, but reradiated back into the radiating beam. The difference is that pulse self-induced transparency achieves transparency by challenging the relaxation time of the detecting molecule by switching off in a shorter time interval than that relaxation time. In the present cw self-induced transparency, the relaxation time of the detecting molecule is challenged by the shorter time interval of polarization compatibility.

As an example, Fig 2.1.6 shows the spectra of two constituent beams, 700 and 770 TeraHertz. However, such a representation does not address the two beams' polarization, nor their combination. If the two beams are orthogonally polarized and combined, the resulting combined beam is a POLMOD beam. In which case, a molecular system detects the combined beam by the conjoint simultaneous dipole stimulation/sampling, and this molecular sampling is set by the excited state relaxation time.

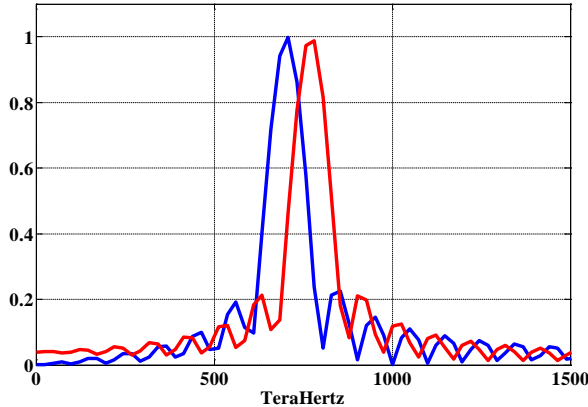


Fig 2.1.6 Spectra of two constituent beams at 700 and 770 TeraHertz. This representation does not address different polarizations. If the two beams are orthogonally polarized and combined, the combined beam is a POLMOD beam. A molecular system detects the combined beam by the conjoint simultaneous dipole stimulation/sampling, and the molecular sampling is set by the excited state relaxation time.

A POLMOD beam is formed from two orthogonally polarized beams. Therefore, each constituent beam acts in the manner of an additional magnetic field to the other beam; or, stated differently, each magnetic field of one beam acts as an electric field to the other. The total energy density is the sum of the densities of the field of each beam:

$$\omega = \omega_1 + \omega_2 = \frac{1}{2}\epsilon E_1^2 + \frac{1}{2}\epsilon E_2^2 \text{ joules/m}^2$$

For a small volume,  $\Delta v$ , the decrease in energy as a function of time is:

$$-\frac{\partial}{\partial t} \left( \frac{1}{2}\epsilon E_{21}^2 + \frac{1}{2}\epsilon E_2^2 \right) \Delta v = \int_S S \cdot ds \text{ watts}$$

where  $S$  = energy per unit area passing per unit time through the surface of the volume  $\Delta v$  in units of watts/m<sup>2</sup>. Diving by  $\Delta v$  and taking the limit obtains:

$$\nabla \cdot S = - - \frac{\partial}{\partial t} \left( \frac{1}{2} \epsilon E_1^2 + \frac{1}{2} \epsilon E_2^2 \right)$$

Using Maxwell equation substitutions, the result is:

$$S = E_1 \times E_2$$

Using the fact that  $E_2$  is the effective magnetic field to  $E_1$  and substituting, gives:

$$S = E \times H \text{ watts/m}^2$$

The Bowditch or Lissajous pattern representations of Fig 2.1.5A are thus the differential, or instantaneous Poynting vector representations; and the combined **E** field representation 2.1.5B, *when integrated over time*, is the Poynting vector.

In the following Fig 2.1.7 are shown (i) a combined radiated POLMOD beam traveling in the z (time) direction; (ii) the same combined beam as a function of the two orthogonally polarized constituent beams; and (iii) the changing frequencies of the first and second constituent beams in the x and y directions. This last figure (iii) indicates that a statically polarized molecular detector will experience radiation changing in the x and y direction at the rates shown.

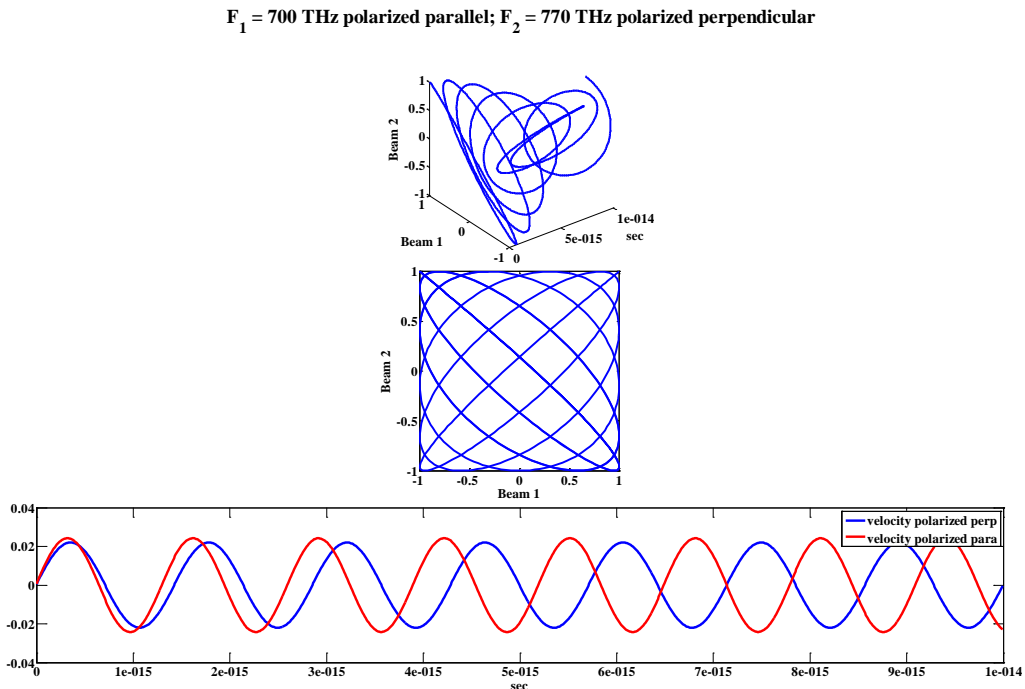


Fig 2.1.7 Top: A combined **E** field radiated POLMOD beam traveling in the z (time) direction. Middle: the same **E** field combined beam as a function of the two orthogonally polarized constituent beams – a Lissajous pattern. Lower: The changing frequencies of the first and second constituent **E** field beams in the x and y directions.

If a horizontally polarized beam of frequency 700 TeraHertz is combined with a perpendicularly polarized beam of 1050 TeraHertz, and if a molecular detector's polarization preference is 700 TeraHertz, horizontally polarized, then the detector will be polarization-compatible with the radiation, but only for durations ( $5.8^{-15}$  sec) that are a function of the beat frequency indicated in red in Fig 2.1.8. The polarization-compatible incident combined beam is indicated in blue. An objective of POLMOD beam design was to establish the beat frequency such that the relaxation time of atmospheric molecules is defeated. Fig 2.1.8 shows a 700+770 THz POLMOD radiated beam traveling in the z (time) direction and "sampled" by generic molecular systems at  $5^{-16}$  sec,  $1^{-15}$  sec and C:  $2^{-15}$  sec. Each molecular system will only integrate these patterns (detection by g $\rightarrow$ e state excitation) if the excitation-induced dipole is compatible in polarization with the excitation.

Fig 2.1.10 shows other examples of a 700+770 THz orthogonally polarized cw POLMOD beam – polarization beat frequency repetition interval:  $1.4^{-14}$  sec; and a 700+1050 THz POLMOD – polarization beat frequency repetition interval:  $3^{-15}$  sec. These figures show the requirements for relaxation times for three generic molecular systems also requiring (a) circularly polarized corotating compatibility with an effective magnetic field (green); (b) circularly polarized contrarotating compatibility with an effective magnetic field (blue); and (c) linear polarization compatibility (magenta). It was an objective of the present completed tests to determine the beat frequency repetition interval for optimum atmospheric propagation.

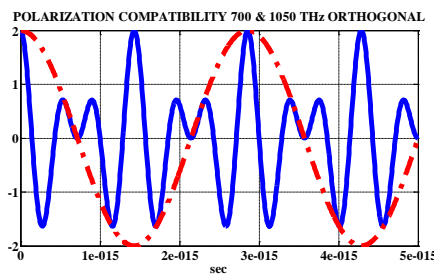


Fig 2.1.8 If a horizontally polarized beam of frequency 700 TeraHertz is combined with a perpendicularly polarized beam of 1050 TeraHertz, and if a molecular detector's polarization preference is 700 TeraHertz, horizontally polarized, then the detector will be polarization-compatible with the radiation, only for durations that are a function of the beat frequency indicated in red. The polarization-compatible incident combined beam is indicated in blue. An objective of the proposed tests is to establish the beat frequency repetition interval (here  $3^{-15}$  sec) such that the relaxation time of atmospheric molecules is defeated.

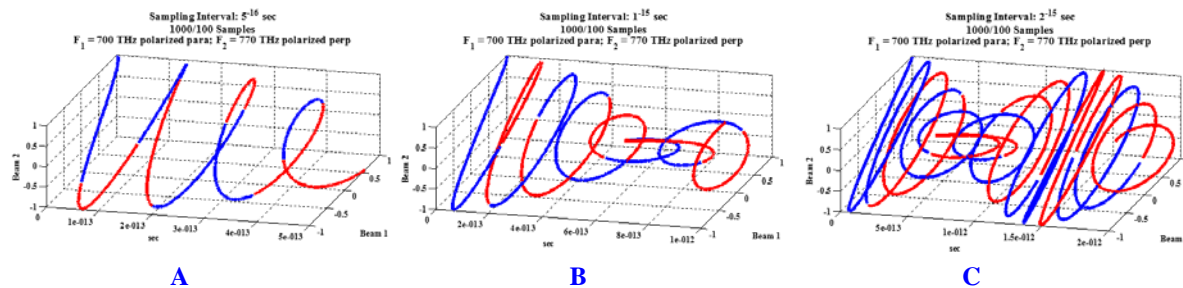


Fig 2.1.9 A 700+770 THz POLMOD radiated beam traveling in the z (time) direction and "sampled" by generic molecular systems at A:  $5^{-16}$  sec; B:  $1^{-15}$  sec; and C:  $2^{-15}$  sec. Each molecular system will only integrate these patterns (detection by g $\rightarrow$ e state excitation) if the excitation-induced dipole is compatible in polarization with the excitation.

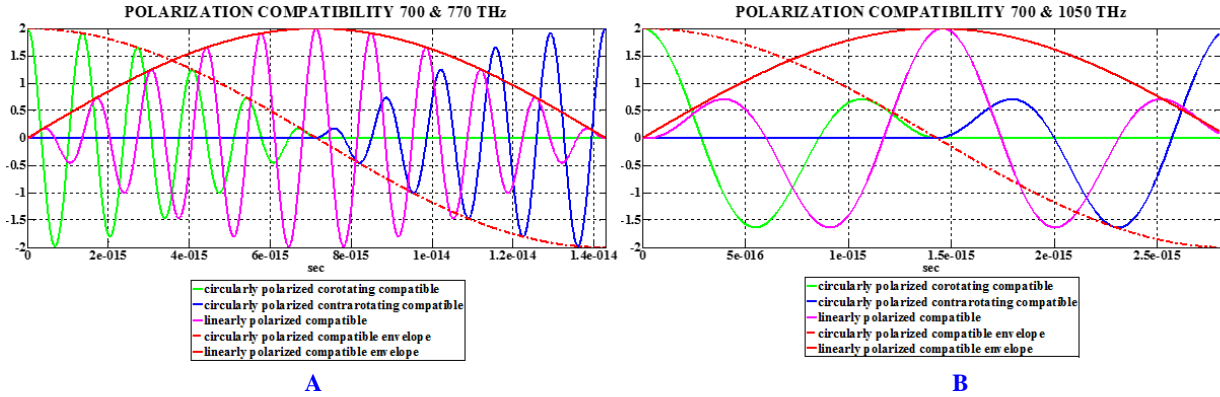


Fig 2.1.10 These figures show the requirements for relaxation times for three generic molecular systems also requiring (a) circularly polarization *corotating* compatibility with an effective magnetic field (green); (b) circularly polarization *contrarotating* compatibility with an effective magnetic field (blue); and (c) linear polarization compatibility (magenta). A: 700+770 THz POLMOD – polarization beat frequency repetition interval:  $1.4 \times 10^{-14}$  sec. B: 700+1050 THz POLMOD – polarization beat frequency repetition interval:  $3 \times 10^{-15}$  sec.

Referring back to the Poincaré sphere (Fig 2.1.1), which represents *statically*, all polarizations and rotations and reviewing: circularly polarized co-rotating is represented at the north pole; circularly polarized counter-rotating is represented at the south pole. Along the longitudinal lines are represented the varieties of elliptical polarizations. Around the equator latitude line are shown horizontally polarized linear, and vertically polarized linear configurations, as well as the variety of linear polarizations in between these. The angles  $2\psi$  and  $2\chi$  are shown for a combined beam. Another angle,  $\delta$ , is relevant and is the inter-beam phase of the combined beam's constituent beams and not represented here. POLMOD is a movement of the P vector on the sphere and is not static. Djordjevic and Arabaci (2010) have proposed exploitation of photon spin angular momentum (SAM) associated with polarization, and orbital angular momentum (OAM) associated with the azimuthal phase of the complex electric field (cf. Djordjevic et al, 2007; Djordjevic & Djordjevic, 2009; Djordjevic, 2011; Leach et al 2004; Gibson et al 2004; Paterson, 2005). POLMOD is related to modulated SAM, and AXMOD to modulated OAM, but for purposes of mitigating channel/atmospheric/ionospheric effects, rather than communications. Both can be represented on the Poincaré sphere.

POLMOD requires a changing angle  $2\chi$ . AXMOD requires a changing angle  $2\psi$ . A *moving* representation of a POLMOD beam is shown in Fig 2.1.2C.

The angular momentum of a beam can be given as (Jackson, 1998, p. 350):

$$\mathbf{L} = \frac{1}{\mu_0 c^2} \int d^3 \left[ \mathbf{E} \times \mathbf{A} + \sum_{j=1}^3 E_j (\mathbf{x} \times \nabla) A_j \right].$$

The first term is identified with the “spin” of the photon; and the second with “orbital” angular momentum because of the presence of the operator  $\mathbf{x} \times \nabla$  term. It follows, therefore, that POLMOD is defined as:

$$d\mathbf{L}_{POLMOD}/dt = \frac{1}{\mu_0 c^2} [\mathbf{E} \times \mathbf{A}],$$

and AXMOD as:

$$\mathbf{dL}_{AXLMO} / \mathbf{dt} = \frac{1}{\mu_0 c^2} \left[ \sum_{j=1}^3 E_j (\mathbf{x} \times \nabla) A_j \right].$$

The main results of the present series of tests reported are:

- Jitter mitigation.
- Amplitude loss mitigation
- Beam pointing movement mitigation.

The frequency and amplitude dependence of these effects has yet to be investigated due to the unavailability of the frequency control of both the modulating and modulated beams. Future work would address these issues.

The rationale for the tests reported is related tangentially to the theory of elastic and inelastic radiation scattering. The relevant background is as follows. If (a) exciting radiation is near resonance with an electronic transition, or (b) there are electronic Raman transitions (Mortensen & Konigstein, 1968), or (c) there is a Jahn-Teller active state (Child & Longuet-Higgins, 1961), then anti-symmetric as well as symmetric components of the Raman tensor are predicted (Plazcek, 1934; McClain, 1971). If the scattered radiation is due only to an induced electric dipole, a depolarization ratio has three components when there is antisymmetric scattering:

- (1) the isotropy  $\alpha^2$ .
- (2) the symmetric isotropy  $\gamma_s^2$ .
- (3) the anti-symmetric isotropy  $\gamma_{as}^2$ .

The depolarization ratio in terms of these components is:

$$\rho = \frac{I_{||}}{I_{\perp}} = \frac{3\gamma_s^2 + 5\gamma_{as}^2}{45\alpha^2 + 4\gamma_s^2},$$

and in terms of the elements of the Raman tensor  $\alpha_{ij}$ , ( $ij = x, y, z$ ):

$$\begin{aligned} \alpha^2 &= (\alpha_{xx} + \alpha_{yy} + \alpha_{zz})^2 \\ \gamma_s &= -\frac{1}{2} \left[ (\alpha_{xx} - \alpha_{yy})^2 + (\alpha_{yy} - \alpha_{zz})^2 + (\alpha_{zz} - \alpha_{xx})^2 \right] \\ &\quad - \frac{3}{4} \left[ (\alpha_{xy} + \alpha_{yx})^2 + (\alpha_{xz} + \alpha_{zx})^2 + (\alpha_{yz} + \alpha_{zy})^2 \right] \\ \gamma_{as} &= -\frac{3}{4} \left[ (\alpha_{xy} - \alpha_{yx})^2 + (\alpha_{xz} - \alpha_{zx})^2 + (\alpha_{yz} - \alpha_{zy})^2 \right] \end{aligned}$$

Defining:

$I_{PARA}$  = incident radiation linearly polarized parallel to scattered radiation

$I_{PERP}$  = incident radiation linearly polarized perpendicular to scattered radiation

$I_{CO}$  = incident radiation circularly polarized corotating to scattered radiation

$I_{CONTRA}$  = incident radiation circularly polarized contrarotating to scattered radiation

a reversal coefficient for scattered radiation at 90° to incident radiation is:

$$r = \frac{6\gamma_s^2}{45\alpha^2 + \gamma_s^2 + 5\gamma_{as}^2} = \frac{I_{CO}}{I_{CONTRA}}$$

and a general reversal coefficient dependent on the scattering angle,  $\nu$ , is (Mortensen & Hassing, 1980):

$$R(\nu) = \frac{1 - \frac{1 - \rho}{2(1 + \rho)} \sin^2(\nu) - \frac{1 - r}{1 + r} \cos^2(\nu)}{1 - \frac{1 - \rho}{2(1 + \rho)} \sin^2(\nu) + \frac{1 - r}{1 + r} \cos^2(\nu)}$$

This general reversal coefficient can be seen to be a function of the three invariants: the isotropy  $\alpha^2$ , the symmetric isotropy  $\gamma_s^2$  and the antisymmetric isotropy  $\gamma_{as}^2$ , and the intensities in four polarization spectra are related to the three invariants by:

$$\begin{aligned} I_{PERP} &= 3\gamma_s^2 + 5\gamma_{as}^2 \\ I_{PARA} &= 45\alpha^2 + 4\gamma_s^2 \\ I_{CO} &= 6\gamma_s^2 \\ I_{CONTRA} &= 45\alpha^2 + \gamma_s^2 + 5\gamma_{as}^2 \end{aligned}$$

Therefore, in the case of scattered radiation due only to an induced electric dipole:

$$I_{PERP} + I_{PARA} = I_{CO} + I_{CONTRA}$$

and only three measurements are needed, the fourth providing a check.

The invariants are related to the intensity data by:

$$\begin{aligned} 6\gamma_s^2 &= I_{CO} \\ 5\gamma_{as}^2 &= I_{PERP} - \frac{1}{2}I_{CO} \\ 45\alpha^2 &= I_{PARA} - \frac{2}{3}I_{CO} \end{aligned}$$

This is the simple picture if there are moments higher than an induced electric dipole that are not involved. This is not the case with optically active molecules (Barron, 1978, 1982). In these cases, besides the polarizability tensor, scattering is defined in terms of optically active tensors defining electric and magnetic dipoles. The Hamiltonian of a system of charged particles interacting with an electromagnetic field is a multipole expansion (Fiutak, 1963), in which the semiclassical Kramers-Heisenberg dispersion equation is demonstrated to be identical with the corresponding quantum mechanical description (Göppert-Mayer, 1931). The Hamiltonian describing a molecule excited by a field is (Hertzfeldt & Göppert-Mayer, 1936; Fiutak, 1963; Buckingham, 1967):

$$\mathcal{H} = \mathcal{H}_0 - d_\alpha E_\alpha - \frac{1}{3} \Theta_{\alpha\beta} E_{\alpha\beta} - m_\alpha - 1/2 \chi_{\alpha\beta} H_\alpha H_\beta$$

where

$\mathcal{H}_0$  is the Hamiltonian for the free molecule;  
 $d_\alpha = \sum_i e_i r_i$  or the electric dipole moment;  
 $\Theta = \frac{1}{2} \sum_i (3r_{i\alpha} r_{i\beta} - r_i^2 \delta_{\alpha\beta})$  or the quadrupole moment;  
 $m_\alpha = \sum_i (e_i/2m) \epsilon_{\alpha\beta\gamma} r_{i\beta} p_{i\gamma}$  or the magnetic moment operator for momentum  $p$ ;  
 $E_\alpha$  and  $E_{\alpha\beta}$  are the electric field and the field gradient at the origin due to external charges;  
 $\chi_{\alpha\beta}$  is the nonlinear susceptibility;  
 $H_\alpha$  and  $H_\beta$  denote the magnetic field;  
 $e_i$  is the  $i$ th element of charge at the point  $r_i$  relative to an origin fixed at some point on the molecule;  
 $\alpha\beta$  denote vector or tensor components and can be equal to  $x, y, z$ .

This is a steady state Hamiltonian multipole expansion but only tangentially relevant to the work reported, as the expansion does not address the relaxation times (transient state) challenged by polarization modulated beams. The duration of the transient polarization “window” for a variety of gases is as follows.

The Maxwell–Boltzmann distribution law for molecular velocities provides the mean square and mean velocities as:

$$\bar{v}^2 = \frac{3fT}{m};$$

$$\bar{v} = (8\bar{v}^2/3\pi)^{1/2}$$

The kinetic theory of gases, assuming that molecules interact like hard spheres, gives:

$$\eta = (5/16\sigma^2)(mkT/\pi)^{1/2} \quad \tau = l/v = 4\eta/5p$$

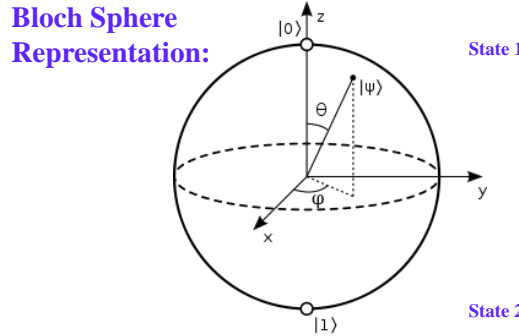
$$l = m/(\pi\rho\sigma^2\sqrt{2})$$

where $k$ = Boltzmann's constant	$\sigma$ = molecular diameter
$T$ = absolute temperature	$m$ = mass of molecule
$p$ = pressure	$l$ = mean free path
$\rho$ = density	$\tau$ = mean time between collisions.
$\eta$ = viscosity	

The  $9.4 \mu\text{m}$   $\text{CO}_2$  absorption band has a band interval from  $850(\text{cm}^{-1}) = 12 \mu\text{m}$  (25.48 THz) to  $1250(\text{cm}^{-1}) = 8 \mu\text{m}$  (37.47 THz), i.e., 11.99 THz. The relaxation time is thus on the order of  $1/11.99 \times 10^{12} = 83$  femtoseconds. Another limiting factor on the window is the molecular inter-collision time. The mean time between collisions is 108 picoseconds – three orders of magnitude greater than the relaxation time.

## 2.2 BLOCH SPHERE

The Bloch sphere (Fig 2.2.1) is a geometrical representation of the state-space of a two-level quantum system. The Bloch sphere is a unit 2-sphere, with each pair of antipodal points corresponding to mutually orthogonal state vectors. The north and south poles of the Bloch sphere are typically chosen to correspond to the standard basis vectors  $|0\rangle$  and  $|1\rangle$ . Substituting polarization states for quantum states gives the Poincaré sphere.



**Rabi Frequency:**  $\Omega(z, t) = 2\mu_{12} \varepsilon^* E(z, t)/\hbar$ , where  
 $E(z, t)$  is the 2-level dipole moment,  
 $\mu_{12}$  is the envelope function, and  
 $\varepsilon$  is the unit polarization vector.

Fig 2.2.1 *The Rabi Frequency*. The Rabi frequency is the frequency of population oscillation for a given atomic transition in a given light field. It is associated with the strength of the coupling between the light and the transition. Rabi flopping between the levels of a 2-level system illuminated with resonant light, will occur at the Rabi frequency. The Rabi frequency is a semi-classical concept as it is based on a quantum atomic transition and a classical light field. If the incident radiation is a pulse, then at the end of the pulse the Bloch vector has been rotated through an angle:  $A(z, t) = \theta(z, t) = \int_{-\infty}^t \Omega(z, t') dt'$ , where  $\theta$  is the tipping angle or the angle through which the Bloch vector is rotated in the  $y'$  and  $z'$  plane about the  $x'$  axis. The angle  $A$  is also referred to as the area of the pulse, as it is proportional to the area under the pulse envelope in the time domain. For the special case of an intense light pulse producing atomic excitation, and if the pulse area is:  $A = 2n\pi$ ,  $n = 1, 2, 3, \dots$  The pulse propagates through the medium without attenuation of its area, i.e., the medium appears transparent to the light pulse, despite the fact that its midfrequency coincides with an atomic resonance.

If the incident radiation on a molecular system is a (POLMOD cw) “pulse”, then at the end of the “pulse” the Bloch vector has been rotated through an angle:

$$A(z, t) = \theta(z, t) = \int_{-\infty}^t \Omega(z, t') dt'$$

Where  $\theta$  is the tipping angle or the angle through which the Bloch vector is rotated in  $y'$  and  $z'$  plane about the  $x'$  axis. The angle  $A$  is also referred to as the area of the pulse, as it is proportional to the area under the pulse envelope in the time domain.

For the special case of an intense light pulse producing atomic excitation, and if the pulse area is:

$$A = 2n\pi, n = 1, 2, 3, \dots,$$

the pulse propagates through the medium without attenuation of its area, i.e., the medium appears transparent to the light pulse, despite the fact that its midfrequency coincides with an atomic resonance.

A simple representation of an ion is as an electron cloud attached to a fixed ion. If the attachments are represented in the x, y and z directions as “springs”, and those springs have different spring constants in the x, y and z directions, then polarization is more apt to occur in the direction or axis of the weakest spring constant. Therefore:

- Induced polarization will not be parallel to the direction of the inducing field.
- Susceptibility is not a scalar.

But differences in refractive index (birefringence) and absorption (dichroism) depend on the polarization:

$$\mathbf{P} = \epsilon_0 \chi \mathbf{E} = \epsilon_0 (\bar{\epsilon} - 1) \mathbf{E}$$

where:

$$1 + \chi = \bar{\epsilon} = \bar{\eta}^2 = \left( \eta + i \frac{c}{2\omega} \alpha \right)^2$$

Therefore, a difference in the refractive index, e.g., in the x and y directions (birefringence) or the absorption coefficient (dichroism) implies a difference in the susceptibility, e.g., in the x and y directions, which is due to the induced polarization. As previously noted, the appropriate representation of the susceptibility is thus not as a vector, but as a tensor:

#### SUSCEPTIBILITY TENSOR

$$\mathbf{P} = \epsilon_0 \begin{bmatrix} \chi_{11} & \chi_{12} & \chi_{13} \\ \chi_{21} & \chi_{22} & \chi_{23} \\ \chi_{31} & \chi_{32} & \chi_{33} \end{bmatrix} \mathbf{E}$$

Atoms are polarized by applied fields:

$$\begin{aligned} \mathbf{D} &= \epsilon_0 \mathbf{E} + \mathbf{P}, \\ \mathbf{P} &= \epsilon_0 \chi \mathbf{E}, \\ \mathbf{D} &= \epsilon_0 (1 + \chi) \mathbf{E}; \end{aligned}$$

and the conventionally defined Poynting vector is orthogonal to the incident field:

$$\mathbf{S} \cdot \mathbf{E} = 0,$$

but the wavevector is orthogonal to the electric displacement:

$$\mathbf{k} \cdot \mathbf{D} = 0.$$

Therefore, because in anisotropic media  $\mathbf{E}$  and  $\mathbf{D}$  are not necessarily parallel initially at time  $t_0$ , the Poynting vector and the wavevector may diverge.

In the Lorentz harmonically bound classical particle picture:

$$m\ddot{x} = -\frac{dV}{dx} = -m\omega_0^2 x,$$

the potential  $V$  is anharmonic for large displacements:

$$V(x) = \frac{m\omega_0^2}{2} x^2 + bx^3 + cx^4 + \dots$$

Therefore, the polarization varies nonlinearly with the field:

$$P = \varepsilon_0 \{ \chi^{(1)} E + \chi^{(2)} E^2 + \chi^{(3)} E^3 + \dots \}.$$

A one-dimensional electromagnetic wave propagating in the  $z$ -direction through a medium in which there is a macroscopic polarization is represented by:

$$\left( \frac{\partial^2}{\partial z^2} - \frac{n^2}{c^2} \frac{\partial^2}{\partial t^2} \right) \mathbf{E}(z, t) = \frac{1}{\varepsilon_0 c^2} \frac{\partial^2 \mathbf{P}(z, t)}{\partial t^2}$$

where  $\mathbf{P}(z, t)$  is a macroscopic polarization. However, the picture offered by this equation neglects the fact the  $\mathbf{E}$  is a vector and  $\mathbf{P}$  is a tensor, and that  $\mathbf{P}$  does not spring immediately, and instantaneously, into full amplitude.

There is also the claim that the dielectric constant is a tensor (Beth, 1936). Therefore, the field intensity  $\mathbf{E}$  is, in general, not parallel to the polarization,  $\mathbf{P}$ , nor to the electric displacement,  $\mathbf{D}$ . The torque is then given as:

$$\mathbf{L} = \mathbf{P} \times \mathbf{E}.$$

The Rabi frequency is the frequency of population oscillation for a given atomic transition in a given light field. It is associated with the strength of the coupling between the light and the transition. Rabi flopping between the levels of a 2-level system illuminated with resonant light, will occur at the Rabi frequency. But the Rabi frequency is a semi-classical concept as it is based on a quantum atomic transition and a classical light field. The Rabi frequency represented in the Bloch picture also does not represent the transient polarization state of a rapidly changing polarization modulated wave, nor does it account for the tensor nature of polarization  $\mathbf{P}$ .

## 2.3 KOLMOGOROV TURBULENCE THEORY

The Kolmogorov turbulence theory (KT) assumes statistical homogeneity, isotropy and without preferential direction (Kolmogorov, 1941a,b, 1962; Obukhov, 1962). These assumptions imply that the mean value of the field is constant and that correlations between random fluctuations in the field from point to point are independent of the chosen observation. KT assumes that small scale structures are statistically homogeneous, isotropic and independent of large scale structures. KT is limited to the inertial subrange  $l \ll L_o$ . It is assumed that the rate at which energy is supplied to the largest possible scale is equal to that dissipated at the shortest scale. In some sense, KT requires that eddies know how big they are, at which rate energy is supplied to them, and at which rate they must supply it to the next smaller eddies in the cascade. External energy is assumed to be input only on the largest scales and only dissipated on the smallest scales.

The optical field associated with the propagation through atmospheric turbulence of radiation from a monochromatic point source has a randomly modulated amplitude and a randomly modulated phase. Where the amplitude goes to zero the phase manifests a spatial dependence that indicates the presence of a branch point (Fried, 1998). A standard adaptive optics system, in particular one that utilizes a least mean square error wave-front reconstructor, will not be able to properly determine the phase of the optical field in the vicinity of such a branch point.

Oesch and Sanchez et al (Sanchez & Oesch, 2011a,b; Oesch & Sanchez, 2012; Oesch et al, 2012; Oesch et al, 2013) showed that fields with branch points are indicators of photons with

orbital angular momentum (OAM) that can be created in optical waves propagating through disturbed turbulence and the creation appears to be governed by the inner scale of turbulence.

While conventional phase-conjugate adaptive-optics provide good correction for weak-scintillation conditions, under strong scintillation conditions there is a significant degradation in correction as the scintillation increased. The presence of branch points in the phase appears to be the primary reason for the degradation in correction as the scintillation increases (Primmerman et al, 1995). Furthermore, Levine et al (1998) is the first study of statistics over near-ground paths *that also provided information on temporal fluctuations instead of probability density functions*. That study showed that near ground turbulence effects *are not consistent with the assumption of a Kolmogorov power spectrum*. Kolmogorov theory is thus inappropriate for the propagation issues addressed in the tests completed.

## 2.4 ORBITAL ANGULAR MOMENTUM (OAM)

Beth (1950) and Allen et al (1992; Allen & Padgett, 2000) showed that light beams that are not plane waves will possess orbital angular momentum (OAM). Oesch and Sanchez et al (Sanchez & Oesch, 2011a,b; Oesch & Sanchez, 2012; Oesch et al, 2012; Oesch et al, 2013) showed that fields with branch points are indicators of photons with OAM that can be created in optical waves propagating through disturbed turbulence and the creation appears to be governed by the inner scale of turbulence. Furthermore, it was demonstrated that creation of angular momentum occurred at the highest frequencies is moderated by the inner scale of turbulence. Jackson (1998, p. 350) has long provided a classical formulation of angular momentum in spin angular momentum (SAM) and orbital angular momentum (OAM) contributions.

As previously noted, POLMOD is essentially *modulated* SAM and axial modulation (AXMOD) is *modulated* OAM, but for purposes of mitigating channel/atmospheric/ionospheric effects, rather than communications. POLMOD is essentially *modulated* SAM and axial modulation (AXMOD) is *modulated* OAM, but for purposes of mitigating channel/atmospheric/ionospheric effects, rather than communications.

## 2.5 RELATIONSHIP TO ADAPTIVE OPTICS

Adaptive optics is a control system for the spatial phase of a beam of light for compensating optical aberrations or changing the spatial phase of a beam of light to create a desired effect. Some alternative technologies are: deconvolution, spatial filtering, null corrector plates, nonlinear phase conjugation. *There is an accent with these on the spatial*. This accent on the spatial (using classical physics) may not be appropriate for laser weaponry and laser communications, for which *there is an accent on the temporal*. POLMOD and AXMOD are temporal, semi-quantum approaches. *In astronomy and imaging, the objective is to preserve spatial information. In communications/weaponry the objective is to preserve information sequence and point focus*. Whereas adaptive optics addresses the *receive side* of the channel, POLMOD/AXMOD addresses the *transmit side*. Therefore, POLMOD/AXMOD offers either an alternative approach to the same problem, or can be used together with (improved) adaptive optics, each addressing one side of the channel.

### 3. MEDIA

The media studied were of three types: (1) water vapor in a chamber (Fig 3.1); (2) heated air (Fig 3.2); and (3) a medium of changing refractive index: either a compact disk cover, or a pseudo-random phase plate (Fig 3.3). The plate was attached to a rotary stage and operated at 5, 20 and 40 rpm.

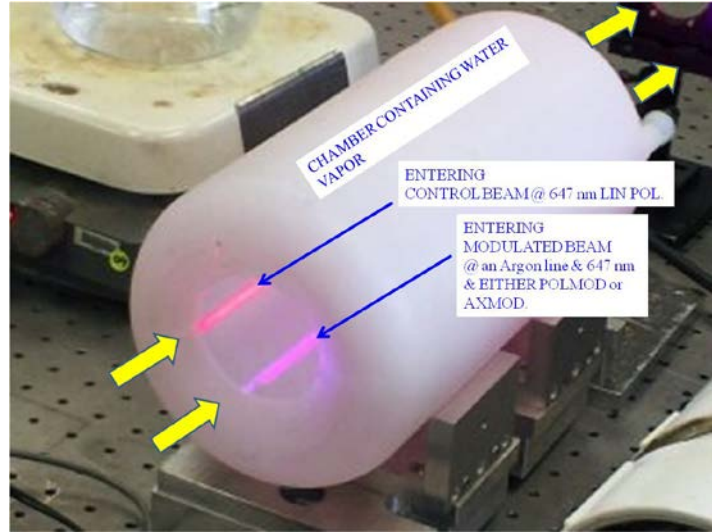


Fig 3.1. Test medium: water vapor arrangement. Water vapor (steam) was passed into the chamber through which the modulated and control beams were passed simultaneously. (Report 12).

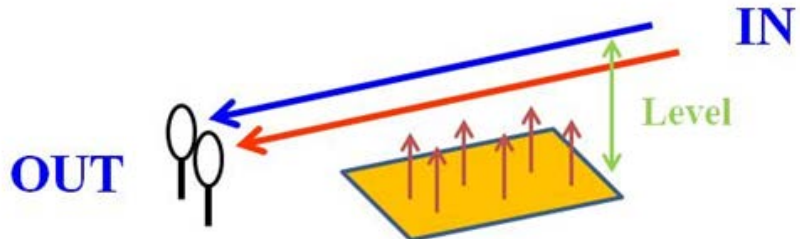


Fig 3.2 Test Arrangement: Hotplate. A hotplate heated air, creating a turbulent condition. Simultaneously, both the test beam (POLMOD) and the control beam were sent over the hotplate at known heights of (1) 2.86 cm, (2) 3.49 cm and (3) 4.76. Two photodiodes recorded the beams entering the turbulent medium (IN) and exiting the turbulent medium (OUT). (Report 13).

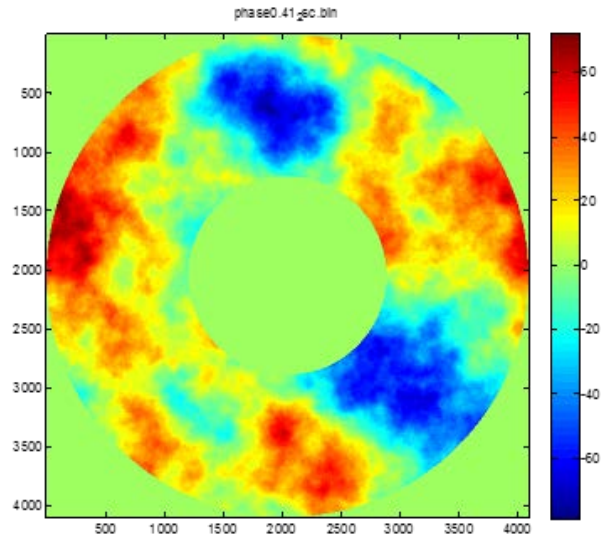


Fig 3.3 Lexitek pseudorandom phase plate, 4 inch square and a  $4096 \times 4096$  array. There is  $-78.7204$  to  $+72.1974$  radians of phase at the design wavelength  $\lambda = 632.8$  nm as indicated on the right.  $0.0008''$  grid spacing yielding 3.277 inch (83.25 mm) diameter. Plate was attached to a rotary stage and was operated at 5, 20 and 40 rpm. Beams were propagated at left ( $225^\circ$ ) at radius 3 inches (0.0762 m). Therefore 5 rpm = 2.39 m/s; 20 rpm = 9.58 m/s; and 40 rpm = 19.15 m/s. (Report 43).

#### 4. LABORATORY TEST CONFIGURATIONS

Below are the test configurations:

- Fig 4.1 Test arrangements – hot plate and vapor chamber media.
- Fig 4.2.1 & 4.2.2 Optical configuration – atmospheric tests.
- Fig 4.3 Test arrangement – hot plate medium.
- Fig 4.4 Laser combination designs.
- Fig 4.5 2 Laser Design – block diagrams and instantiation.
- Fig 4.6 3 Laser Design – block diagrams and instantiation.
- Fig 4.7 Spectra of 2 Laser & 3 laser Designs.
- Fig 4.8 3 Beam Design
- Fig 4.9 3 Beam Design – Phase response
- Fig 4.10 3 Beam Design – Phase response
- Fig 4.11 3 Beam Design – Poincaré sphere and Lissajous representations
- Fig 4.12 3 Beam Design -  $d\varphi/dt$  spectra
- Fig 4.13 3 Beam Design -  $d\varphi/dt$  spectra
- Fig 4.14 Sequence of test recording.

Fig 4.15 provides a description of entropy, Shannon entropy and threshold entropy.

Fig 4.16 is a comparison of 2 and 3 laser test design/configurations.

Figs 4.17-22 address the 3 laser test design/configuration.

Fig 4.23 plots POLMOD inter-beam phase.

Fig 4.24 illustrates POLMOD Lissajous patterns.

Fig 4.25 provides phase rate-of-change plots.

Fig 4.26 is a phase modulation representation.

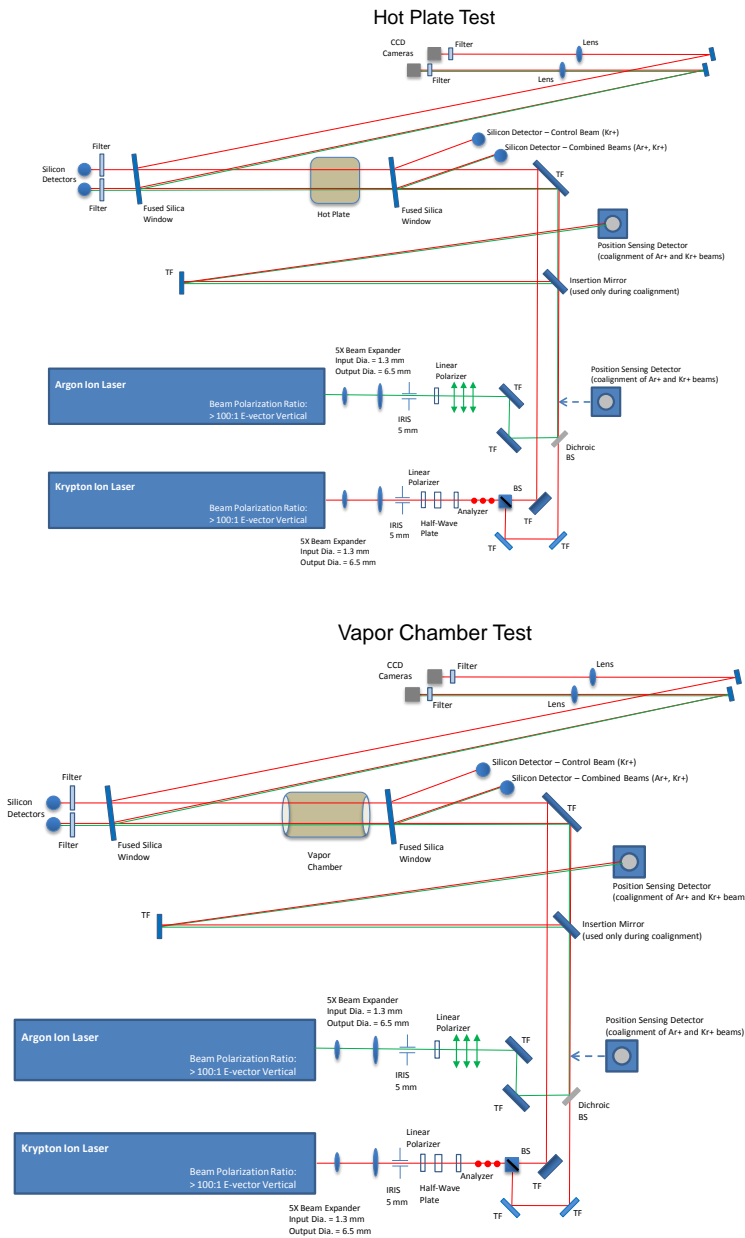
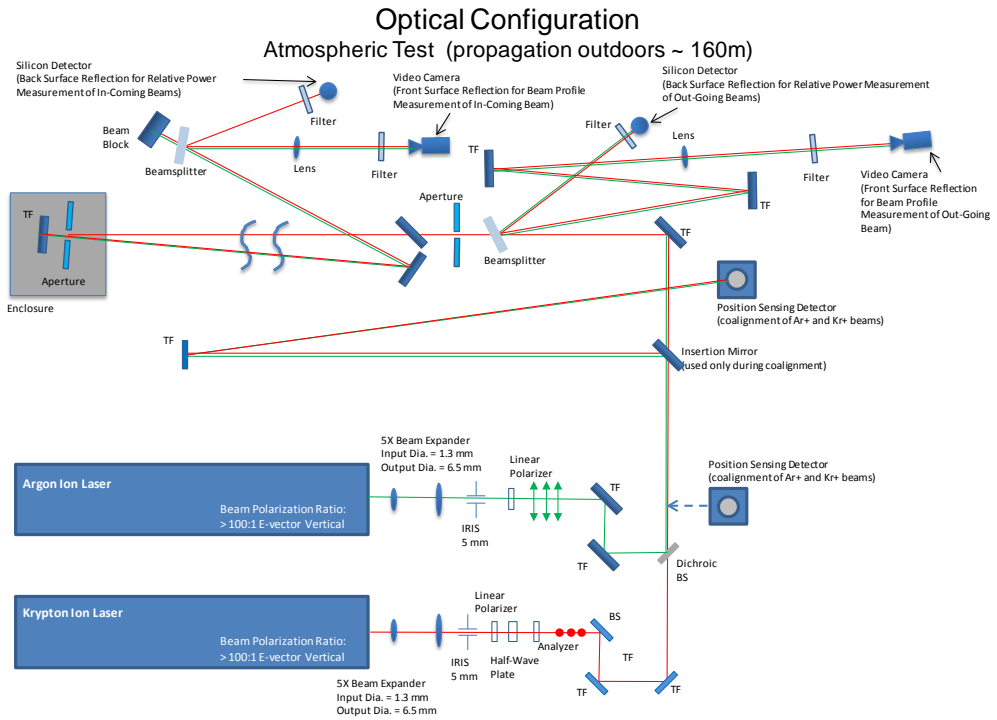


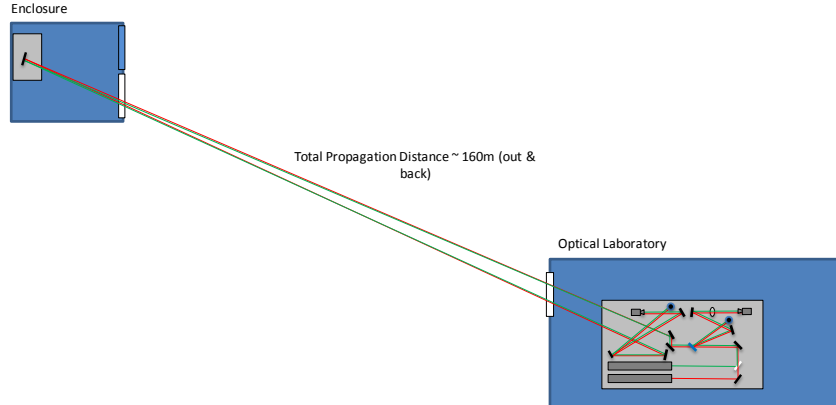
Fig 4.1 The test arrangements (courtesy Kevin Suter) for hot plate and vapor chamber arrangements. (Report 21).



**A**

### Beam Propagation Path

Polarization Modulation Testing – August 26-30, 2013



**B**

Fig 4.2.1

A: Test Optical Configuration atmospheric tests.

B: beams were propagated over 80 meters – 160 meters outgoing and incoming. (courtesy, Kevin Suter.) (Report 26)



**C**



**D**

Fig 4.2.2

C: Down range from the optical laboratory: 80 meters each way; 160 meters two-way.

D: Closeup of down range. (Report 26)

## Optical Configuration

## Atmospheric Correction - Hot Plate

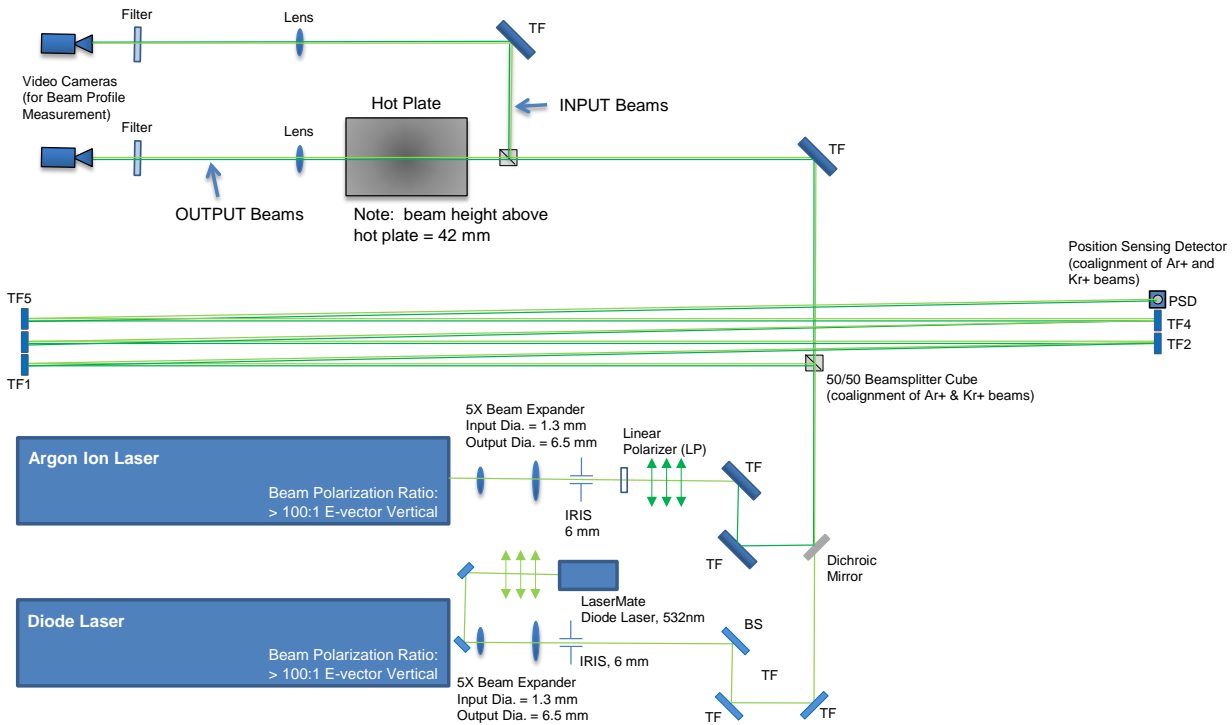


Fig 4.3 The Test arrangement, hot plate medium. Beam elevation above hot plate: 42.0 mm. Path length: 50.5 feet. Diode laser,  $\lambda = 532$  nm. Krypton laser,  $\lambda = 456, 476, 488$  or  $514$  nm. (Report 33)

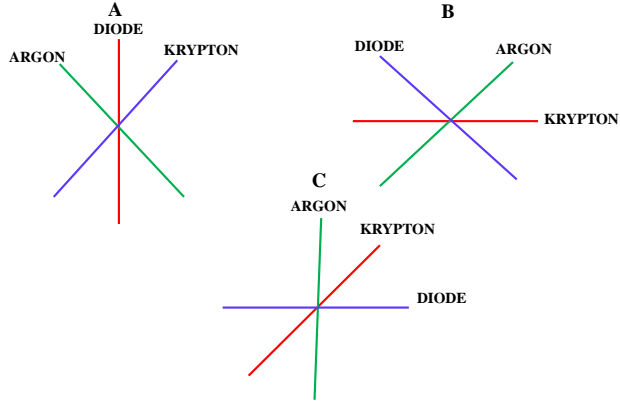


Fig 5.4 Laser combining designs for POLMOD (Report 36)

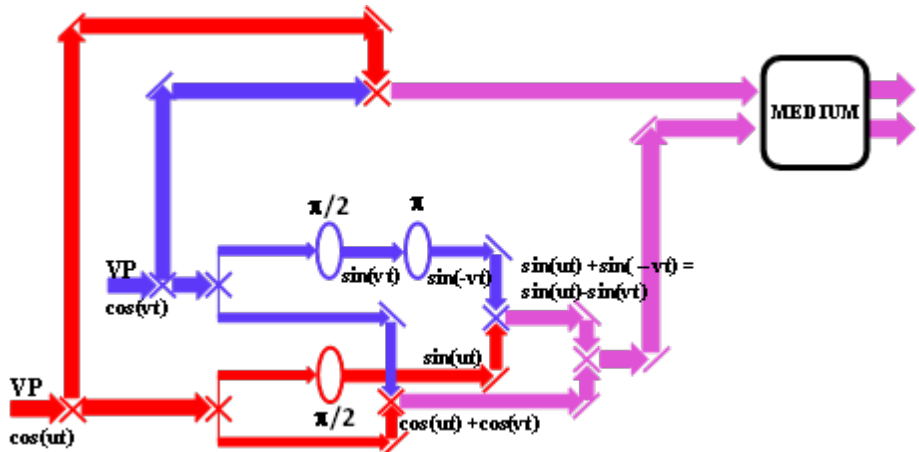


Fig 4.5.1 2 Laser Algebraic design: Two laser, Two polarization combinations. Two laser beams of different frequencies,  $u$  and  $v$ , are combined on two orthogonal channels, such that:

$$HP = 2\cos\left(\frac{u+v}{2}t\right)\cos\left(\frac{u-v}{2}t\right) = \cos(ut) + \cos(vt),$$

$$VP = 2\cos\left(\frac{u+v}{2}t\right)\sin\left(\frac{u-v}{2}t\right) = \sin(ut) - \sin(vt).$$

The 2 laser beams are split creating 4 beams. The horizontally polarized channel,  $\cos(ut) + \cos(vt)$ , is easily achieved by beam addition and then rotation. The vertically polarized channel,  $\sin(ut) - \sin(vt)$ , is achieved by the following: (a) Commence with  $\cos(ut)$  and  $\cos(vt)$ , separately, and delay each constituent beam by  $\pi/2$ , separately, to obtain one  $\sin(ut)$  and one  $\sin(vt)$ . (b) Delay the  $\sin(vt)$  by  $\pi$  to obtain  $\sin(-vt)$ . (c) Add  $\sin(-vt)$  to  $\sin(ut)$  to obtain  $\sin(ut) + \sin(-vt) = \sin(ut) - \sin(vt)$ . Finally, combine the vertically and horizontally polarized channels. In the above scheme, the  $\pi/2$  and  $\pi$  delays can be combined into one  $3\pi/2$  delay. The medium in the present series of tests was the rotating phase plate of Fig 4.3. (Report 43)

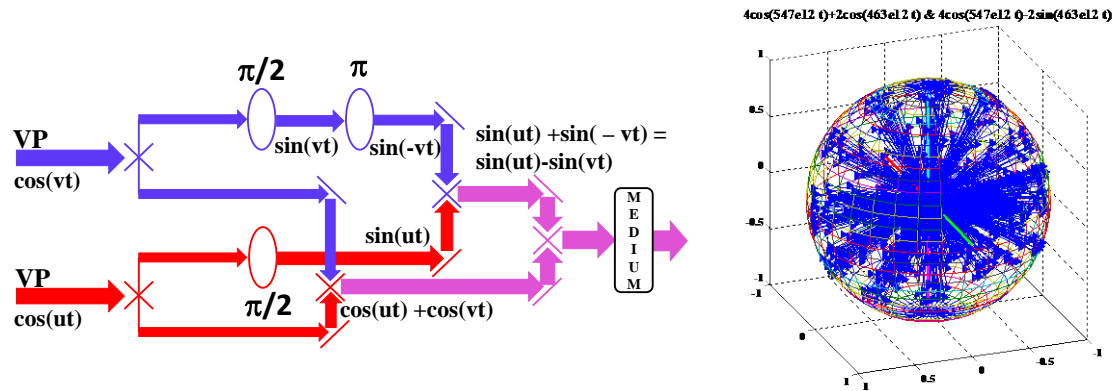


Fig 4.5.2 Two Laser Algebraic Design (Report 37)

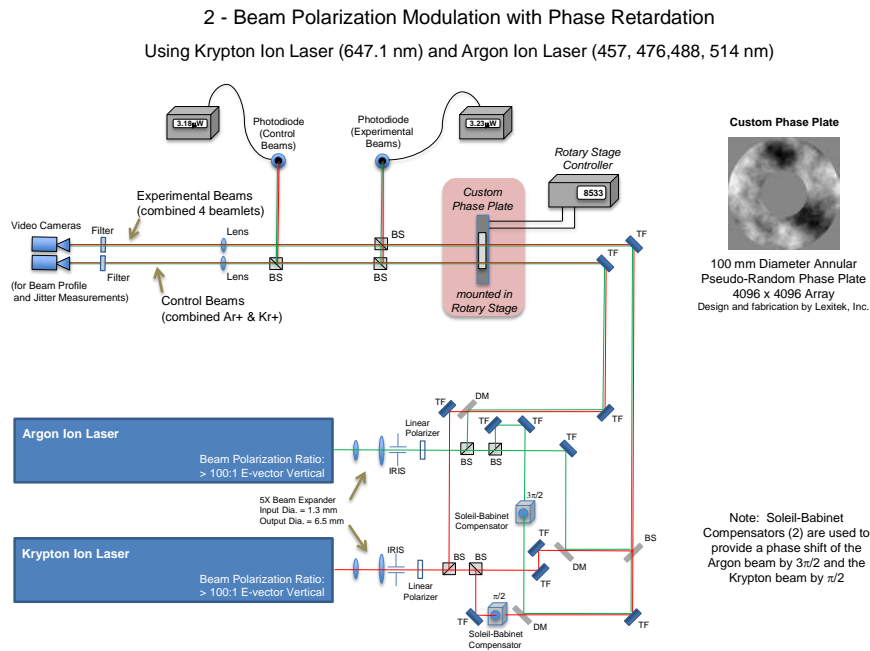


Fig 4.5.3 The instantiation used in the tests reported of the block diagram of Figs 5.5A & B. The video cameras sampled at 30 frames/sec and the power meters sampled at 250 Hz. Courtesy Kevin Suter. (Report 43)

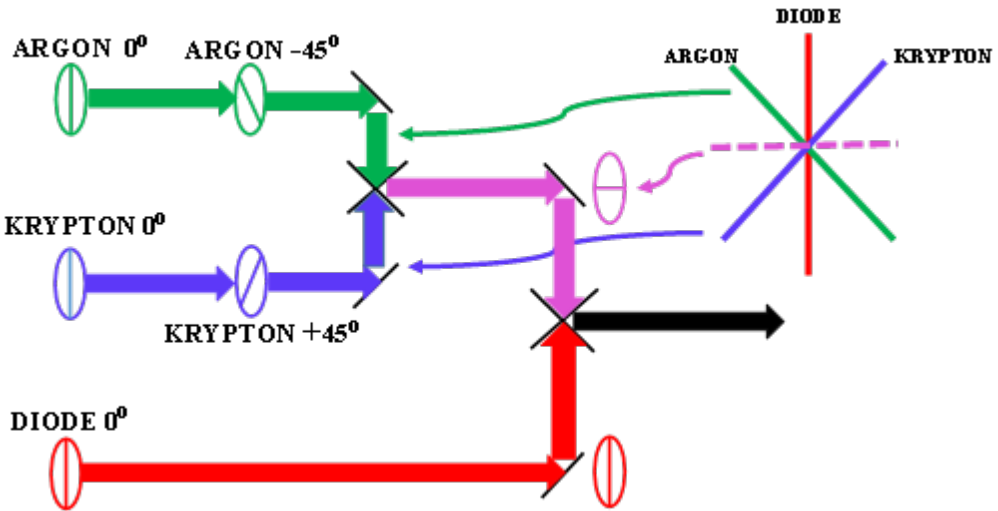


Fig 4.6.1 3 Laser Design: A 3 beam combination providing 3-POLMOD. Given incident beams of different wavelengths that are initially linearly polarized vertically, two rotators – for  $+45^\circ$  and  $-45^\circ$  rotate the Ar+ and Kr+ beams. These two beams are combined to form a beam orthogonal to the diode laser beam. This combined beam is then combined orthogonally with the diode laser beam. In the tests reported here, the Krypton beam was set at  $\lambda = 647$  nm; the diode beam was set at  $\lambda = 532$  nm; and the Argon beam was set at one of the 4  $\lambda$ s: 457, 476, 488 or 514 nm. (Report 43)

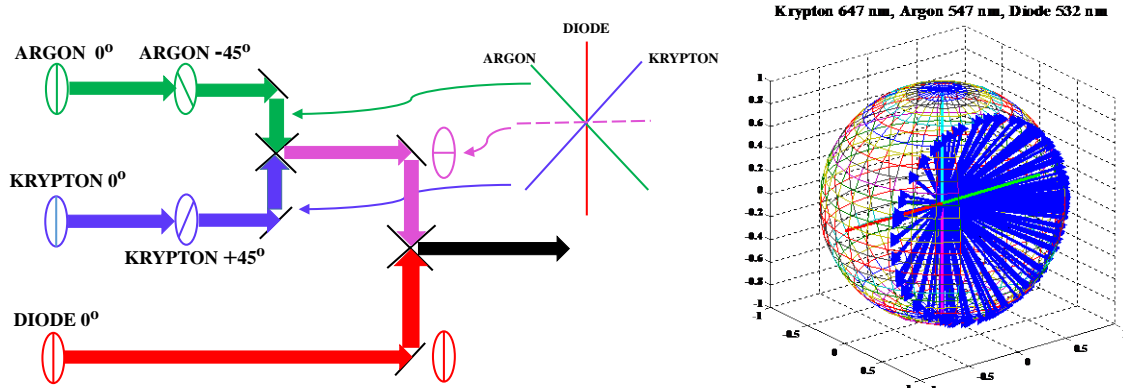


Fig 4.6.2 3 Laser Design: A 3 beam combination providing 3-POLMOD. (Report 37)

### 3 – Beam Polarization Modulation Test Series

Using Krypton Ion Laser (647.1 nm), Diode Laser (532 nm), and Argon Ion Laser (457, 476, 488, 514 nm)

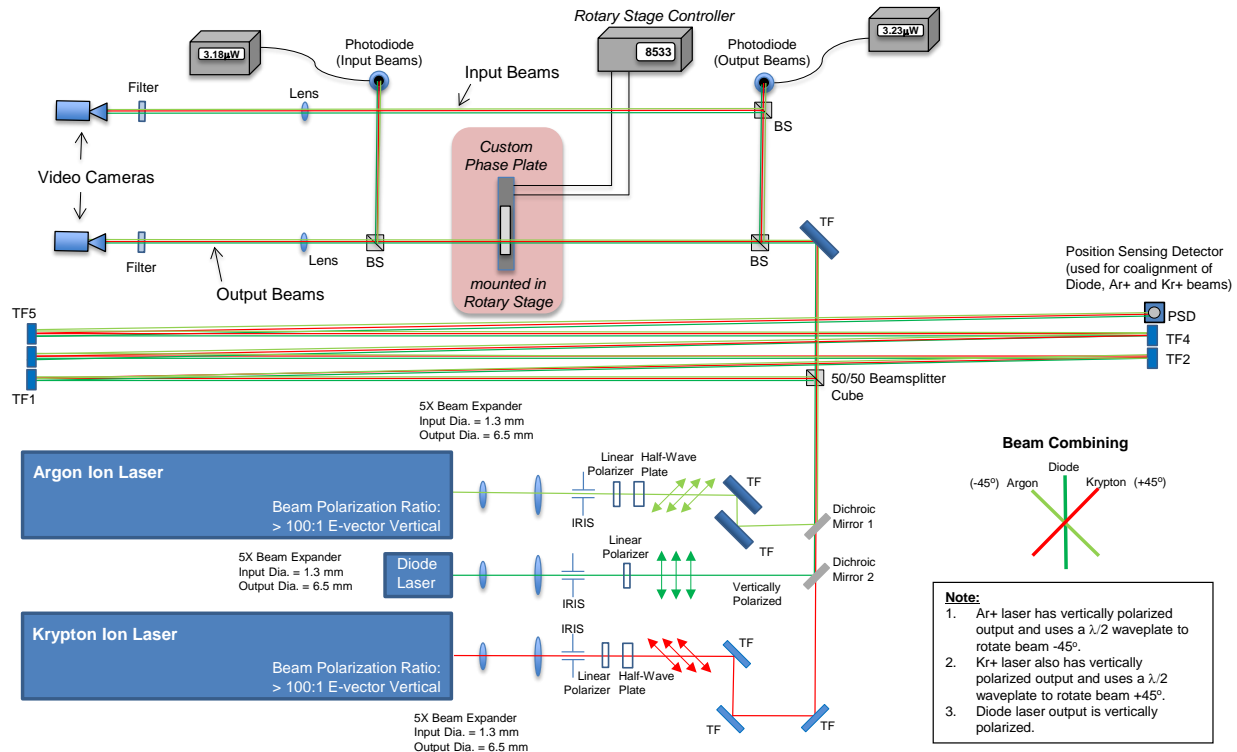
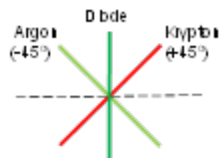


Fig 4.6.3 3 Laser Design: The instantiation used in the tests reported of the block diagram of Figs (5.6A & B). The video cameras sampled at 30 frames/sec and the power meters sampled at 250 Hz. Courtesy Kevin Suter. (Report 43)

## Beam Combining and Test Sequences

### 3-Beam Combination:

- Argon Ion laser beam is vertically polarized out of laser; uses  $\lambda/2$  waveplate to rotate beam  $-45^\circ$ .
- Diode laser beam is vertically polarized; uses linear polarizer to ensure vertical polarization.
- Krypton Ion laser beam is vertically polarized out of laser; uses  $\lambda/2$  waveplate to rotate beam  $+45^\circ$ .



### Test Sequences:

- 2-Line Sequence (35 seconds duration for each test run)
  - 5-seconds background (beams blocked)
  - 10-seconds Diode laser beam only
  - 10-seconds Ar+ beam combined with Kr+ beam
  - 10-seconds all three beams
  - Power in Diode beam = Power Ar+ beam + Power Kr+ beam
- 3-Line Sequence (45 seconds duration for each test run)
  - 5-seconds background (beams blocked)
  - 10-seconds Ar+ beam only
  - 10-seconds Diode beam only
  - 10-seconds Kr+ beam only
  - 10-seconds all three beams
  - Power in Diode beam = Power Ar+ beam = Power Kr+ beam

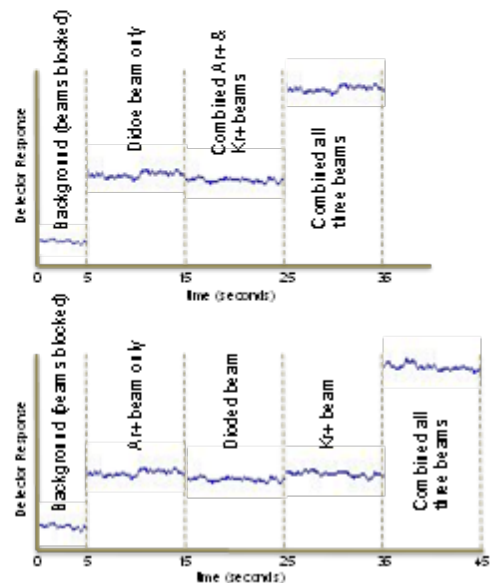


Fig 4.14 The sequence of test recording. In this Part 1 test report, results of the 2-Line Sequence is reported (top). Note that the Power of Diode beam = Power Ar beam + Power Kr beam. Note also, that this sequence method assumes that the dielectrics of the medium are stationary in the time of recording across the sequence. This only the case for the CD cover. (Reports 38 & 43).

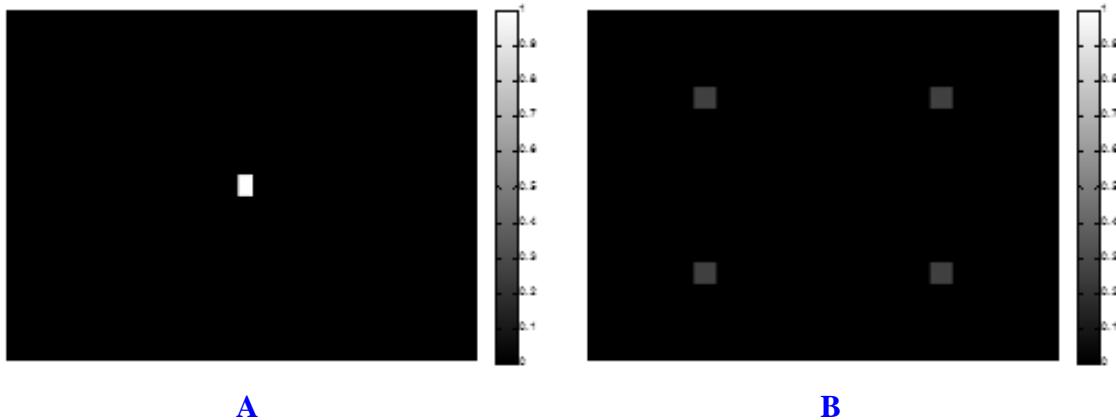


Fig 4.15 Above, are two  $640 \times 280$  “images”. In A, all the energy is “focused” on one location; in B the energy is dispersed to four locations with  $\frac{1}{4}$  of the energy of A in each location – as in an averaged image of a beam dispersed by the medium through which it has passed.

- (1) The entropy of image A is 0.2482, and of B is 0.9888, i.e.,  
 $\text{Entropy}_B > \text{Entropy}_A$ .
- (2) The Shannon wave packet entropy of image A is  $1.3921\text{e+003}$ , and of B is  $5.8919\text{e+003}$ , i.e.,  
 $\text{Shannon\_entropy}_B > \text{Shannon\_entropy}_A$ .
- (3) The Threshold wave packet entropy of image A is 4392, and of B is 20992. i.e.,  
 $\text{Threshold\_entropy}_B > \text{Threshold\_entropy}_A$ .

We see that an average image dispersed by spatial jitter – image B – has more randomness than a less dispersed average image – image A – as shown by 3 measures of entropy. (Report 44. SEP\_2014\_VIDEO\_CAMERAS.)

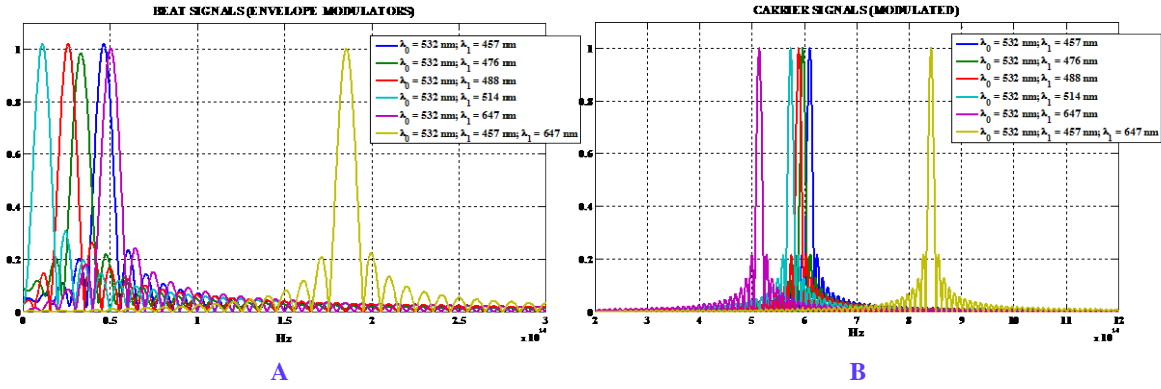


Fig 4.16 A comparison between 2- and 3-Laser Designs. A: envelopes (beat signal) and B: carriers of 2-POLMOD and a 3-POLMOD signal.

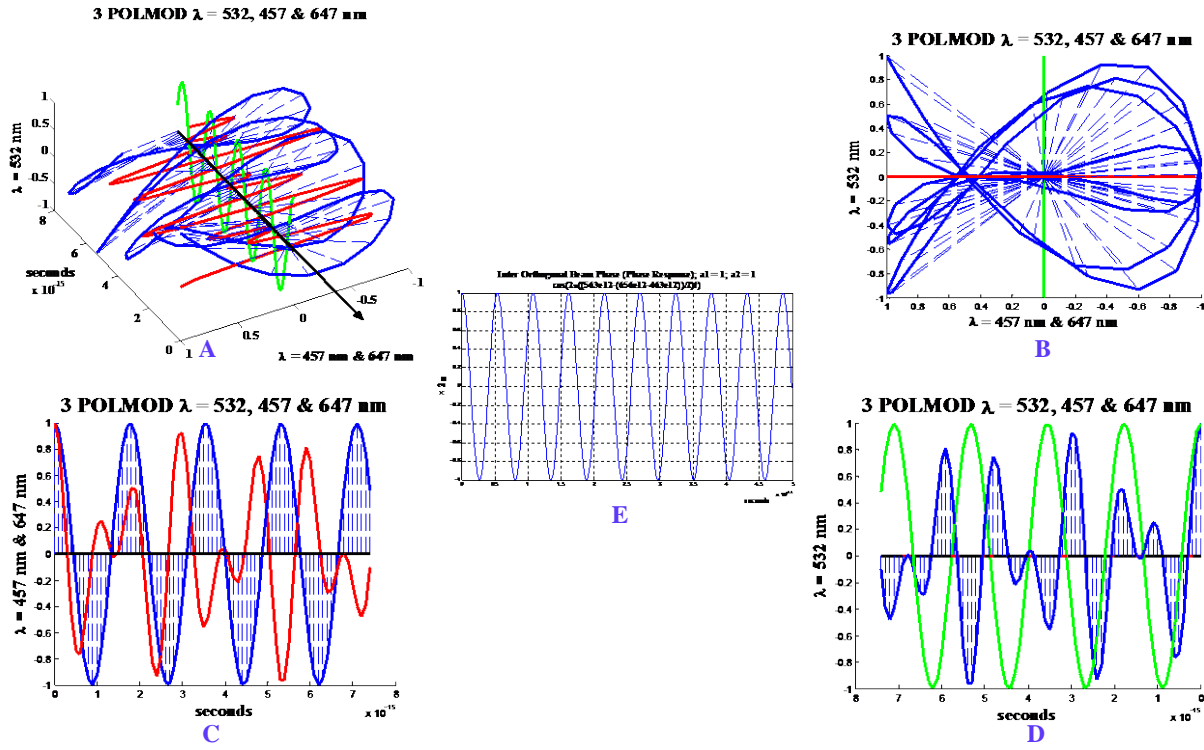


Fig 4.17 3 Laser Design: A 3-POLMOD signal composed of  $\lambda = 532, 457$  and  $647 \text{ nm}$  components, according to the Fig 1A configuration. Phase response:  $\cos(2\pi((563e12 - (656e12 - 463e12))/2)/2)t$ . Three lasing lines:  $\lambda = 532, 457$  and  $647 \text{ nm}$ . Phase modulation rate (C2) is  $\sim 200 \text{ THz}$ . (Report 36. PP: POLMOD 3 BEAMS).

### Krypton 647 nm, Argon 547 nm, Diode 532 nm

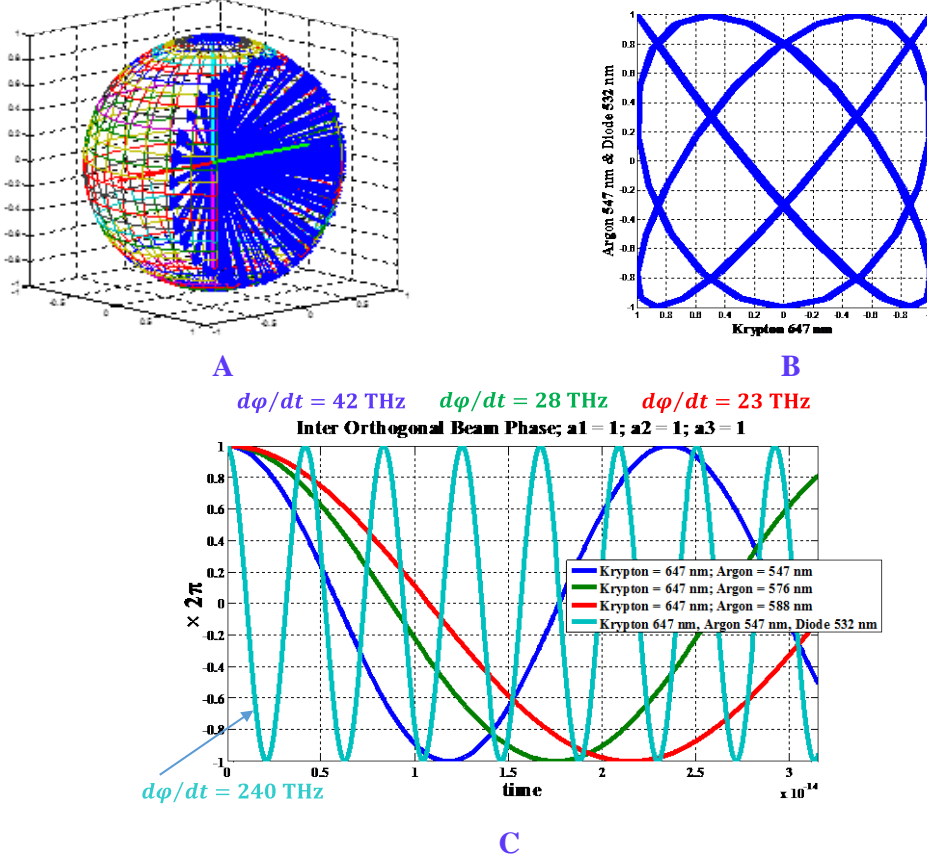


Fig 4.18 3 Laser Design: A 3-POLMOD signal composed of  $\lambda = 532, 457$  and  $647$  nm components, according to the Fig 1A configuration. A: Poincaré sphere representation; B: Lissajous pattern; C: Phase response:  $\cos(2\pi((647e12 - (548e12 - 563e12))/2)/2)t$ . Note the 3-POLMOD higher frequency compared with the 2-POLMOD phase modulation. Three lasing lines:  $\lambda = 532, 547$  and  $647$  nm. Phase modulation rate is  $\sim 260$  THz. Compare with Fig 4, where  $\lambda = 457$  was substituted for  $\lambda = 547$  nm. (Report 36)

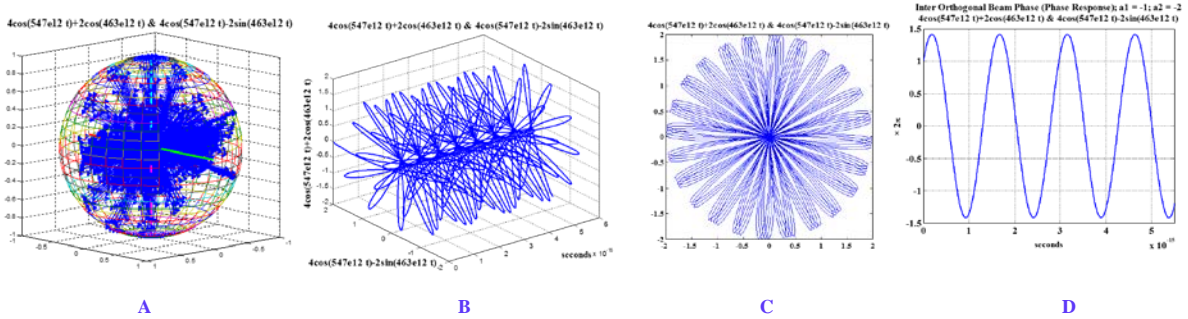


Fig 4.19 3 Laser Design: POLMOD phase modulation rate:  $\sim 660$  THz.  
 $\lambda_1 = 647$  nm ( $f_1 = 463$  THz);  $\lambda_2 = 547$  nm ( $f_2 = 548$  THz).  
 Orthogonal Beam<sub>1</sub> =  $4 \cos(547e12t) + 2\cos(463e12t)$   
 Orthogonal Beam<sub>2</sub> =  $4 \sin(547e12t) - 2\sin(463e12t)$ .  
 A: Poincaré sphere representation; B & C: Representations over time in Lissajous pattern form; D: Phase response:  $\sim 660$  THz. (Report 36. PP: POLMOD\_3\_BEAMS)

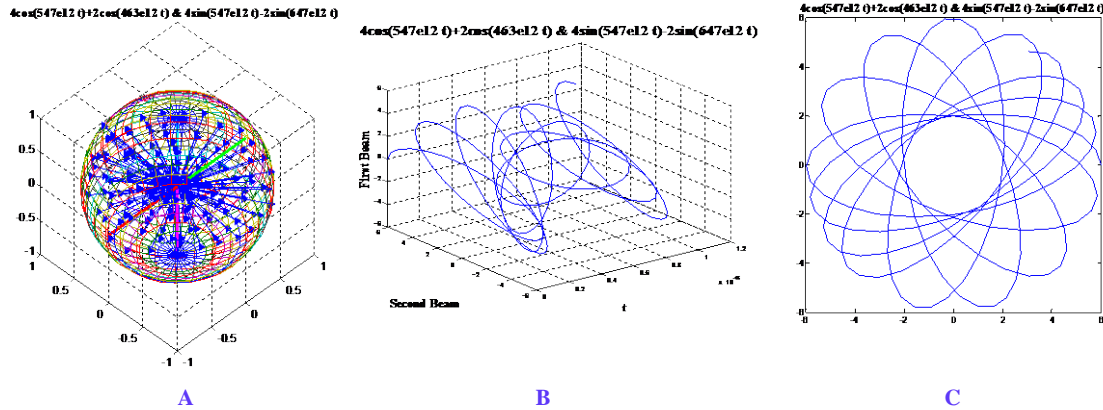


Fig 4.20 3 Laser Design. (PP: POLMOD\_3\_BEAMS).

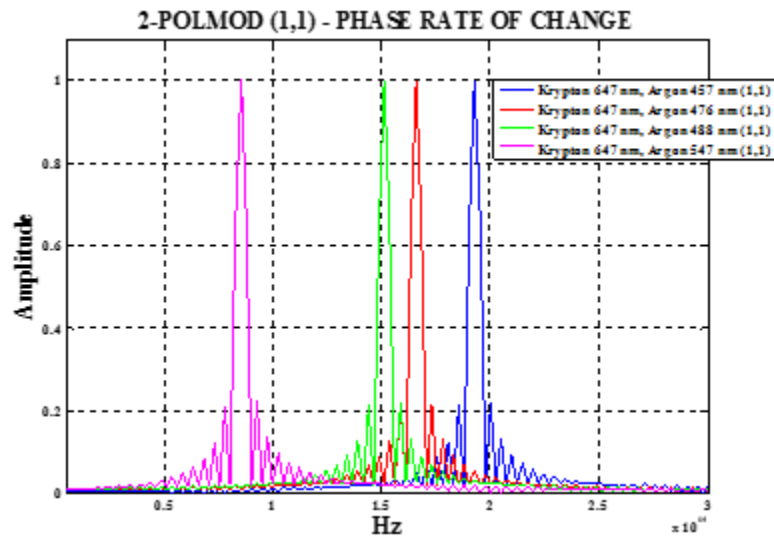


Fig 4.21 2 Laser Design. Phase Rate of Change  $d\varphi/dt$  – Algebraic Design. Frequencies are:  
 193 THz (647+457 nm, orthogonal)  
 166 THz (647+476 nm, orthogonal)  
 151 THZ (647+488 nm, orthogonal)  
 85 THz (647+547 nm, orthogonal)  
 (Report 43).

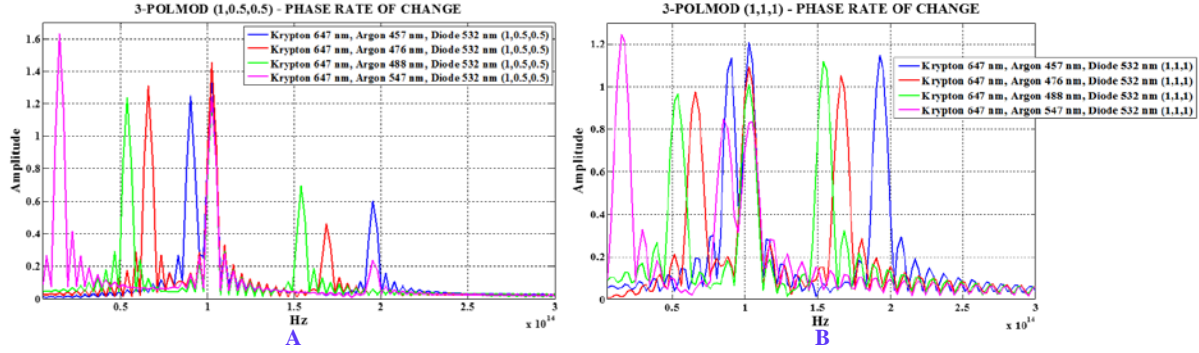


Fig 4.22 3 Laser Designs. Frequency domain (spectra)  $d\varphi/dt$  phase-rate-of-change. Upper: 2-Line sequence. Lower 3-Line sequence. There are differences in the spectra between the 2-Line sequence and the 3-Line sequence method testing but they are minor. Notice that phase modulation rates can be almost as high as 200 THz. (Report 41)

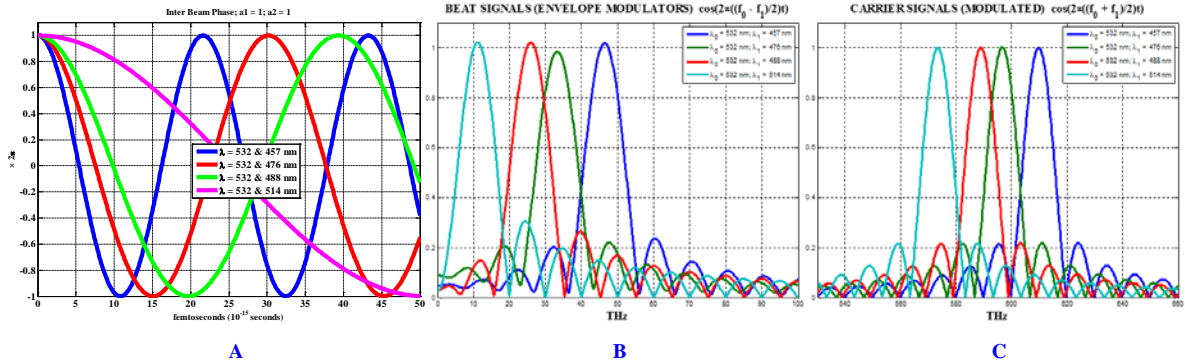


Fig 4.23 Interbeam Phase.

A: The interbeam phase changes at a uniform rate. The most rapid change is that of the  $\lambda = 532 \text{ & } 457 \text{ nm}$  combined beam. The slowest is that of the  $\lambda = 532 \text{ & } 514 \text{ nm}$  beam.

B: From the perspective of a receiver/absorber of single polarization, the combined beams are periodic beat waves. If  $f_0$  is the frequency of the longest wavelength of the combined beam –  $\lambda_0 = 532 \text{ nm}$  in the present case – and  $f_1$  is the wavelength of the shortest wavelength of the combined beam, then the envelope of the beat signal is given by:  $\cos(2\pi \left[ \frac{f_0 - f_1}{2} \right] t)$ .

C: If  $f_0$  is the frequency of the longest wavelength of the combined beam –  $\lambda_0 = 532 \text{ nm}$  in the present case – and  $f_1$  is the wavelength of the shortest wavelength of the combined beam, then the carrier of the beat signal is given by:  $\cos(2\pi \left[ \frac{f_0 + f_1}{2} \right] t)$ . (Report 33. POLMOD\_BEAT\_WAVES\_03)

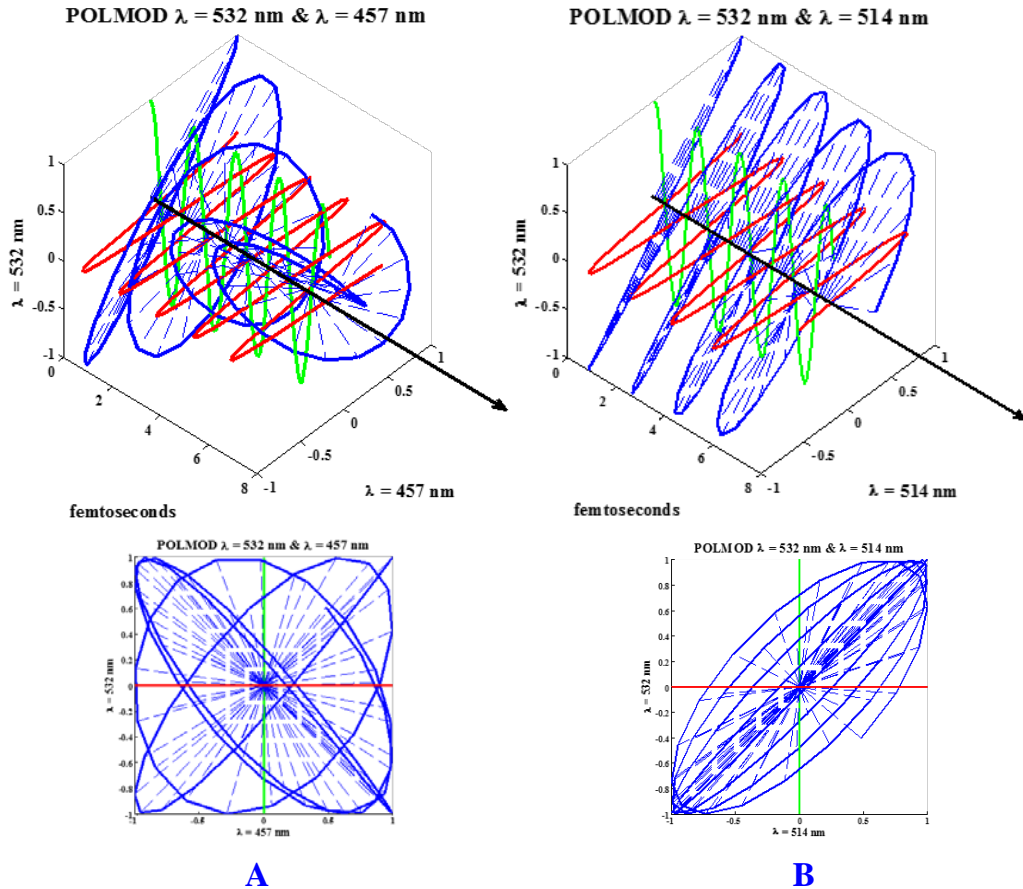


Fig 4.24

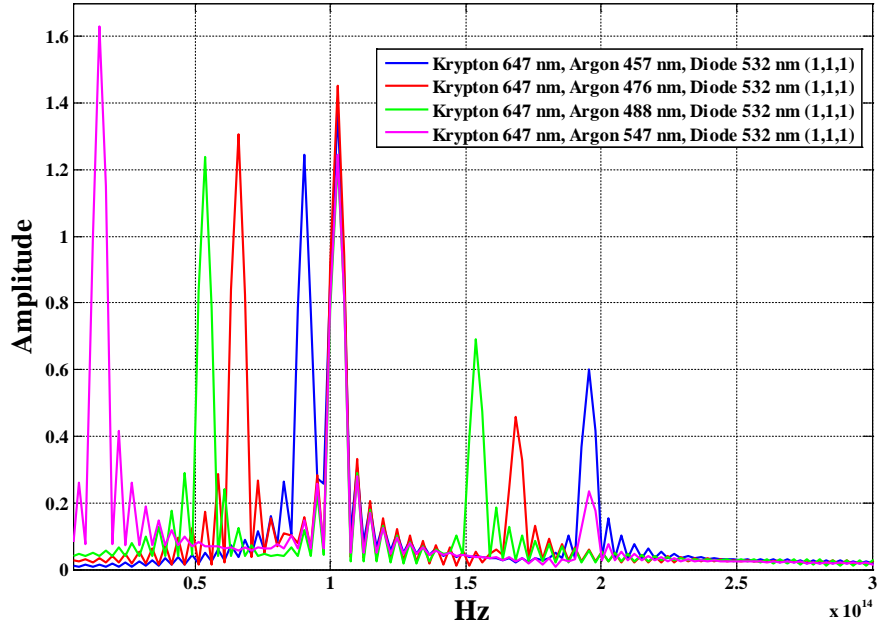
A: Upper: A POLMOD beam (blue) represented over 8 femtoseconds and formed from orthogonal  $\lambda = 457$  nm (red) and  $\lambda = 532$  nm (green) beams.

A: Lower: The same beam viewed head-on and forming a Lissajous pattern (over 8 femtoseconds.)

B: Upper: A POLMOD beam (blue) represented over 8 femtoseconds and formed from orthogonal  $\lambda = 514$  nm (red) and  $\lambda = 532$  nm (green) beams.

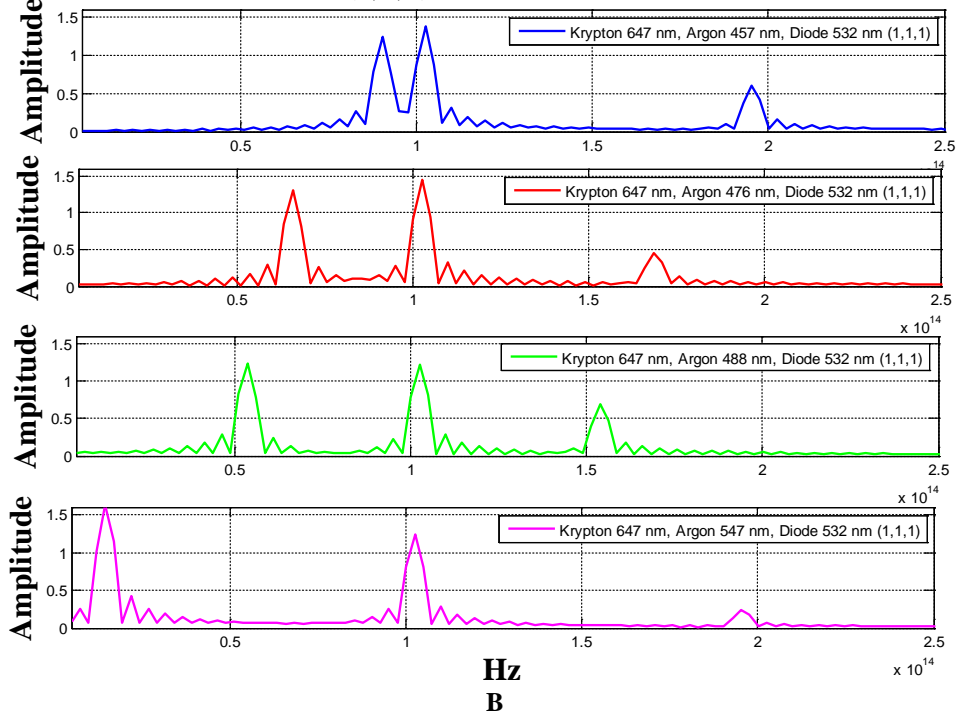
B: Lower: The same beam viewed head-on and forming a Lissajous pattern (over 8 femtoseconds.) (Report 33. POLMOD\_BEAT\_WAVES\_03)

### 3-POLMOD (1,1,1) - PHASE RATE OF CHANGE



A

### 3-POLMOD (1,1,1) - PHASE RATE OF CHANGE



B

Fig 4.25 Phase Rate of Change  $d\varphi/dt$ , – 3 Beam Design. B is an exploded version of A. Frequencies from highest to lowest amplitude are:

103, 90, 195 THz (647 + 457 + 532 nm, orthogonal)

103, 66, 169 THz (647 + 476 + 532 nm, orthogonal)

103, 53, 169 THZ (647 + 488 + 532 nm, orthogonal)

14, 103, 195 THz (647 + 547 + 532 nm, orthogonal)

(Report 43)

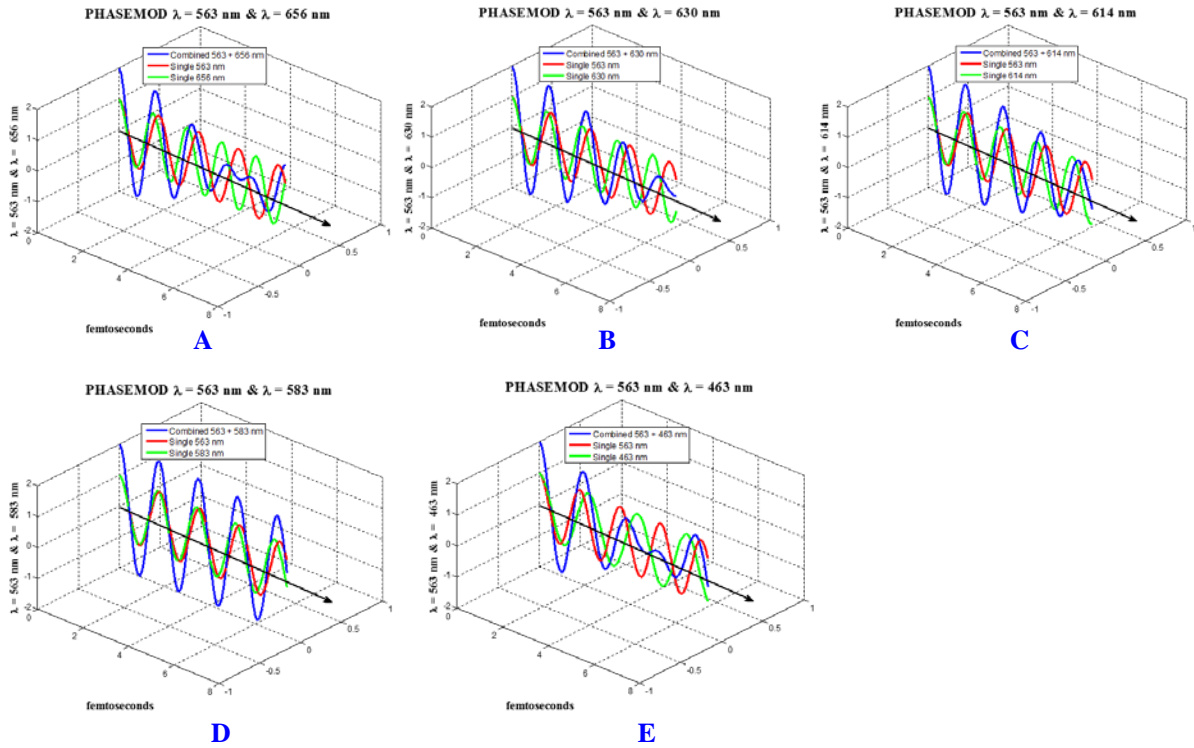


Fig 4.26 Phase Modulation (AXMOD) = 563 nm + (A) 656 or (B) 630 or (C) 614 or (D) 583 or (E) 463 nm. Notice that (A) & (E) provide a similar combined beam – this is because modulated and modulator change roles. (Report 33; POLMOD\_BEAT\_WAVES\_03; POWERPOINT POLMOD\_JAN\_2014\_REPORT\_33; POLMOD\_BEAT\_WAVES\_03)

## 5. TEST RESULTS

### 5.1 DATA ANALYSIS METHODS

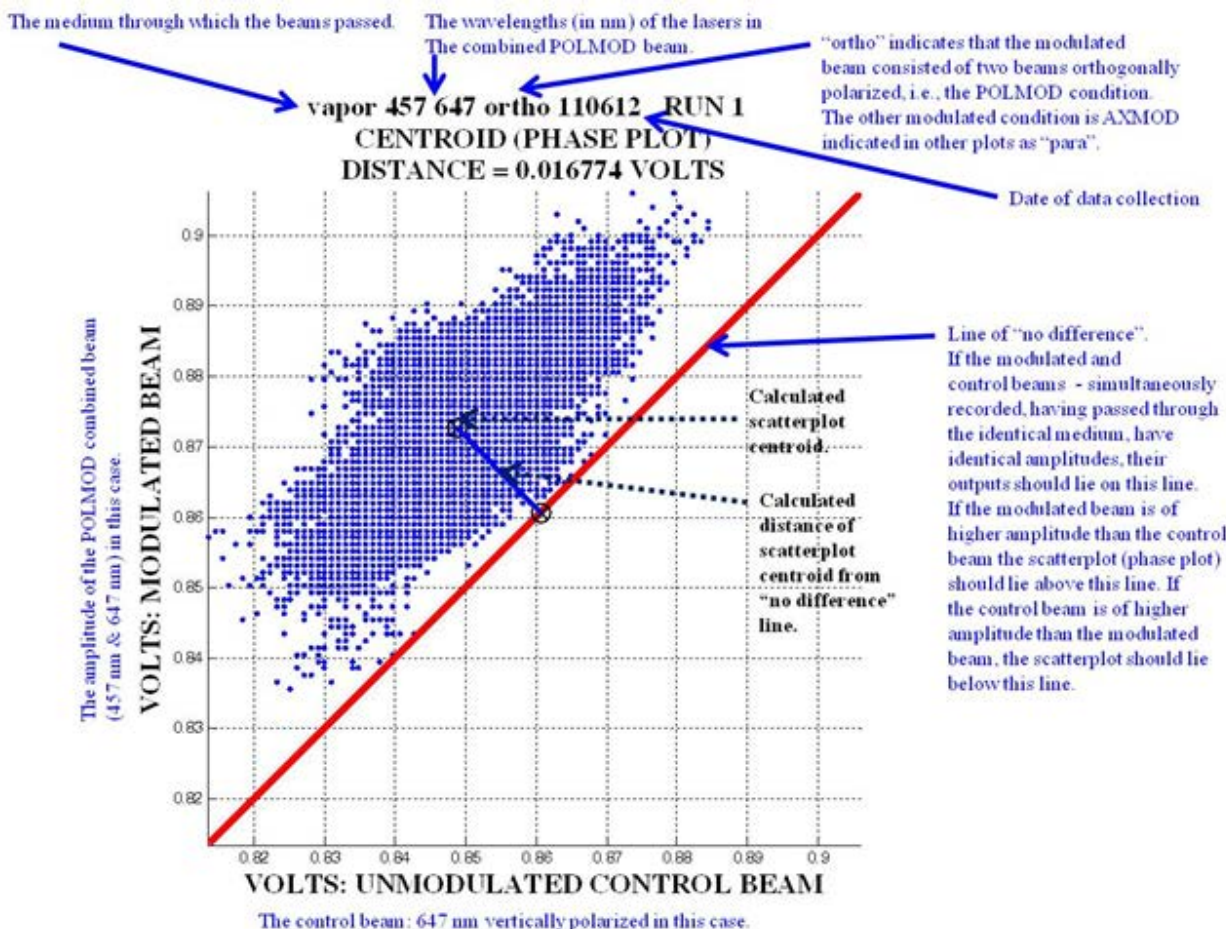
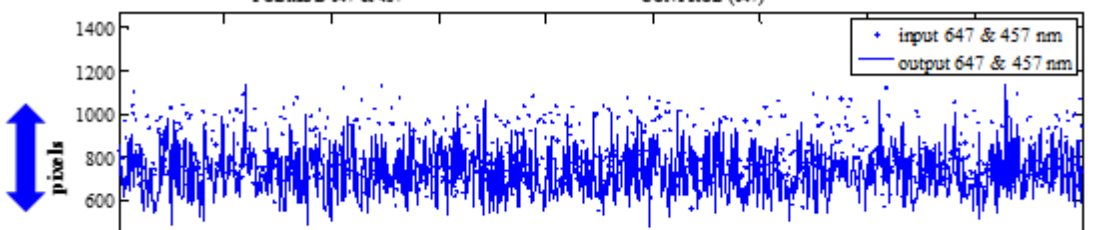
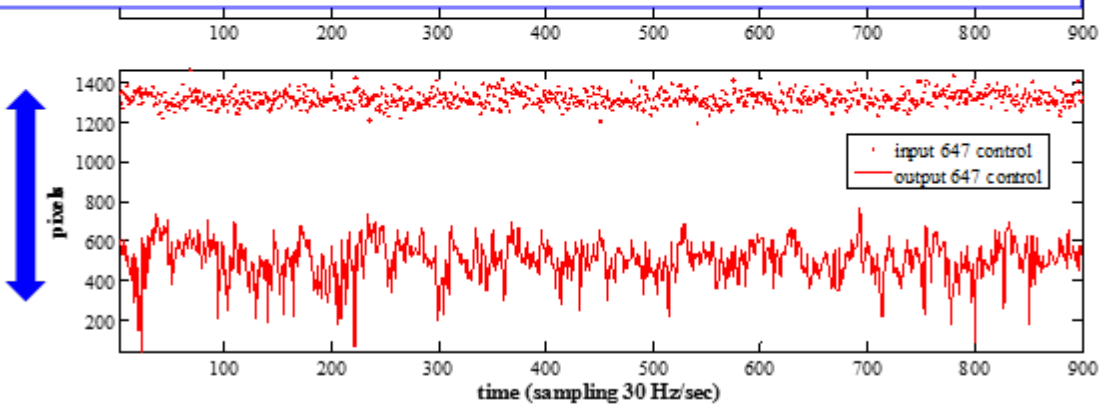


Fig 5.1.1 A data analysis method – one of a number: Water Vapor – see Fig 3.1, above. Besides recordings from the modulated (here: 457 nm & 647 orthogonally polarized) and the control (here: a single beam at 647 nm, linearly polarized) beams exiting the medium, the “background” – or no input – condition, and the “input” – the beam amplitudes prior to entering the medium – condition, were also recorded. The two beams, modulated and unmodulated or control – were aligned at the same amplitude. The data for the two conditions – modulated and control - were recorded at 30 Hz exiting the medium. The data were further treated by (1) subtracting the mean of the background from the medium-exiting or output amplitude, and (2) dividing by the mean of the medium-entering or input amplitude. This treated data were displayed in a phase, or scatterplot, shown here. The scatterplot thus removes the time variable. The centroid for the data, and the distance from the center line of “no difference” between the modulated and control conditions were then calculated. (Report No 12).

WATER VAPOR TEST, CONTOUR AREA, Polarization Modulation: raw scores: Krypton  $\lambda = 647$  nm, Argon  $\lambda = 457$  nm  
 $\sigma_{\text{POL MOD 647 \& 457}} \text{ out/in ratio} = 1.0189$     $\sigma_{\text{CONTROL (647)}} \text{ out/in ratio} = 2.7013$



POLMOD BEAM INPUT (PRIOR TO WATER VAPOR CHAMBER) IS NOISY, BUT THE STANDARD DEVIATION AND THE MEAN CHANGES MINIMALLY AFTER PASSING THROUGH WATER VAPOR.



THE MEAN OF THE UNMODULATED BEAM DIMINISHES AND THE STANDARD DEVIATION INCREASES AFTER PASSING THROUGH WATER VAPOR.

Fig 5.1.2 A Typical Result – Water Vapor Medium – see Fig 3.1 above. In all cases tested, (1) the modulated beam was noisier than the control beam even before entering the chamber, but (2A) the relative reduction in the mean of the entering (input) to the chamber vs. exiting (output) beam from the chamber, was greater for the control beam, and (2B) the relative increase in the standard deviation of the entering (input) to the chamber vs. exiting (output) beam from the chamber, was also greater for the control beam. Thus, while the modulated beam was noisier regardless of the medium, the beam was remarkably stable after passing through the medium. Why the modulated beam is noisier is unclear. All the results for all the tested conditions – (HELSTF\_NOV\_2012\_ANALYSIS\_WATER\_VAPOR\_PD, Report No 14)

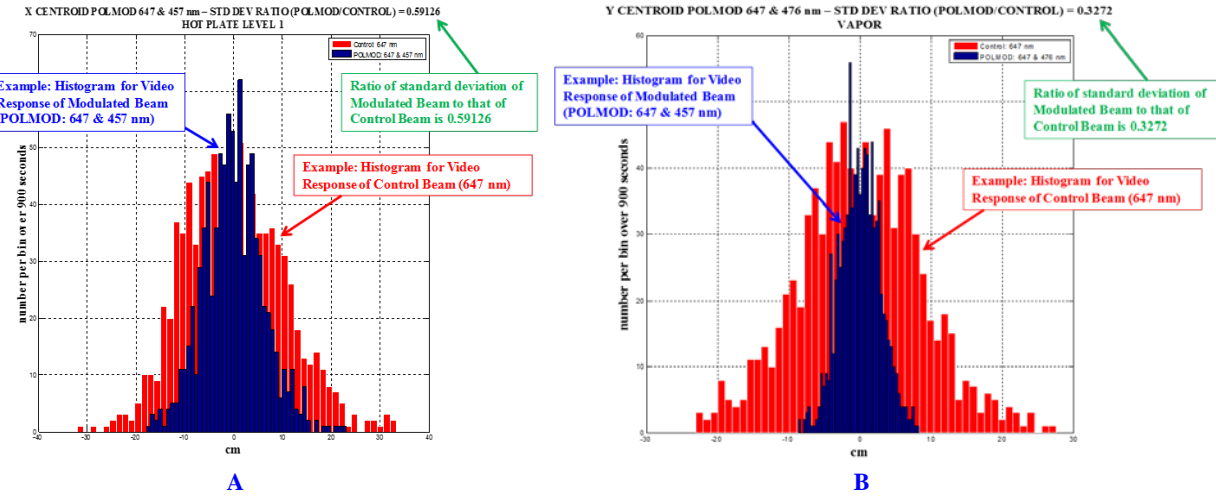


Fig 5.1.3 An example of the analysis procedure. (A) Medium: Heated Air (see Fig 3.2, above). (B) Water Vapor (see Fig 3.1, above) The statistical measure is the x centroid and histogram bin counts were calculated for both control (the 647 nm beam – in red) and the modulated (the 647 & 457 nm beam – in blue) – POLMOD in this case. The result for the modulated beam is overlaid on that for the control beam. The standard deviations were taken from the original data, and the ratio – modulated beam to control beam calculated. In this case it is 0.59126, indicating a decrease in the jitter for the modulated beam. Both beams are of equal entering-medium power. In this example, the level of the beams above the hot plate was Level 1. (Reports 17 & 18)

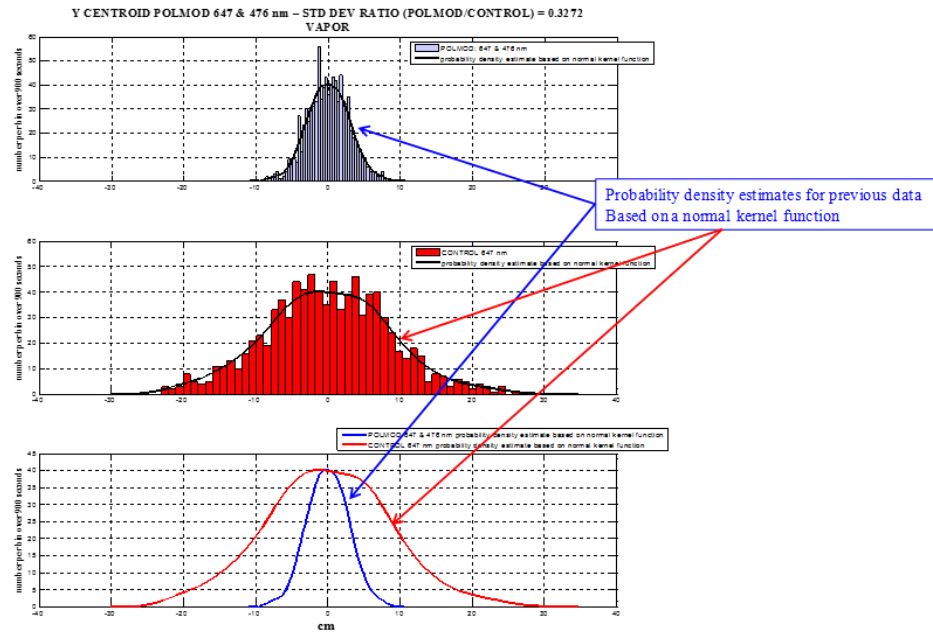


Fig 5.1.4 Medium: Water Vapor (see Fig 3.1, above). A example of continuation of the analysis procedure. Probability density measures were calculated based on a normal kernel function for the data of Fig 3A. An easily visualized comparison of the control and modulated beam can then be made – lower figure. (Reports 17 & 18)

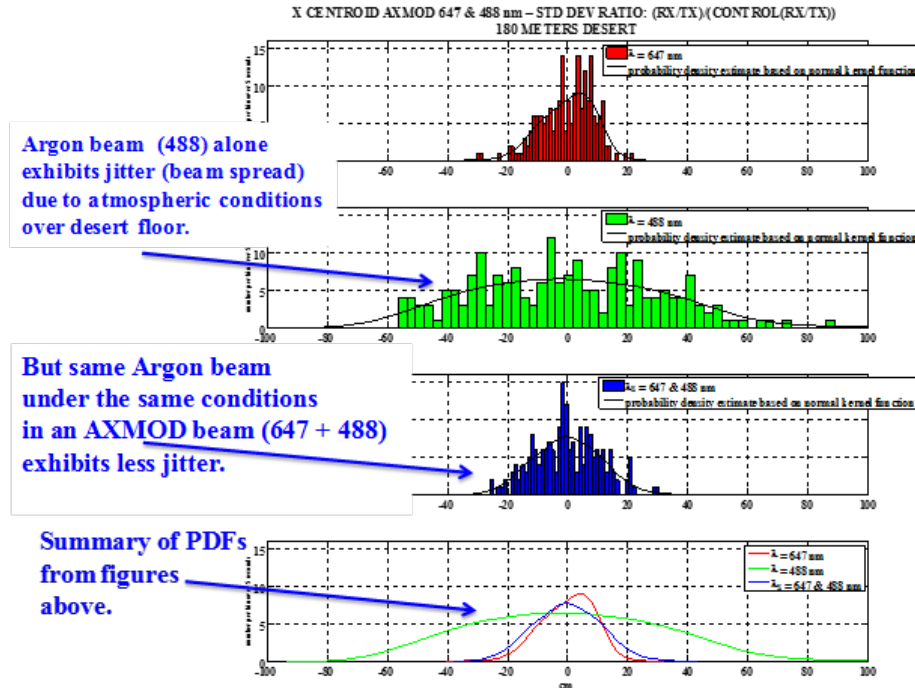


Fig 5.1.5 Medium: Power meter tests conducted for propagation over 160 meters of desert (see Figs 4.2.1 & 4.2.2, above). (Report 26)

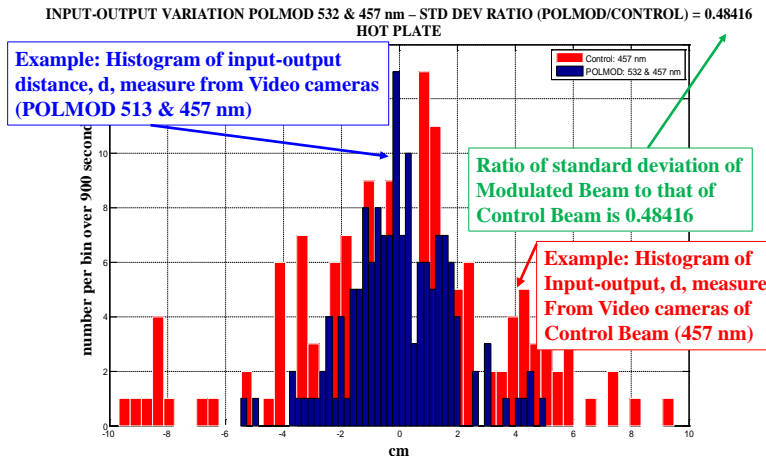


Fig 5.1.6.1 An example of an analysis procedure. The statistical measure is the distance  $d$  of the output beam (camera 1) from the input beam (camera 2), where:

$$d = \sqrt{(x_{\text{centroid\_out}} - x_{\text{centroid\_in}})^2 + (y_{\text{centroid\_out}} - y_{\text{centroid\_in}})^2}.$$

Histogram bin counts were calculated for both control beams (either the 532 nm beam alone, or the  $\xi$  nm beam alone – in red here) and the modulated (the 532 &  $\xi$  nm beam – in blue), where  $\xi = 457, 476, 488$  or  $514$  nm – POLMOD modulation in this case. The result for the modulated beam is overlaid on that for the control beam. The standard deviations were taken from the original data, and the ratio – modulated beam to control beam calculated. In this case it is 0.59126, indicating a decrease in the jitter for the modulated beam. Both beams are of equal entering-medium power. The distance of the beams above the hot plate was 42.0 mm. (Report 33)

INPUT-OUTPUT VARIATION POLMOD 532 & 457 nm – STD DEV RATIO (POLMOD/CONTROL) = 0.48416  
HOTPLATE

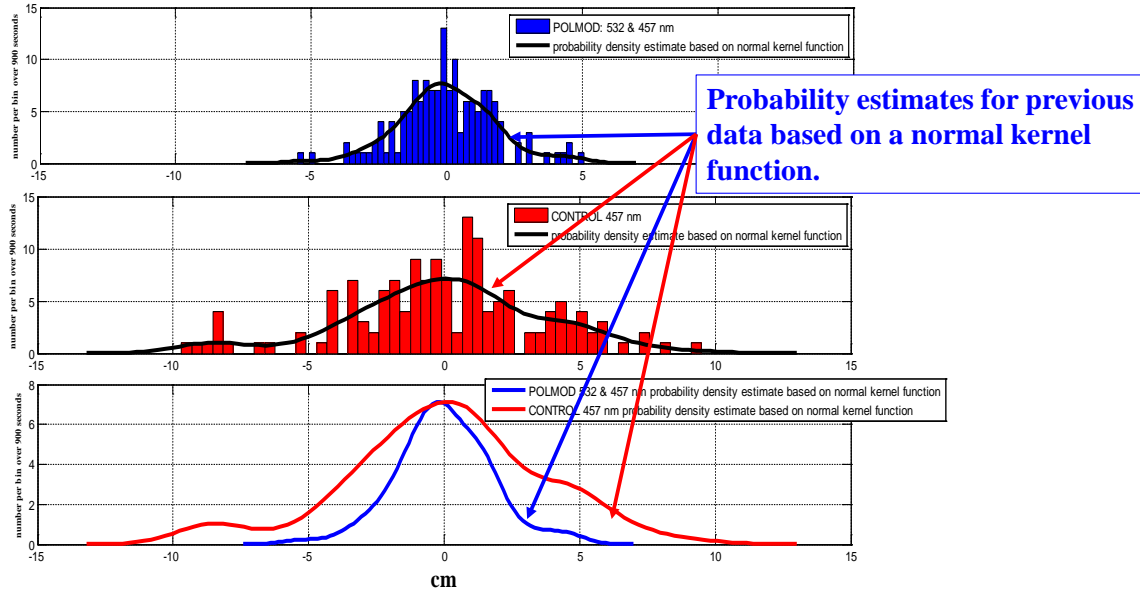


Fig 5.1.6.2 Probability density measures were calculated based on a normal kernel function for the data of Fig 5.1.6.1. An easily visualized comparison of the control and modulated beam can then be made – lower figure.(Report 33)

NOTE: ONLY IN THE CASE OF CD COVER ARE THE MEDIUM DIELECTRICS STATIONARY FOR ALL THREE LASER CONDITIONS RECORDINGS.  
THEREFORE, THE 3 LASER CONDITION RECORDINGS NOT IDENTICAL FOR HOT AIR & VAPOR MEDIA.

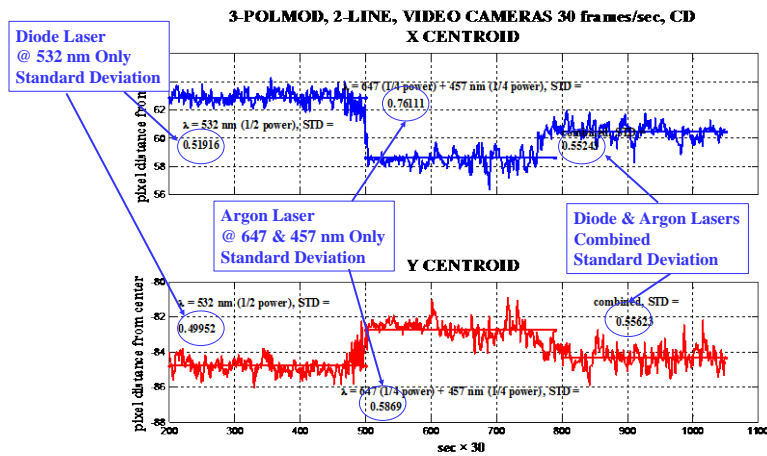


Fig 5.1.7 Video Cameras: Standard deviation data extraction. The  $\sigma$ 's were calculated for the x and y centroids, providing deviations from a central location, the  $\sigma$ 's indicating a measure of jitter. Note again, that only in the case of the CD cover were the dielectrics of the medium stationary. Therefore the results from the CD cover are considered the most reliable.

**NOTE: ONLY IN THE CASE OF CD COVER ARE THE MEDIUM DIELECTRICS STATIONARY  
FOR ALL THREE LASER CONDITIONS RECORDINGS.  
THEREFORE, THE 3 LASER CONDITION RECORDINGS NOT IDENTICAL FOR HOT AIR &  
VAPOR MEDIA.**

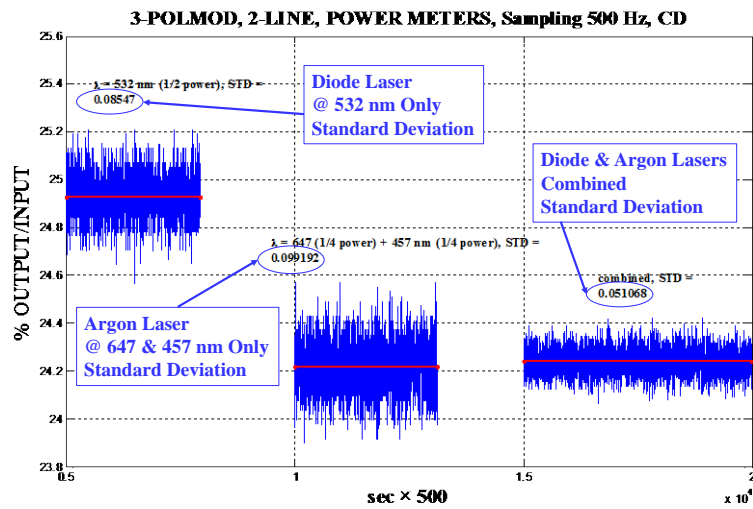


Fig 5.1.8 Power Meters: Standard deviation data extraction. Note again, that only in the case of the CD cover were the dielectrics of the medium stationary. Therefore the results from the CD cover are the most reliable. (Report 38)

$$d = \sqrt{(x_{\text{centroid\_out}} - x_{\text{centroid\_in}})^2 + (y_{\text{centroid\_out}} - y_{\text{centroid\_in}})^2}$$

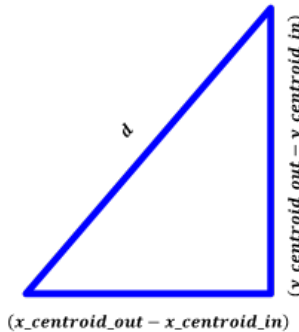


Fig 5.1.9. The means of the x and y centroids for the input and output to the CD medium provided by the 2 CCD cameras permitted the change,  $d$ , effected by the medium to be calculated. (Report 34)

AXMOD – CD –  $\lambda = 647$  nm – BEAM ALIGNMENT CHANGE: % IMPROVEMENT EXPECTANCY: ALIGNMENT CHANGE OFFSET EQUIDISTANT

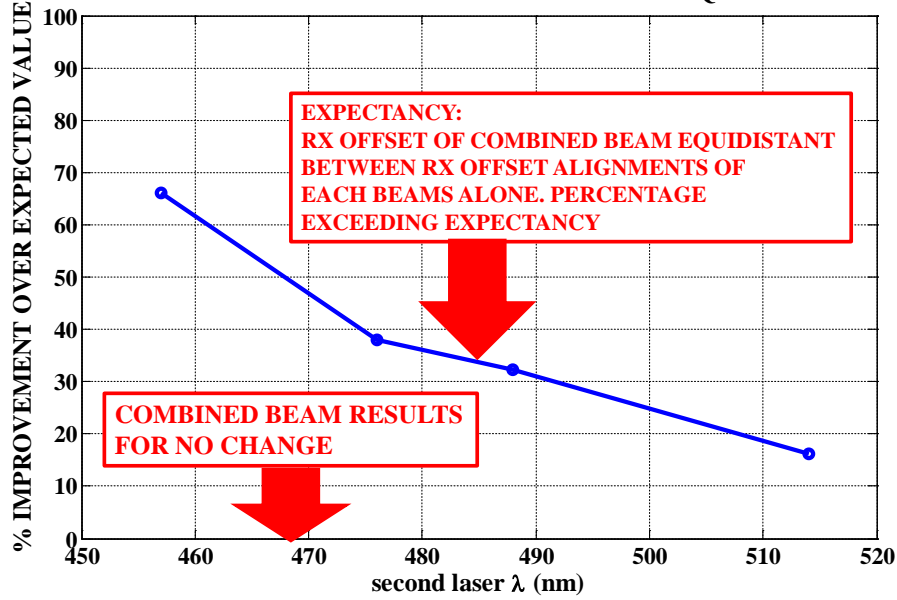


Fig 5.1.10. Data analysis method. Using the  $d$  measures (Fig 5.1.9), a (no effect) expectancy was calculated based on the return signal (RX) offset  $d$  alignment of the combined beam (POLMOD or AXMOD) being equidistant between the RX offset  $d$  alignment of the 2 control beams. This expectancy is the null result condition. A percentage improvement, i.e., percentage deviation from the expectancy, could then be calculated. (Report 34; POWERPOINT: HELSTF JAN 2014. PP: HELSTF\_JANUARY\_1014\_VISIT\_CCD\_CAMERAS)

## 5.2 DATA ANALYSIS

This section provides the evidence of jitter mitigation and the quantitative results under the conditions and test configurations described.

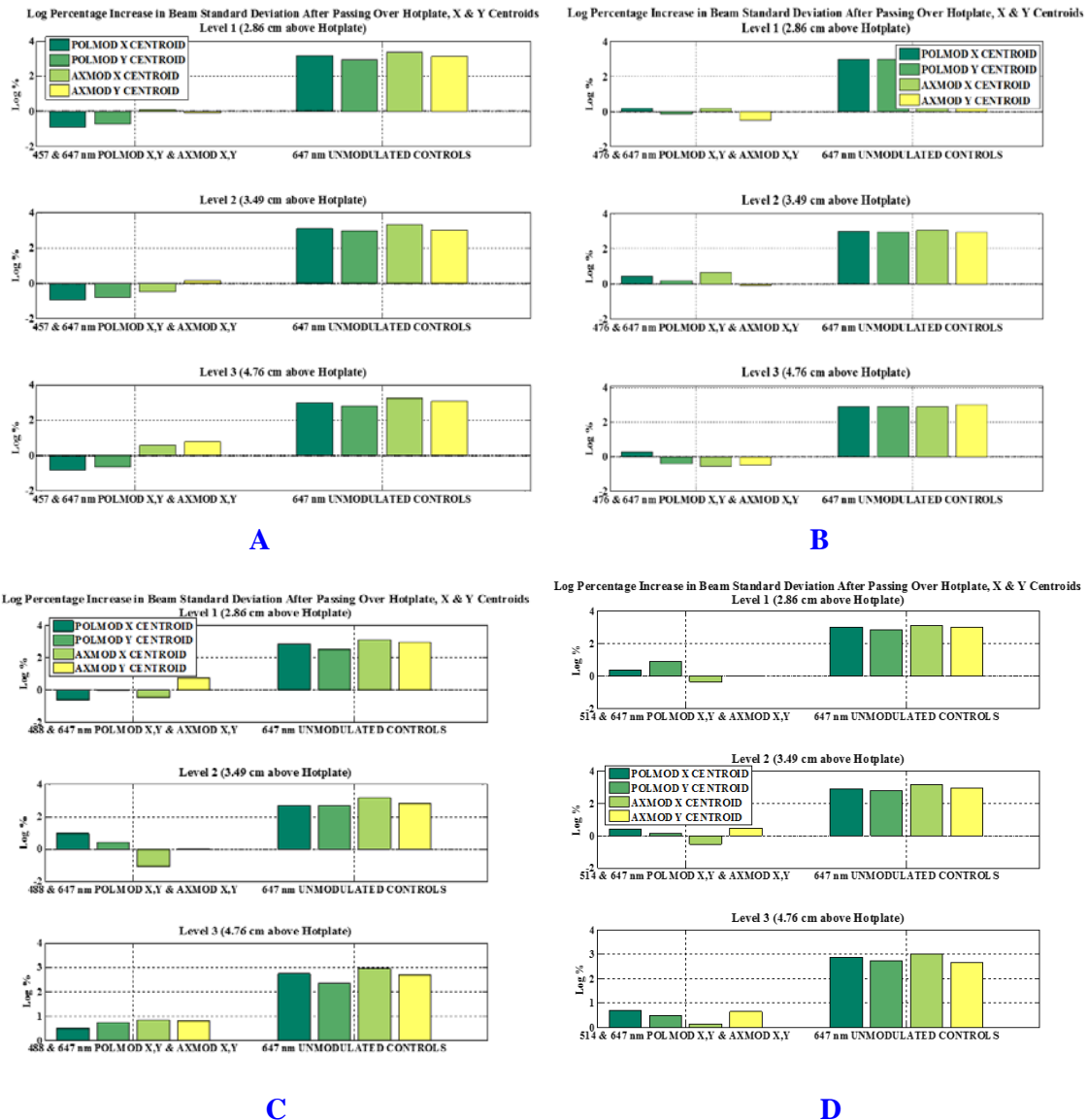


Fig 5.2.1 Heated Air Medium (Hot Plate – Fig 3.2, above). Test beam composed of  $\lambda = 647$  nm beam (Krypton) modulated by a (A)  $\lambda = 457$  nm beam; (B)  $\lambda = 476$  nm; (C)  $\lambda = 488$  nm; (D)  $\lambda = 514$  nm beam, (Argon), for the two modulations: POLMOD and AXMOD. There are two statistical measures: standard deviations of the X centroid and of the Y centroid, giving 4 conditions for the test beam (left) and for the control beam (right). It should be noted that the y-axis is the logarithm of the percentage increase in a beam's standard deviation after passing through the medium (over the hotplate). There is an extremely clear difference between the test and the control results. These results are based on a measure of differences between entering and exiting the medium for all wavelength combinations. (January 2013 tests, Report No 13)

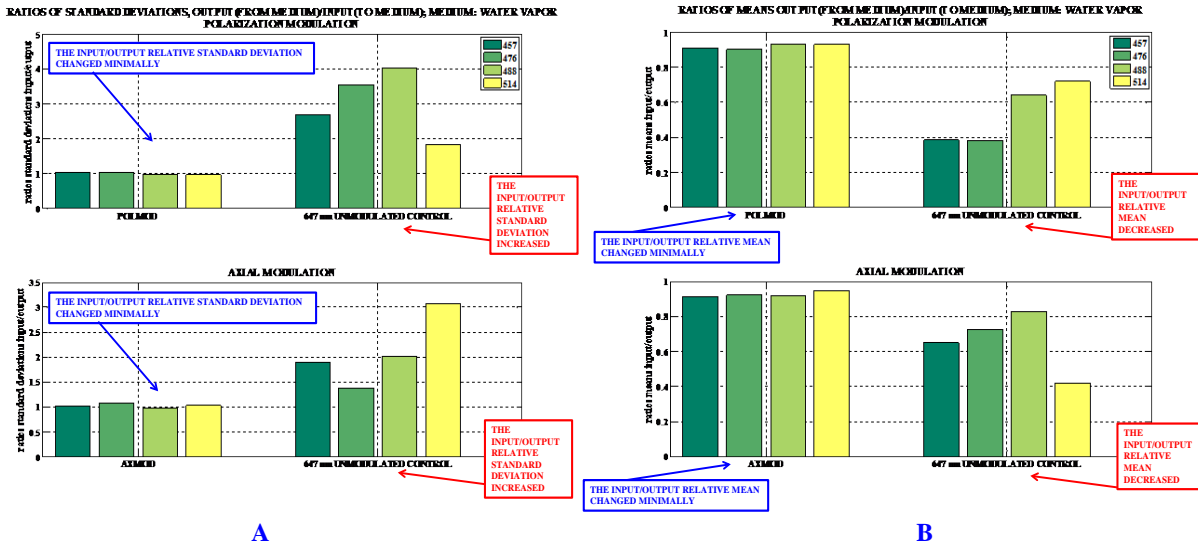


Fig 5.2.2 Water Vapor Medium (see Fig 3.1, above)

A: Ratio of standard deviations (output/input), modulated beams vs control beam. The result is clear-cut and noteworthy. The ratio increases in the case of the control (unmodulated) beam, but remains remarkably constant near 1.0 in the case of the modulated (POLMOD and AXMOD) beams – despite the noisy condition of the modulated beams.

B: Ratio of means (output/input), modulated beams vs control beam. The result is again clear-cut and noteworthy. The ratio decreases in the case of the control (unmodulated) beam, but remains remarkably constant near 0.9 in the case of the modulated (POLMOD and AXMOD) beams – despite the noisy condition of the modulated beams. (Report No 14)

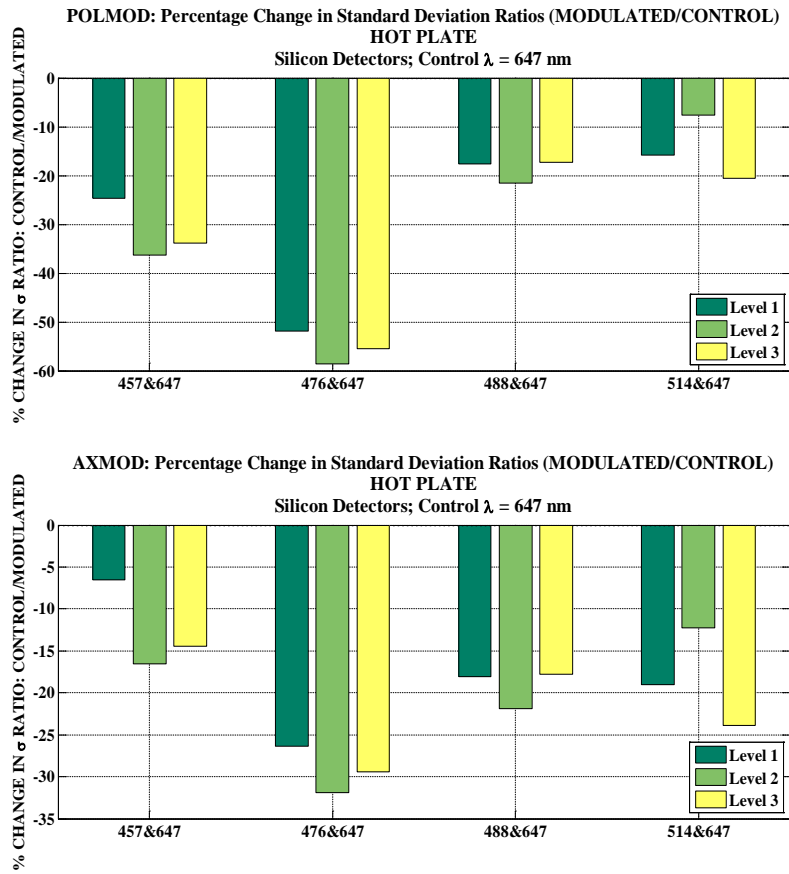


Fig 5.2.3 Heated Air Medium (Hot Plate – see Fig 3.2, above). Percentage change in standard deviation ratios (modulated/control), where modulation is either POLMOD or AXMOD, at three levels of beam passage over the hot plate, and with four modulating wavelengths  $\lambda = 457, 476, 488$  and  $514$  nm with carrier  $\lambda = 647$  nm. Control beam wavelength  $\lambda = 647$  nm and the modulation and control beams were of equal amplitude. The expectancy was that any change due to a modulation would be in the negative direction, i.e., less jitter from passing through the medium defeating changing refraction (the real part of the medium dielectric constant). The expected result was obtained in all cases. (Report 19)

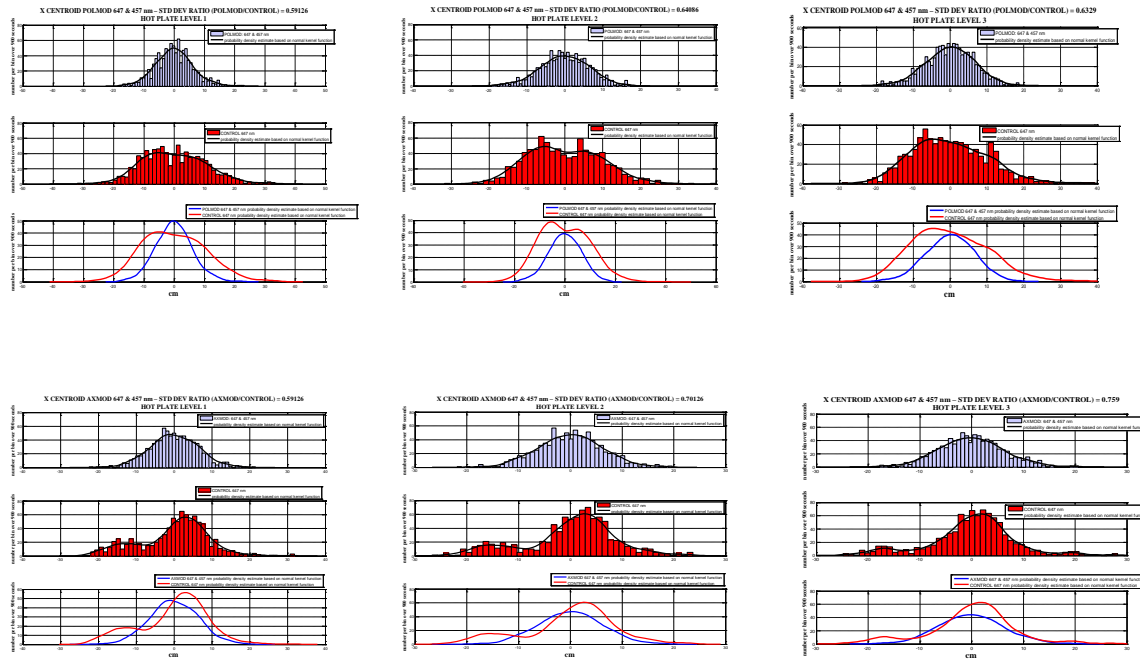


Fig 5.2.4.1 Medium: Heated Air (Hot Plate, see Fig 3.2, above). Upper: POLMOD. Lower: AXMOD. X Centroid: 647 & 457 nm (modulated) – blue – and 647 nm (control) – red – beams. Columns: Levels 1, 2 and 3. (Report 17)

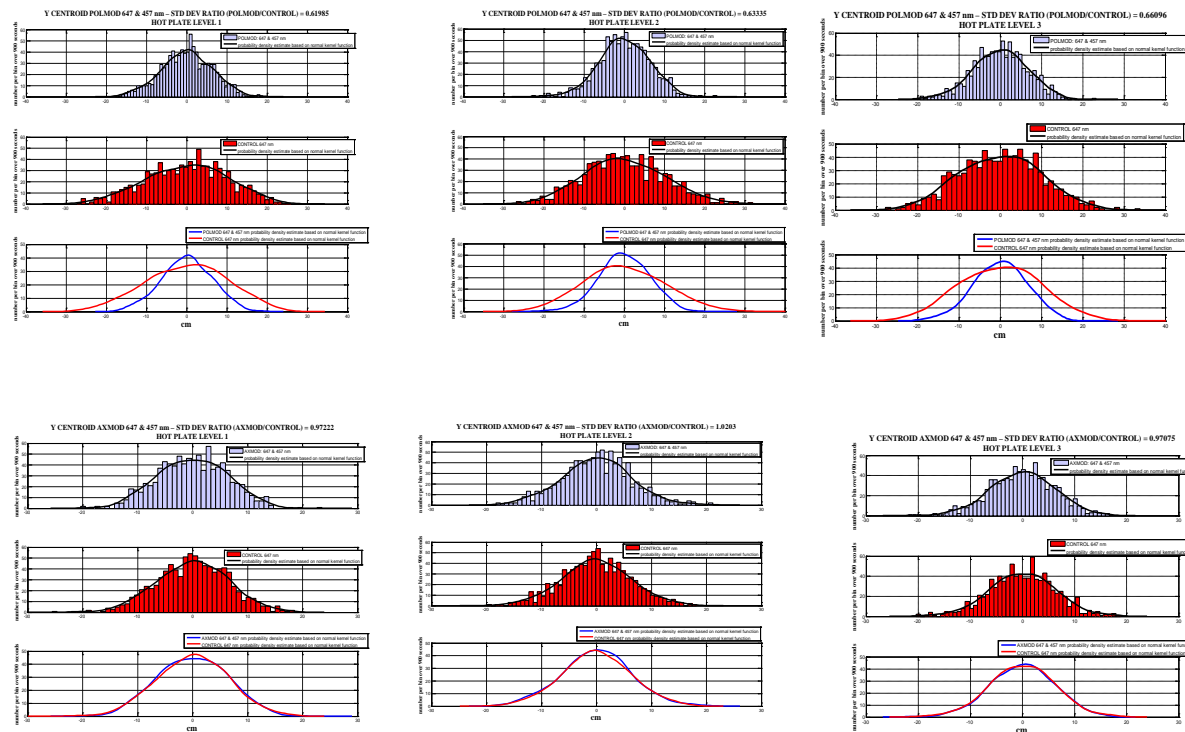


Fig 5.2.4.2 Medium: Heated Air (Hot Plate, see Fig 3.2, above). Upper: POLMOD. Lower: AXMOD. Y Centroid: 647 & 457 nm (modulated) – blue – and 647 nm (control) – red – beams. Columns: Levels 1, 2 and 3. The same data are represented in A and B. (Report 17)

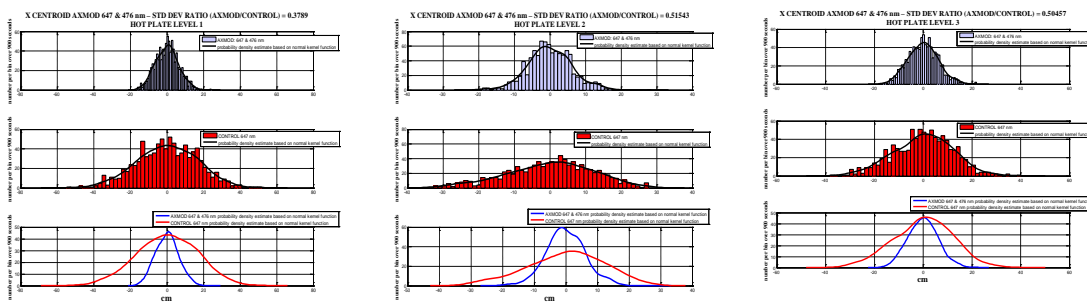
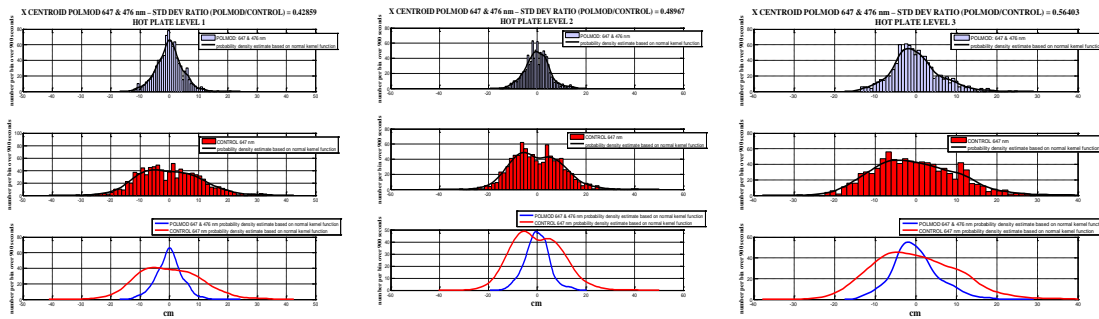


Fig 5.2.4.3 Medium: Heated Air (Hot Plate, see Fig 3.2, above). Upper: POLMOD. Lower: AXMOD. X Centroid: 647 & 476 nm (modulated) – blue – and 647 nm (control) – red – beams. Columns: Levels 1, 2 and 3. The same data are represented in A and B. (Report 17)

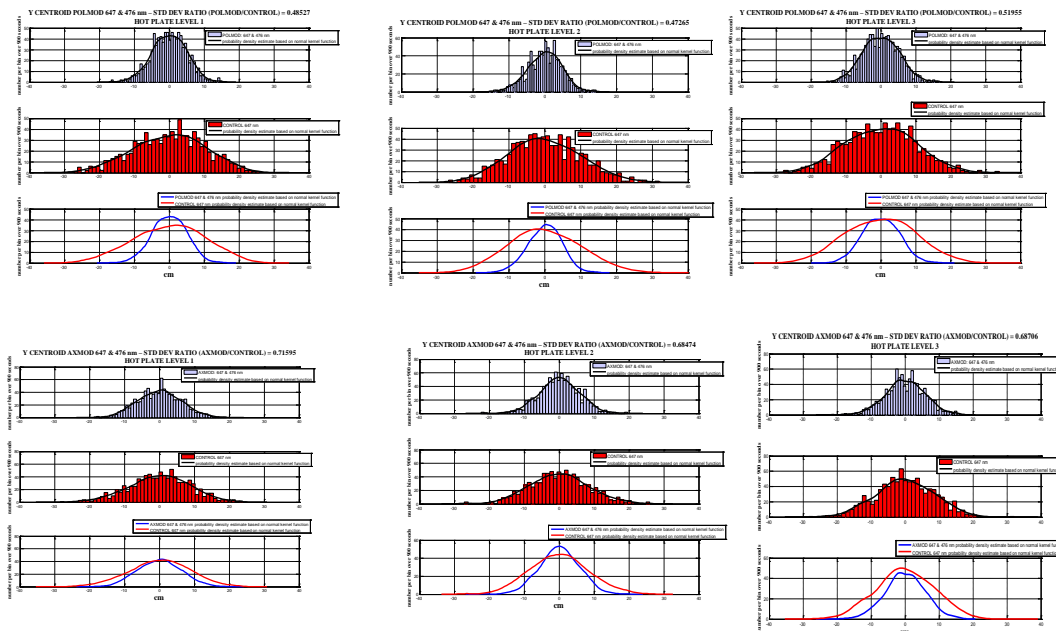
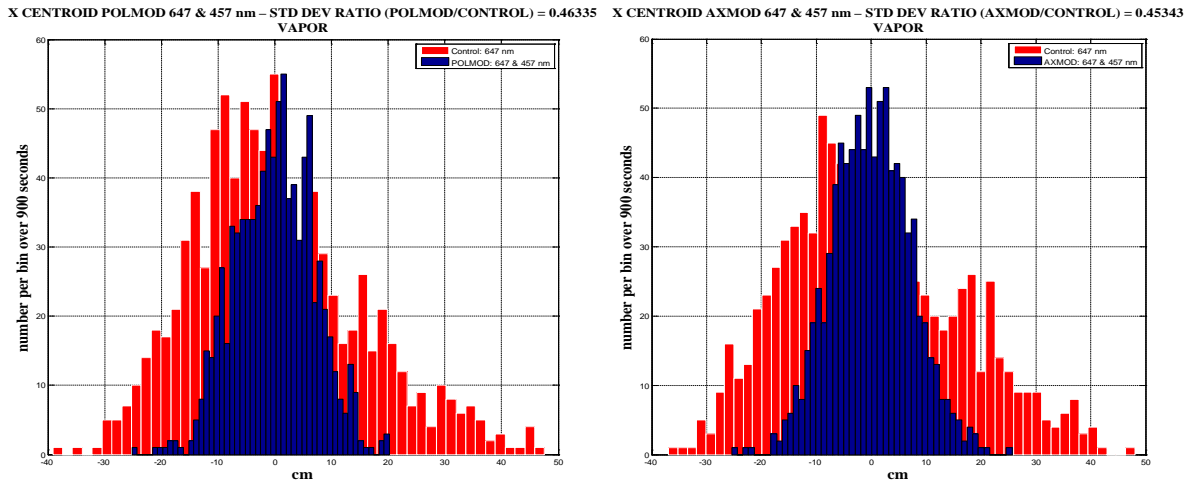
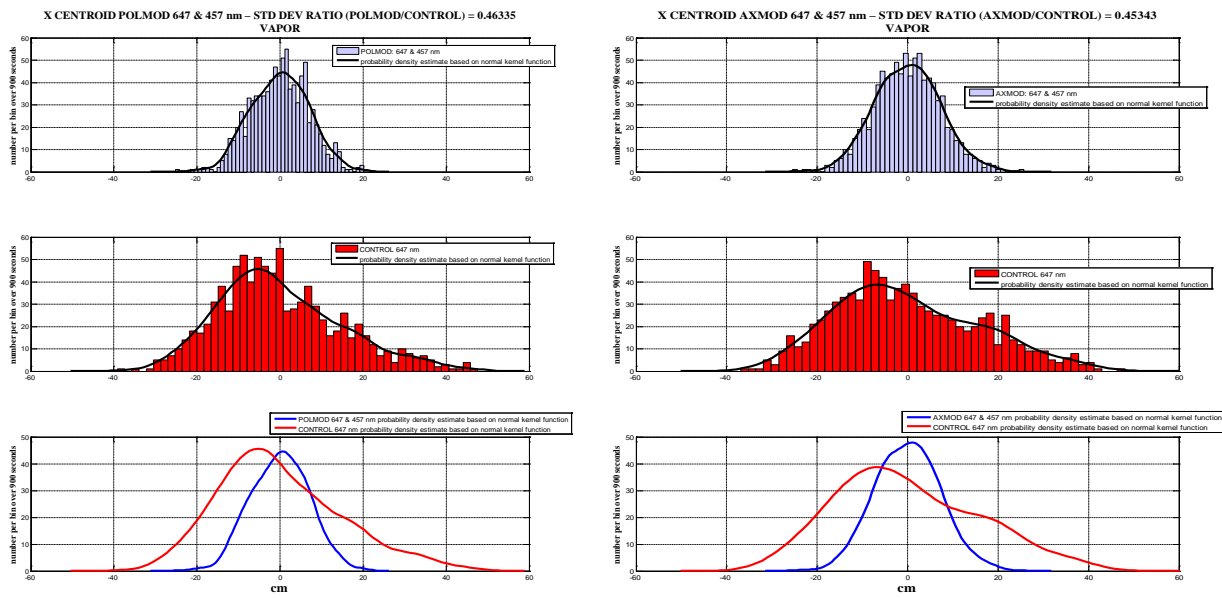


Fig 5.2.4.4 Medium: Heated Air (Hot Plate, see Fig 3.2, above). Upper: POLMOD. Lower: AXMOD. Y Centroid: 647 & 476 nm (modulated) – blue – and 647 nm (control) – red – beams. Columns: Levels 1, 2 and 3. The same data are represented in A and B. (Report 17)



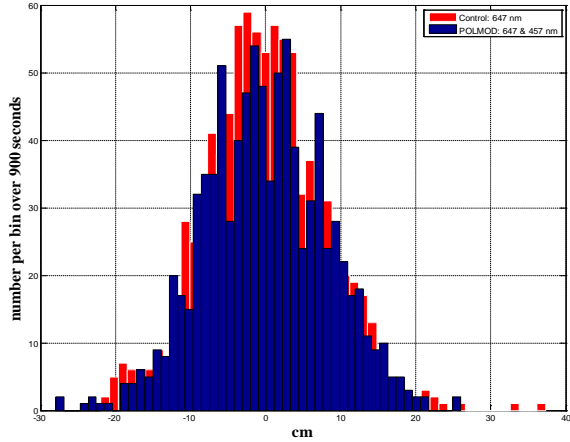
A



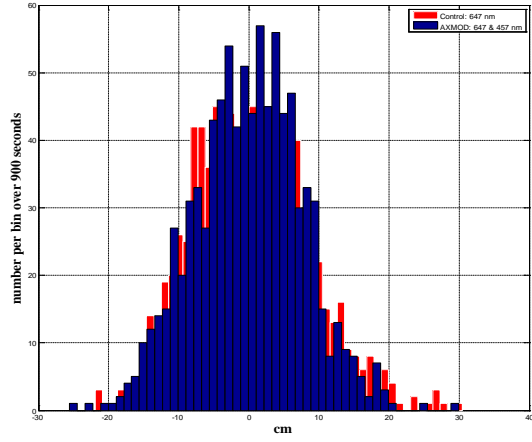
B

Fig 5.2.5.1 Medium: Water Vapor (see Fig 3.1, above). X Centroid: 647 & 457 nm (modulated) – blue – and 647 nm (control) – red – beams. Columns: POLMOD & AXMOD. The same data are represented in A and B. (Report 18)

Y CENTROID POLMOD 647 & 457 nm – STD DEV RATIO (POLMOD/CONTROL) = 1.0236  
VAPOR

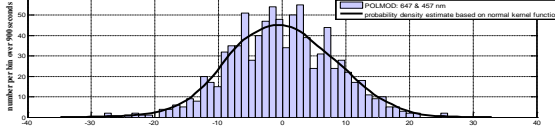


Y CENTROID AXMOD 647 & 457 nm – STD DEV RATIO (AXMOD/CONTROL) = 0.91049  
VAPOR

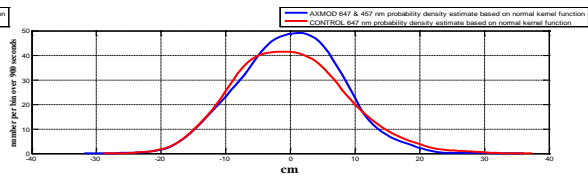
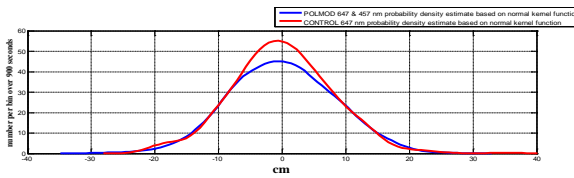
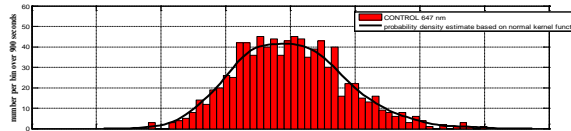
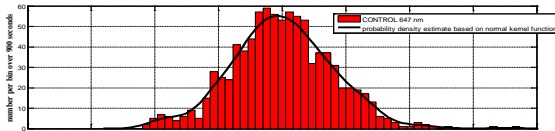
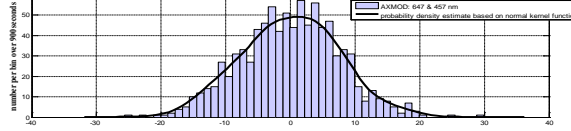


A

Y CENTROID POLMOD 647 & 457 nm – STD DEV RATIO (POLMOD/CONTROL) = 1.0236  
VAPOR

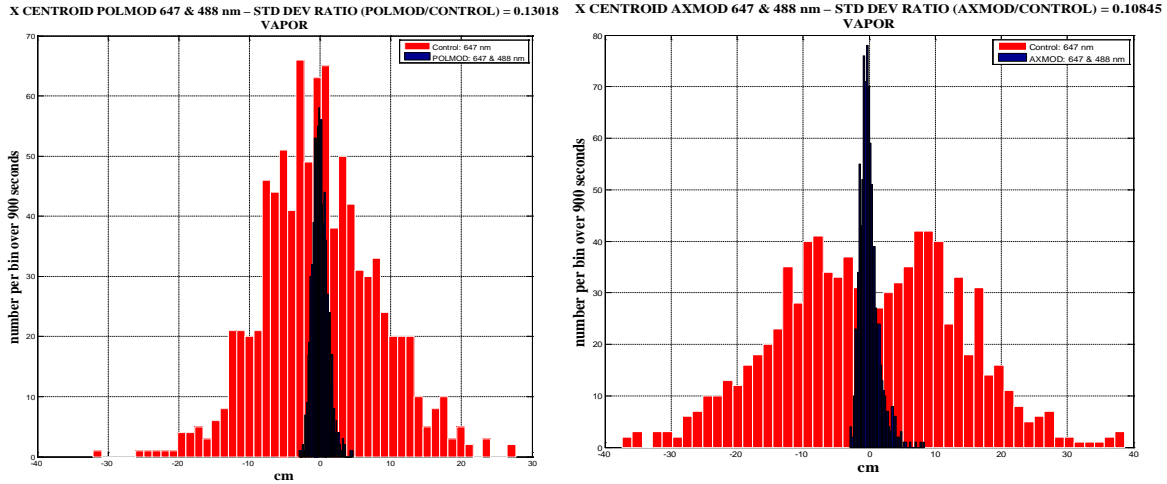


Y CENTROID AXMOD 647 & 457 nm – STD DEV RATIO (AXMOD/CONTROL) = 0.91049  
VAPOR

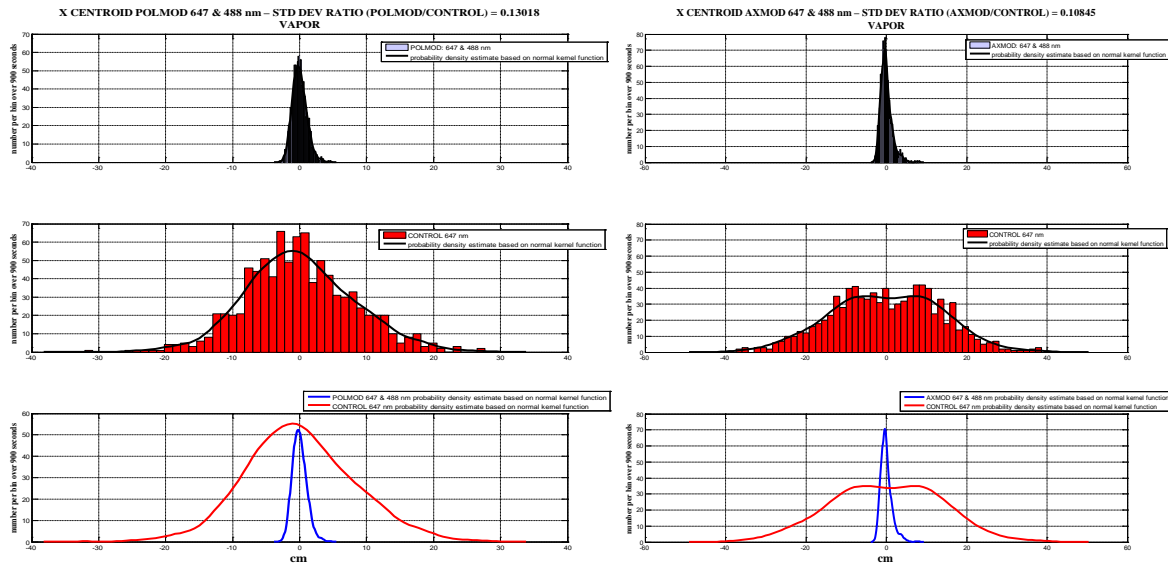


B

Fig 5.2.5.2 Medium: Water Vapor (see Fig 3.1, above). Y Centroid: 647 & 457 nm (modulated) – blue – and 647 nm (control) – red – beams. Columns: POLMOD & AXMOD. The same data are represented in A and B. (Report 18)

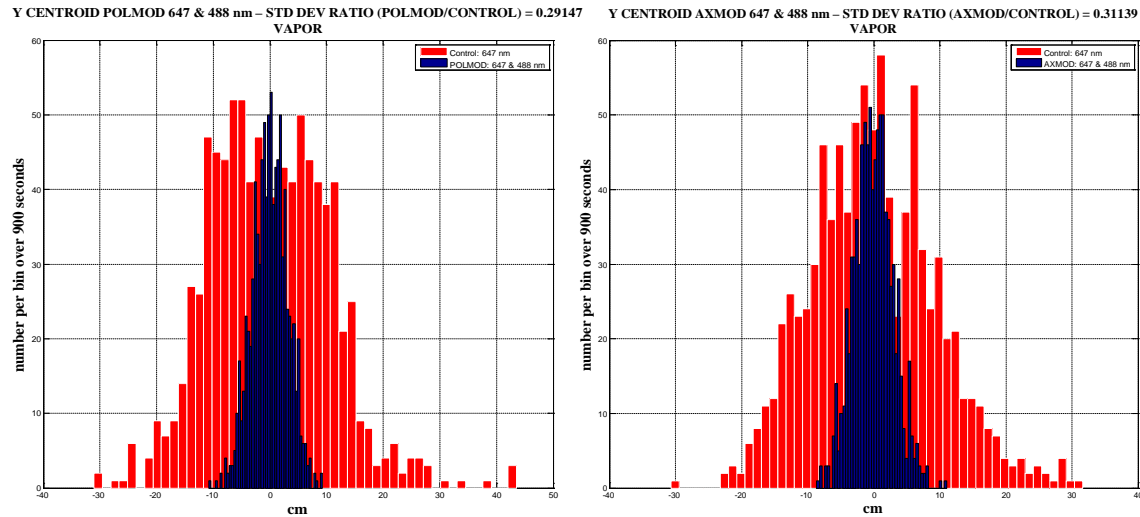


A

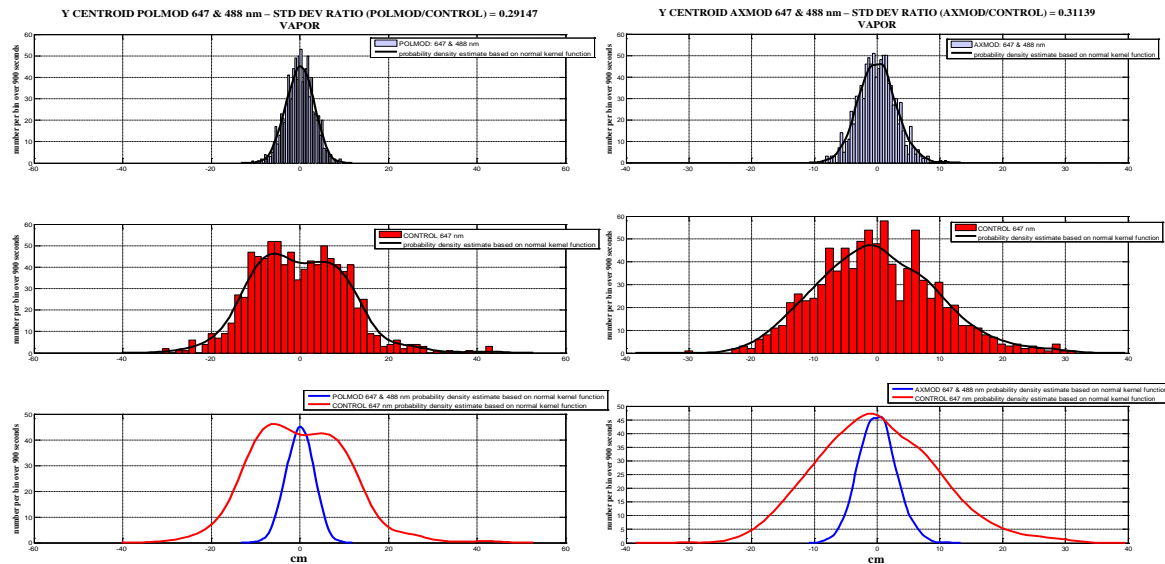


B

Fig 5.2.6.1 Medium: Water Vapor (see Fig 3.1, above). X Centroid: 647 & 488 nm (modulated) – blue – and 647 nm (control) – red – beams. Columns: POLMOD & AXMOD. The same data are represented in A and B. (Report 18)



A



B

Fig 5.2.6.2 Medium: Water Vapor (see Fig 3.1, above). Y Centroid: 647 & 488 nm (modulated) – blue – and 647 nm (control) – red – beams. Columns: POLMOD & AXMOD. The same data are represented in A and B. (Report 18)

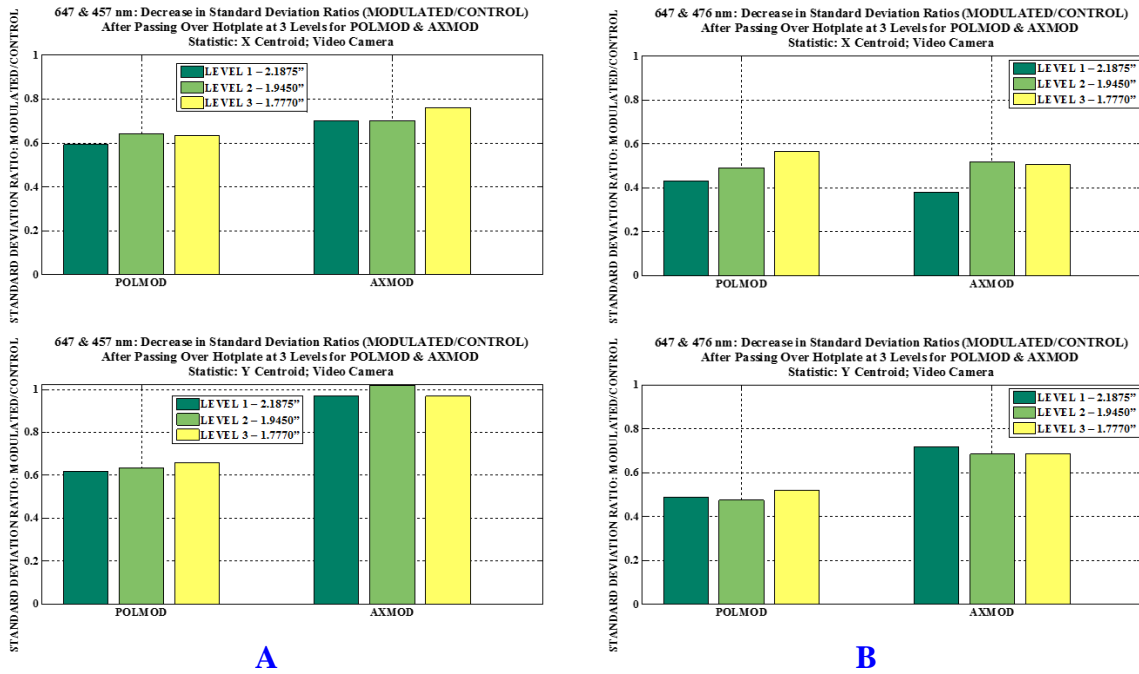


Fig 5.2.7 Medium: Heated Air (see Fig 3.2, above). Standard deviation ratios: modulated beam/control beam. Upper: X centroid values; Lower: Y centroid values.

(A): Except for AXMOD, Y Centroid, Level 2, all ratios are less than 1.0, which, if the input modulated and control beams were equal in jitter, indicate a reduction in jitter increase resulting from passage through the medium, by the modulated condition.

(B) All ratios are less than 1.0, which, if the input modulated and control beams were equal in jitter, indicate a reduction in jitter increase resulting from passage through the medium, by the modulated condition. (Report 17)

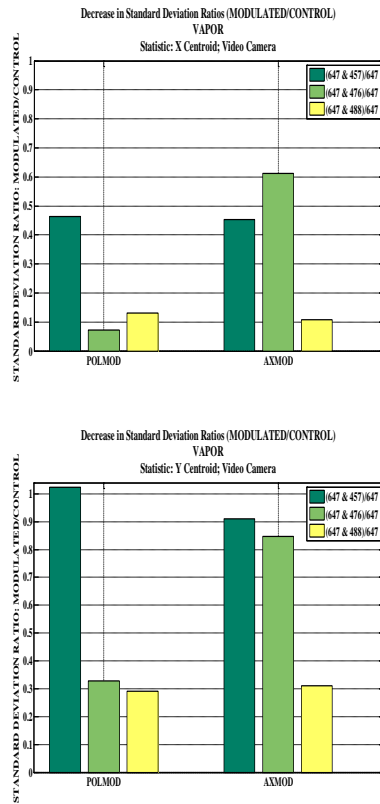


Fig 5.2.8 Medium: Water Vapor (see Fig 3.1, above). Standard deviation ratios: modulated beam/control beam. Upper: X centroid values; Lower: Y centroid values. Except for the AXMOD, Y Centroid, (647 & 457)/647 result (lower, right), all ratios are less than 1.0, which, if the input modulated and control beams were equal in jitter as assumed, indicate a substantial reduction by the modulated conditions of normal jitter-increase resulting from passage through the medium. (Report 18)

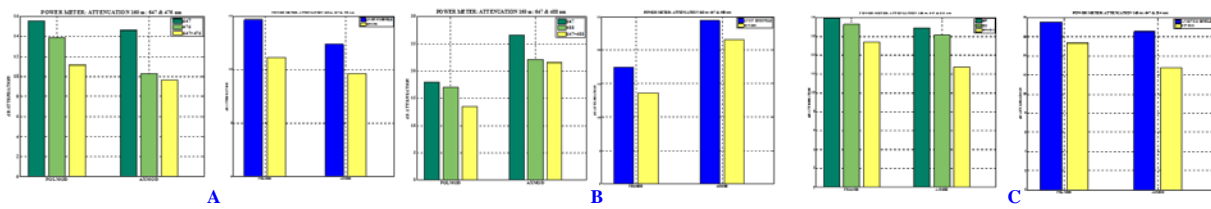


Fig 5.2.9 Medium: Power meter tests conducted for propagation over 160 meters of desert (see Figs 4.2.1 & 4.2.2, above). POLMOD and AXMOD power meter results for  
 (A) LEFT:  $\lambda = 647$  nm alone, 476 nm alone & 647 + 476 nm combined. RIGHT: the  $\lambda = 647$  nm alone and  $\lambda = 476$  nm alone results have been averaged.  
 (B) LEFT:  $\lambda = 647$  nm alone, 488 nm alone & 647 + 488 nm combined. RIGHT: the  $\lambda = 647$  nm alone and  $\lambda = 476$  nm alone results have been averaged.  
 (C) LEFT:  $\lambda = 647$  nm alone, 514 nm alone & 647 + 514 nm combined. RIGHT: the  $\lambda = 647$  nm alone and  $\lambda = 476$  nm alone results have been averaged.

There is less attenuation in the case of the modulated beams. (Report 26)

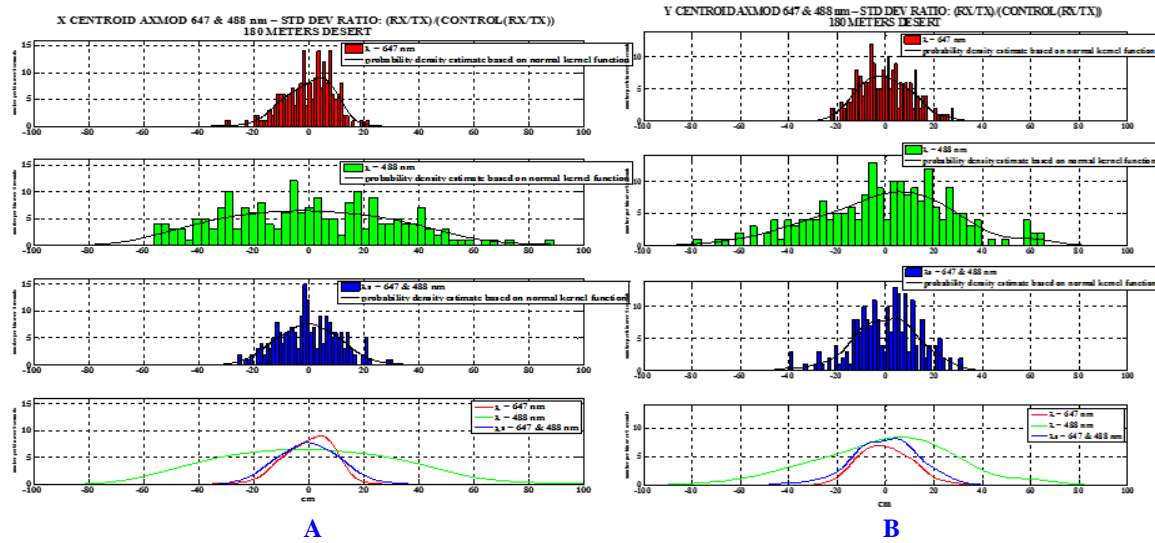
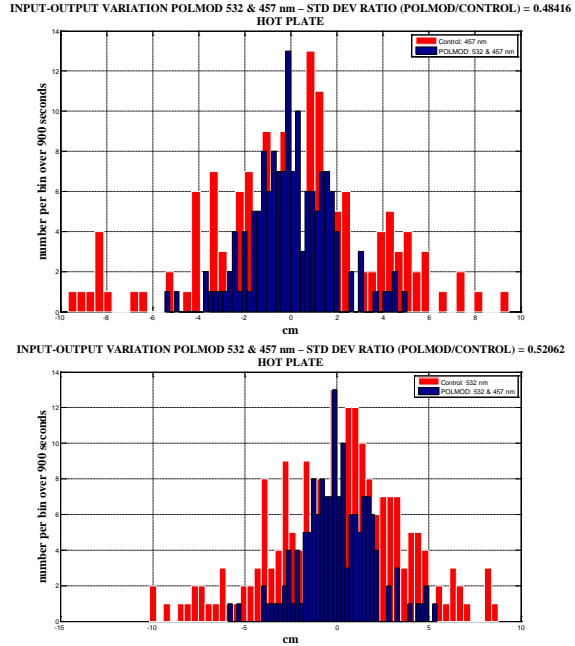
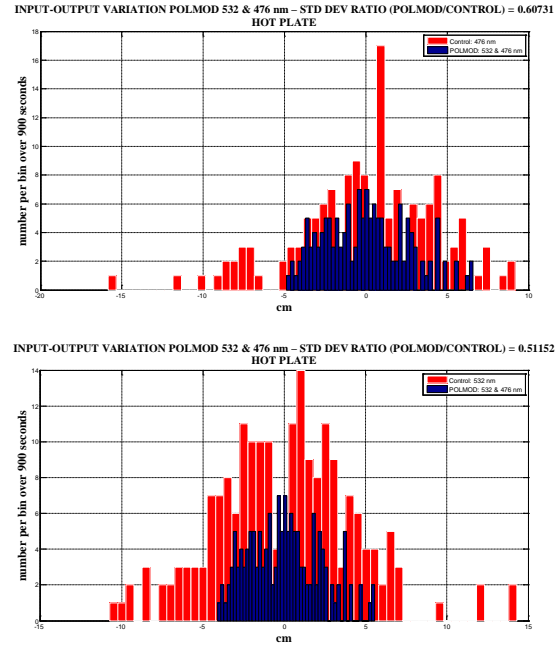


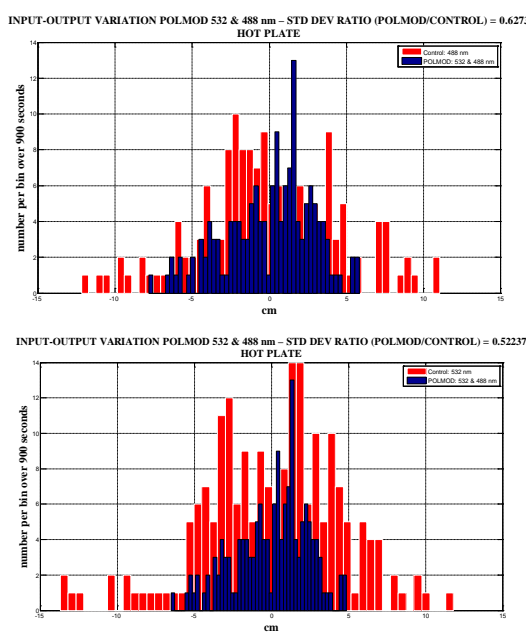
Fig 5.2.10 Medium: Power meter tests conducted for propagation over 160 meters of desert (see Figs 4.2.1 & 4.2.2, above). AXMOD X and Y Centroid histograms for the three cases: (a) Krypton beam alone ( $\lambda = 647$  nm); (b) Argon beam alone ( $\lambda = 488$  nm); and (c) modulated beam. Beam with maximum jitter is the 488 beam. (Report 27)



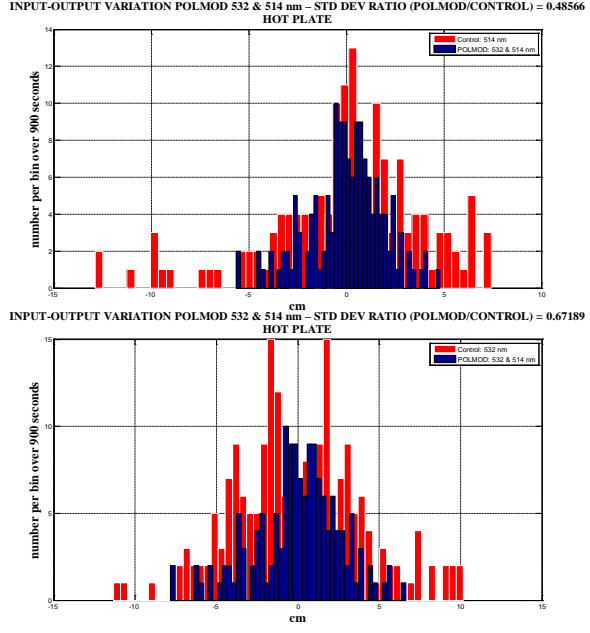
A



B

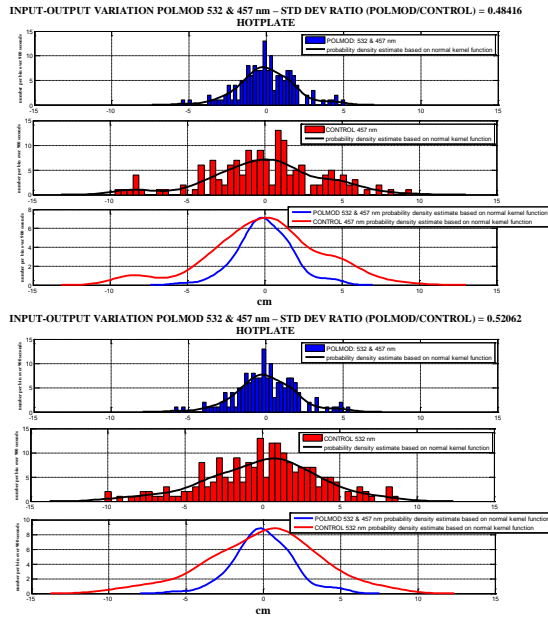


C

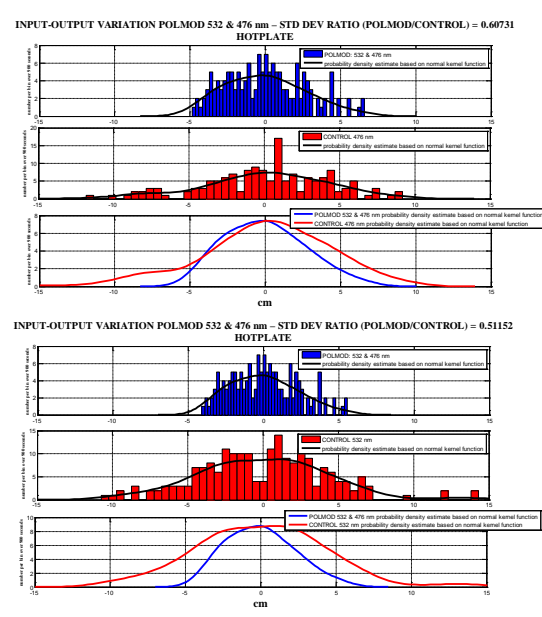


D

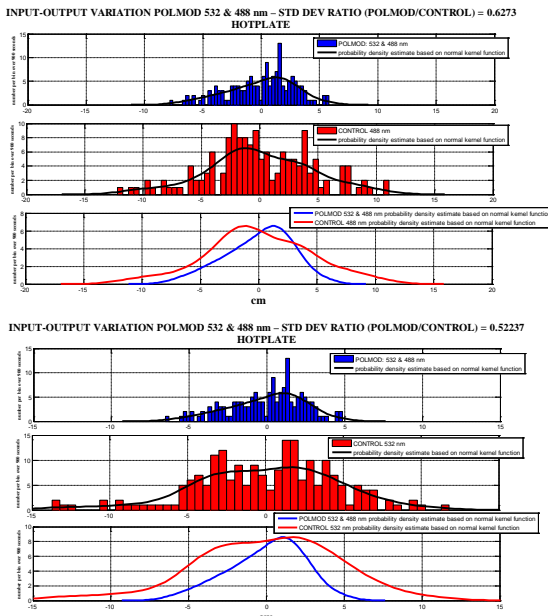
Fig 5.2.11.1 Medium: heated Air (Hot Plate, see Fig 3.2 above). POLMOD Input-Output variation  $d$  value histograms: 532 &  $\xi$  nm (modulated) – blue – where  $\xi = 457$  (A), 476 (B), 488 (C) and 514 (D) nm. In A-C, in the case of the upper figure, the comparison control beam – red – is  $\lambda = \xi$ , ( $\xi = 457$  (A), 476 (B), 488 (C) and 514 (D)); and in the case of the bottom figure, the comparison control beam – red – is  $\lambda = 514$  nm. (Report 33)



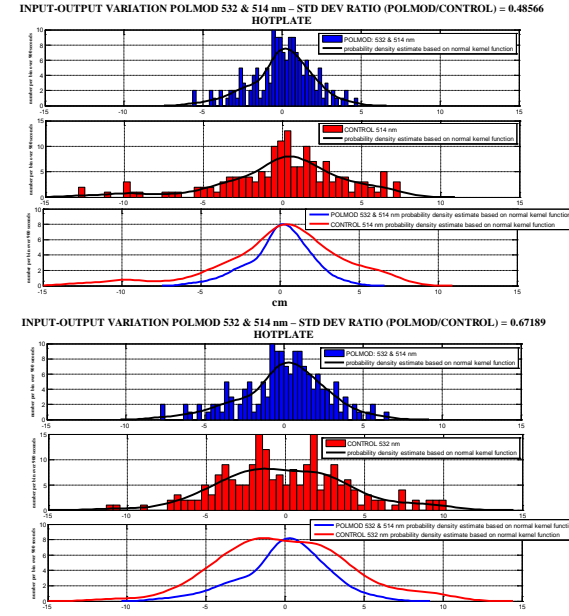
**A**



**B**

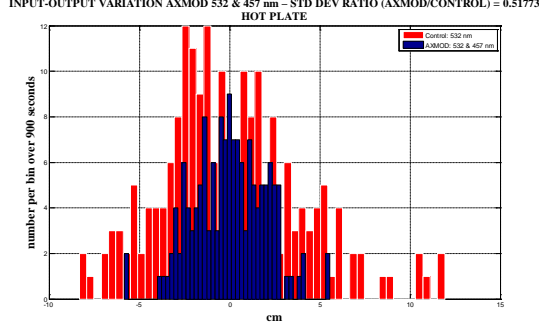
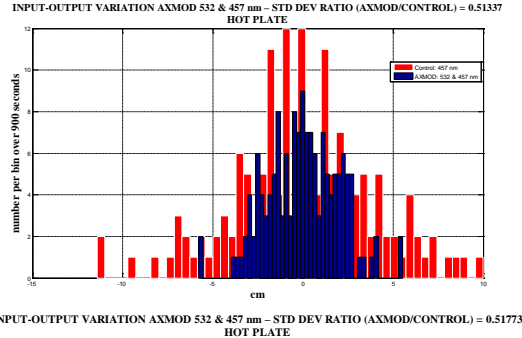


**C**

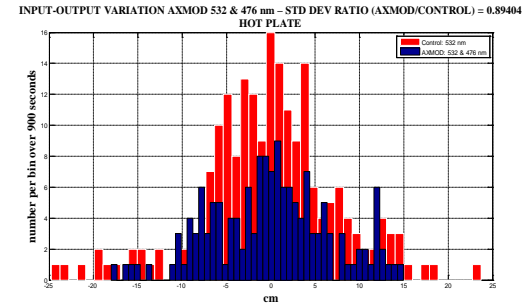
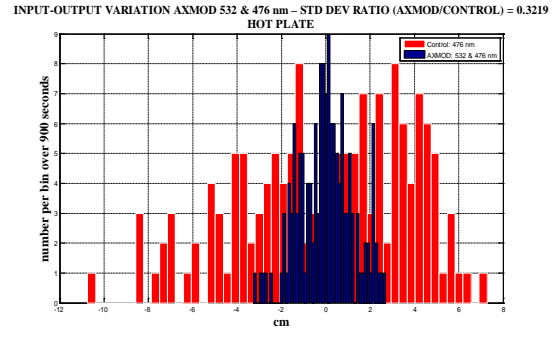


**D**

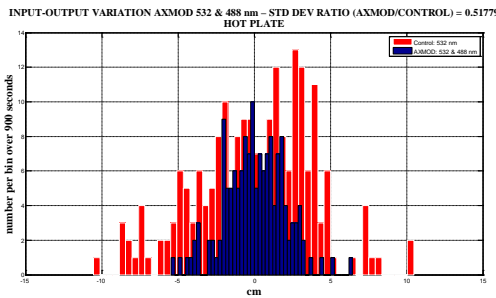
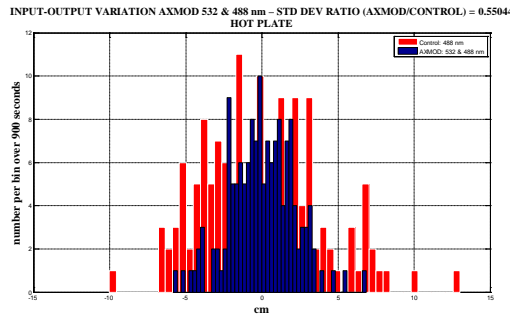
Fig 5.2.11.2 Medium: heated Air (Hot Plate, see Fig 3.2 above). POLMOD Input-Output variation  $d$  value histograms: 532 &  $\xi$  nm (modulated) – blue – where = 457 (A), 476 (B), 488 (C) and 514 (D) nm. Probability density measures calculated for the data shown in Fig 8A based on a normal kernel function. An easily visualized comparison of the control and modulated beam can then be made – lower figure. (Report 33)



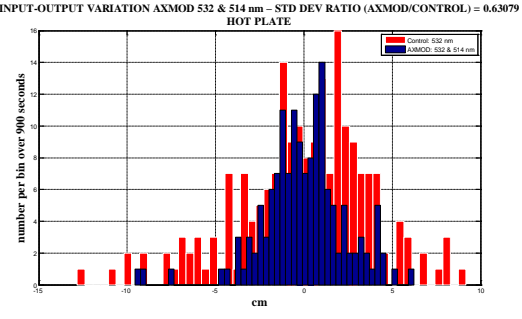
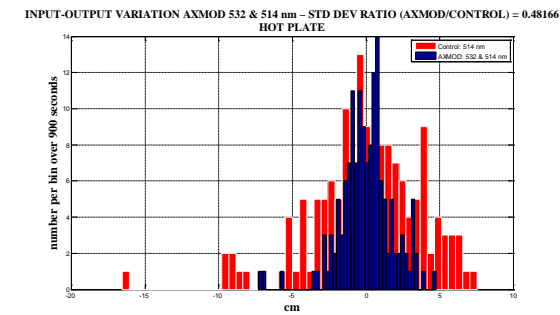
A



B



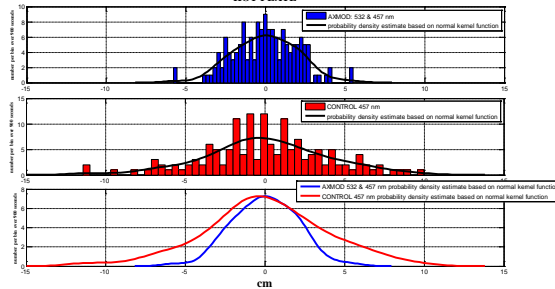
C



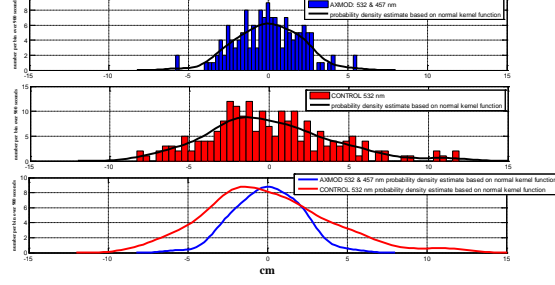
D

Fig 5.2.12.1 Medium: heated Air (Hot Plate, see Fig 3.2 above). AXMOD Input-Output variation  $d$  value histograms: 532 &  $\xi$  nm (modulated) – blue – where  $\xi = 457$  (A), 476 (B), 488 (C) and 514 (D) nm. In A-C, in the case of the upper figure, the comparison control beam – red – is  $\lambda = \xi$ , ( $\xi = 457$  (A), 476 (B), 488 (C) and 514 (D)); and in the case of the bottom figure, the comparison control beam – red – is  $\lambda = 514$  nm. (Report 33)

INPUT-OUTPUT VARIATION AXMOD 532 & 457 nm – STD DEV RATIO (AXMOD/CONTROL) = 0.51337 HOT PLATE

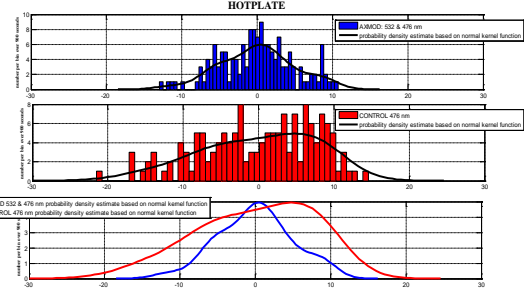


INPUT-OUTPUT VARIATION AXMOD 532 & 457 nm – STD DEV RATIO (AXMOD/CONTROL) = 0.51773 HOTPLATE

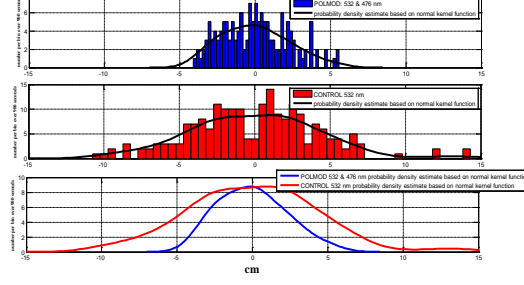


**A**

INPUT-OUTPUT VARIATION AXMOD 532 & 476 nm – STD DEV RATIO (AXMOD/CONTROL) = 0.6438 HOTPLATE

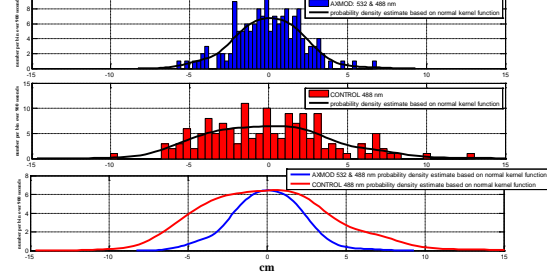


INPUT-OUTPUT VARIATION POLMOD 532 & 476 nm – STD DEV RATIO (POLMOD/CONTROL) = 0.51152 HOTPLATE

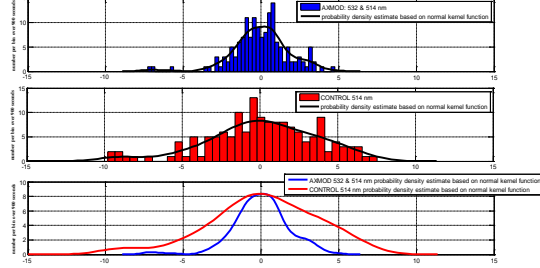


**B**

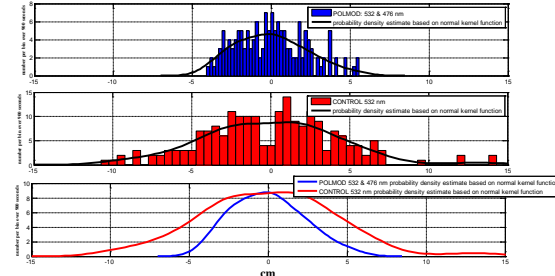
INPUT-OUTPUT VARIATION AXMOD 532 & 488 nm – STD DEV RATIO (AXMOD/CONTROL) = 0.55044 HOTPLATE



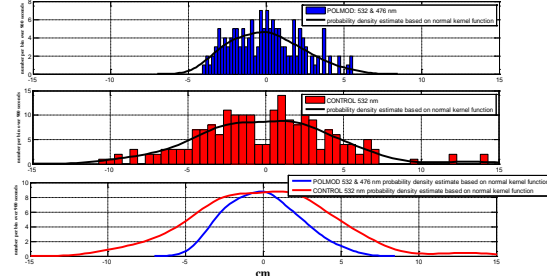
INPUT-OUTPUT VARIATION AXMOD 532 & 514 nm – STD DEV RATIO (AXMOD/CONTROL) = 0.48166 HOTPLATE



INPUT-OUTPUT VARIATION POLMOD 532 & 476 nm – STD DEV RATIO (POLMOD/CONTROL) = 0.51152 HOTPLATE



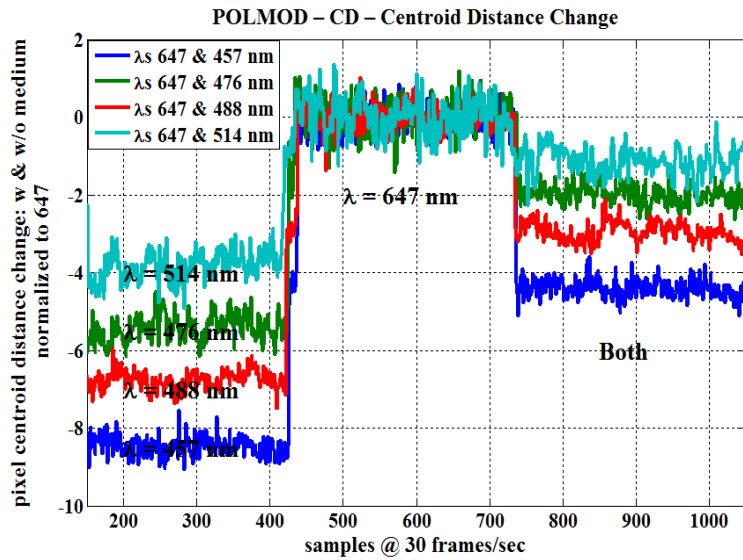
INPUT-OUTPUT VARIATION POLMOD 532 & 476 nm – STD DEV RATIO (POLMOD/CONTROL) = 0.51152 HOTPLATE



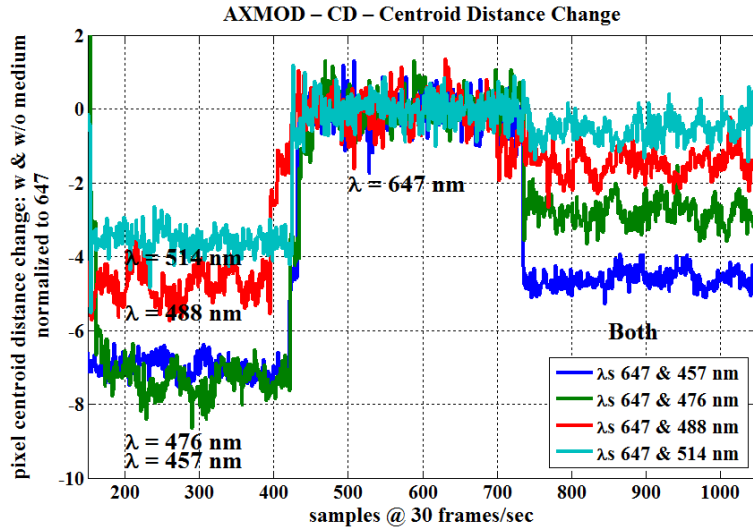
**C**

**D**

Fig 5.2.12.2 Medium: heated Air (Hot Plate, see Fig 3.2 above). AXMOD Input-Output variation  $d$  value histograms: 532 &  $\xi$  nm (modulated) – blue – where = 457 (A), 476 (B), 488 (C) and 514 (D) nm. Probability density measures calculated for the data shown in Fig 9A based on a normal kernel function. An easily visualized comparison of the control and modulated beam can then be made – lower figure. (Report 33)

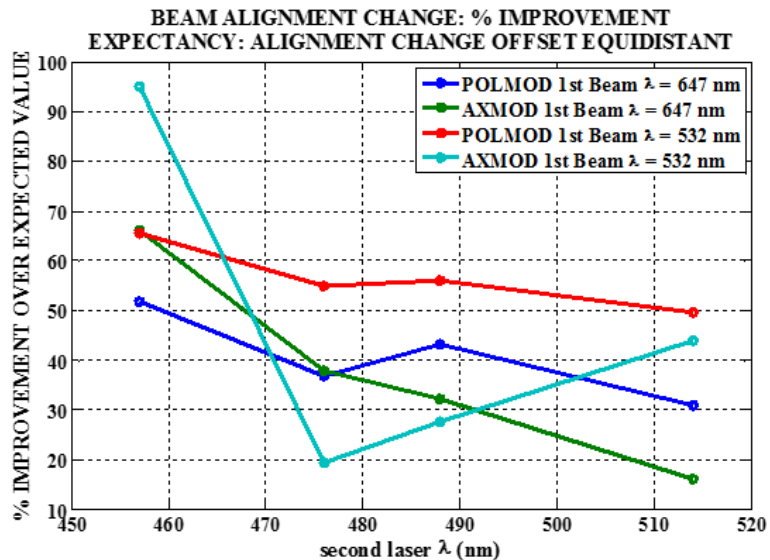


A

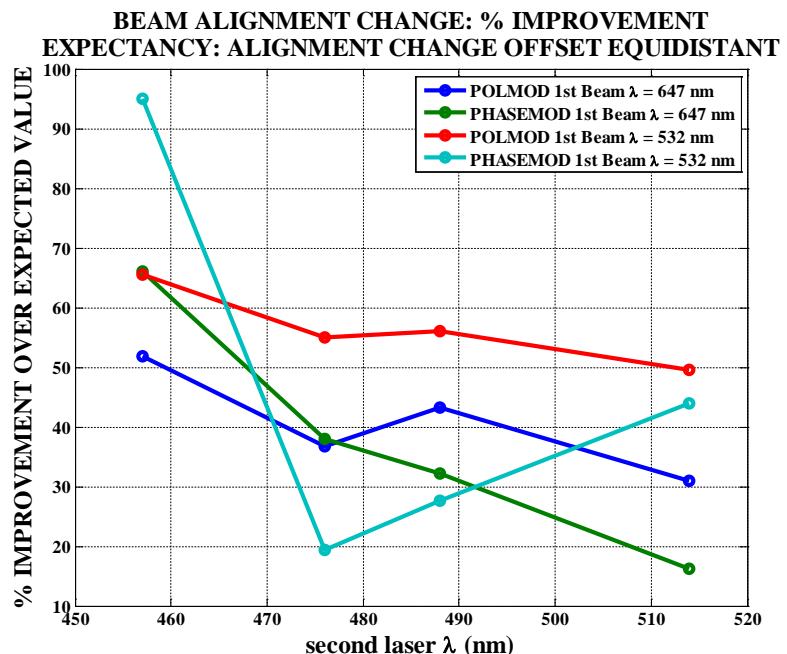


B

Fig 5.2.13 Medium: Phase Plate: CD case.  $d$  measures (see Fig 5.1.9, above), stationary refractive index tests (I) – see test procedure Fig 4.14, above, and analysis procedure 5.1.7 above). The results for the propagations through the CD medium of (i) first the single  $\lambda_2$  control Argon beam ( $\lambda_2 = 457, 476, 488$  or  $514$  nm), then (ii) the single  $\lambda_1$  beam (647 nm) control beam, and finally, (iii) the  $\lambda_1 + \lambda_2$  test beam. A: the POLMOD condition; B: the AXMOD condition. (Report 34; POWERPOINT: HELST JAN 2014)



A



B

Fig 5.2.14 Medium: Phase Plate: CD case. The resulting percentage  $d$  deviations from expectancy measures for conditions (I)  $\lambda_1 = 647$  nm and (II)  $\lambda_1 = 432$  nm, under the (A) POLMOD and (B) PhaseMod conditions, and for modulating frequencies,  $\lambda_2 = 457, 476, 488$  or  $514$  nm. A trend can be seen that indicates the highest improvement in refractive index-induced deviation in beam alignment occurs when  $(\lambda_1 - \lambda_2)$  is greatest. (Report 34. PP: HELSTF\_JANUARY\_1014\_VISIT\_CCD\_CAMERAS)

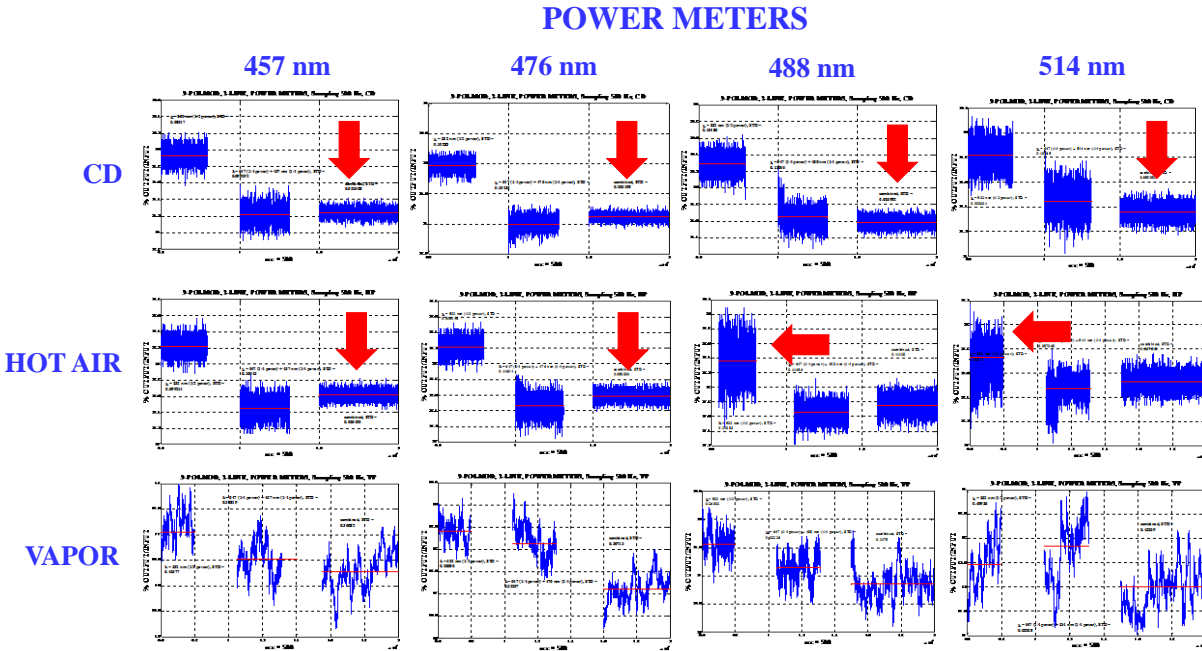


Fig 5.2.15 Media: Phase Plate, CD case, Heated Air, Water Vapor. Power meters: In the case of the CD cover medium – the most reliable condition – there is a clear reduction in the  $\sigma$ 's across Ar  $\lambda$ 's = 457, 476, 488 & 514 nm. The reduction is even evident for the hot air medium for Ar  $\lambda$ 's = 457 and 476 nm. Interestingly, the  $\sigma$ 's for diode = 532 nm at Ar  $\lambda$ 's = 488 and 514 nm are increased in comparison with the Kr + Ar and combined conditions. Noteworthy are the amplitudes of the combined condition. This tableau clearly indicates the non-stationarity of the vapor condition in comparison even with the hot air. One might expect that as the Power of Diode beam = Power Ar beam + Power Kr beam, the power for the combined beam should the sum of all beams. (Report 38)

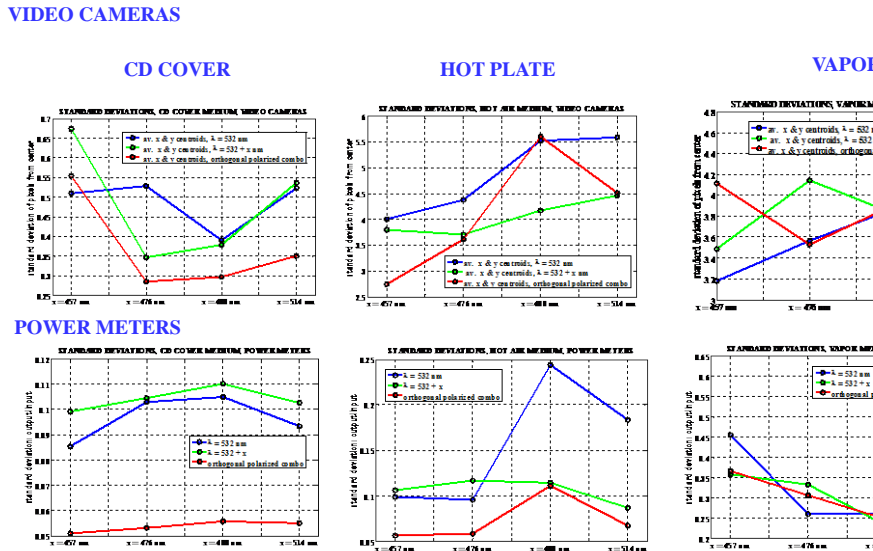


Fig 5.2.16 Media: Phase Plate, CD case, Heated Air, Water Vapor. Video cameras and power meter data. Top row: the  $\sigma$ 's for the cameras' x and y centroids were averaged. It can be seen that in the case of the CD cover, camera data, the combined beam condition clearly improves the  $\sigma$ 's (jitter). Bottom row: in the case of the power meter data, there is an extremely clear result of improvement for the combined beam condition in the case of the CD cover as well as some improvements in the case of the hot plate and vapor. (Report 38)

**STANDARD DEVIATIONS  
VIDEO CAMERAS & POWER METERS**

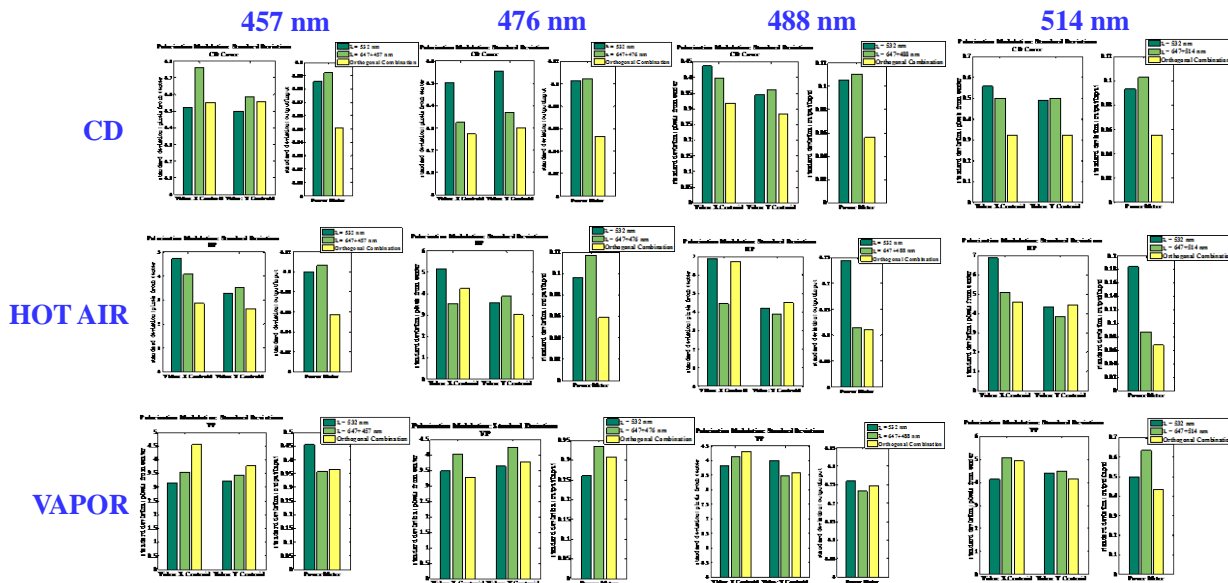


Fig 5.2.17 Media: Phase Plate, CD case, Heated Air, Water Vapor. An overview of the video camera and power meter together. In each of these bar graph combinations, the  $\sigma$ 's for the x and y centroids are the triplets on the left and the  $\sigma$ 's for the power meter are the triplets on the right. In all, the dark green indicates the diode laser ( $\lambda = 532$  nm) alone, the light green the Kr ( $\lambda = 532$  nm) + Ar ( $\lambda = 457, 476, 488$  or  $514$  nm) alone, and the yellow the combined beam. The combined beam improvement in  $\sigma$ 's is evident in the case of the CD cover. It is also evident in the case of the hot air medium for Ar ( $\lambda = 457, 476$  and  $514$  nm). The vapor condition – the most nonstationary – shows less improvement. (Report 38)

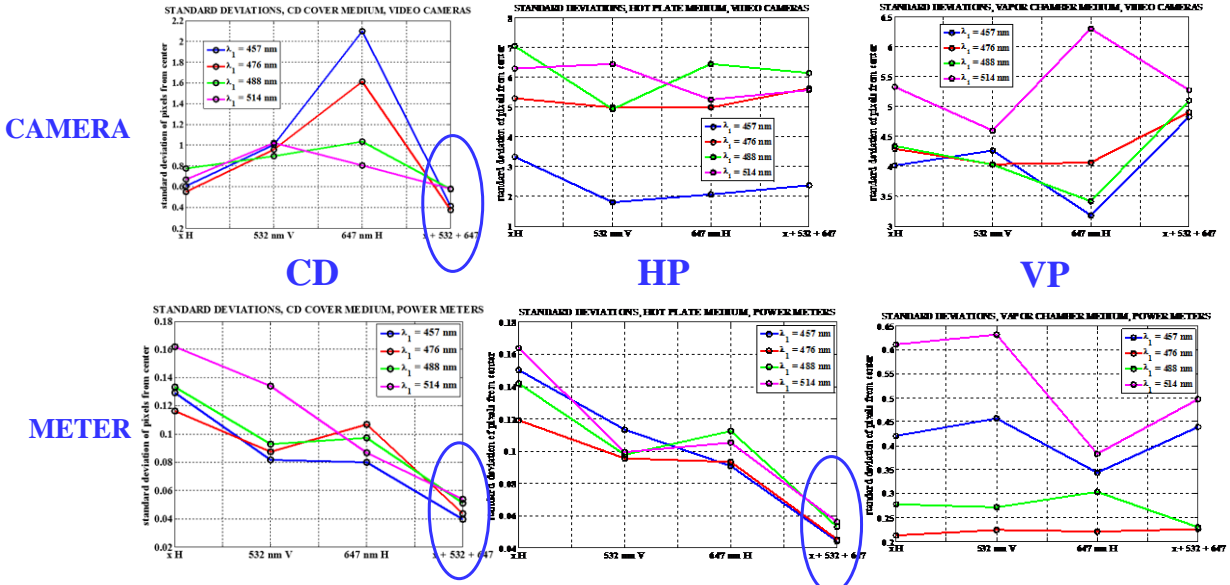


Fig 5.2.18 Media: Phase Plate, CD case, Heated Air, Water Vapor. Top row: camera, the  $\sigma$ 's for the  $d$  measures obtained from  $x$  and  $y$  centroids. It can be seen that in the case of the CD cover, camera data, the combined beam condition clearly improves the  $\sigma$ 's (jitter). Bottom row: in the case of the power meter data, there is an extremely clear result of improvement for the combined beam condition in the case of the CD cover as well as for the hot plate, but no improvement for the vapor. Ellipses indicate significant improvement. (Report 39)

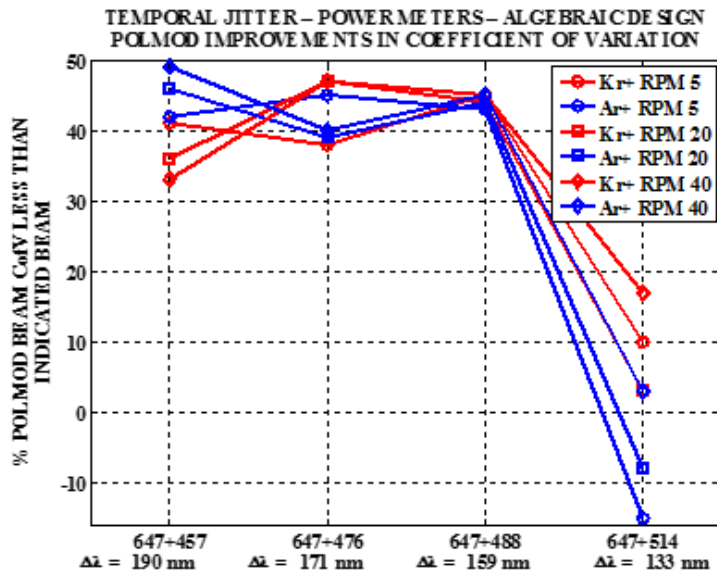


Fig 5.2.19 Medium: Rotating Phase Plate (see Fig 3.3 above). Temporal Jitter results, 2 Line Algebraic Design (see Figs 4.5.1-3 above). POLMOD improvements in the coefficient of variation, at phase plate rotations 5, 20 and 40 rpm, and with orthogonal beam wavelength separations of  $\Delta\lambda = 190$  nm (647 + 457 nm), 171 nm (647 + 476 nm), 159 nm (647 + 488 nm) and 133 nm (647 + 514 nm). Note the decline in coefficient of variation improvement at 133 nm (647 + 514 nm). (Report 43)

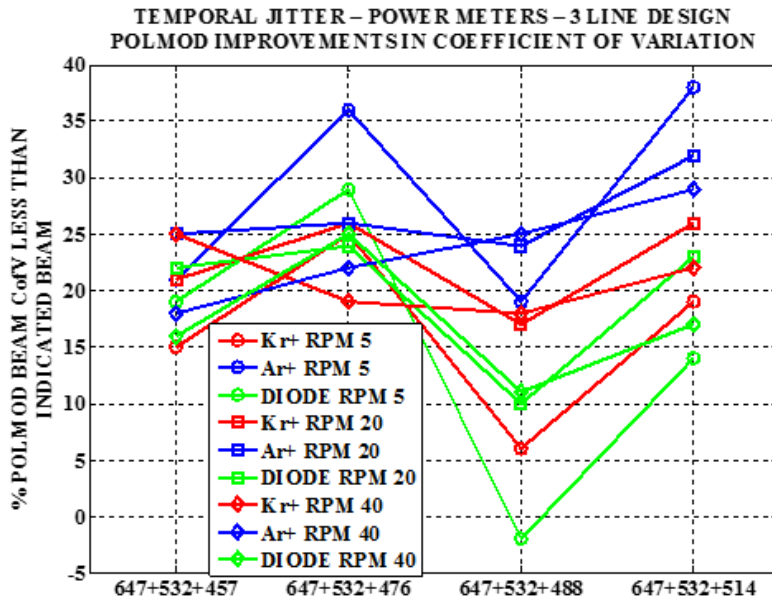


Fig 5.2.20 Medium: Rotating Phase Plate (see Fig 3.3 above). Temporal Jitter results, 3 Beam Design (Figs 4.6.1-3 above). POLMOD improvements in the coefficient of variation, at phase plate rotations 5, 20 and 40 rpm. Note the decline in the coefficient of variation improvement with combination 647 + 532 + 488 nm. (Report 43)

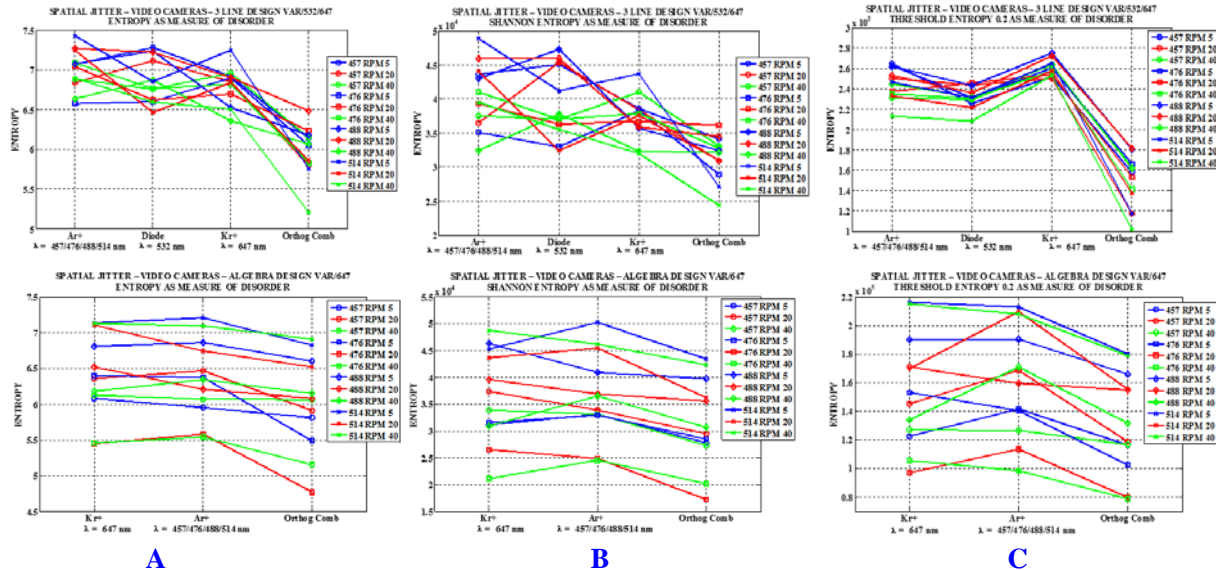


Fig 5.2.21 Medium: Rotating Phase Plate (see Fig 3.3 above). Upper Row: Line Design (Figs 4.6.1-3 above). Lower Row: Algebra Design (Figs 4.5.1-3 above).

A: Entropy Measure of Randomness .Clearly, in *all* instances at *all* wavelength combinations, the orthogonally combined beams reduce spatial jitter (dispersion) at *all* 3 RPMs of the phase plate (see Fig 1). Entropy\_B > Entropy\_A.

B: Shannon Wave Packet Entropy Measure of Randomness.. Clearly, and again, in *all* instances at *all* wavelength combinations, the orthogonally combined beams reduce spatial jitter (dispersion) at *all* 3 RPMs of the phase plate. Shannon\_entropy\_B > Shannon\_entropy\_A.

C: Threshold Wave Packet (0.2) Entropy Measure of Randomness. Clearly, and again, in *all* instances at *all* wavelength combinations, the orthogonally combined beams reduce spatial jitter (dispersion) at *all* 3 RPMs of the phase plate. Threshold\_entropy\_B > Threshold\_entropy\_A. (Report 44. SEP\_2014\_VIDEO\_CAMERAS)

## 6. GEOMETRIC ALGEBRA

### 6.1 INTRODUCTION

Polarization modulation finds an appropriate description in geometric (Clifford) algebra, rather than the conventionally used algebra of Gibbs and Heaviside. Here, we provide a short overview of this algebra (cf. Hestenes & Sobczyk, 1984; Chisholm & Common, 1986; Baylis, 1999; Doran & Lasenby, 2003; Arthur, 2011; Chappel, et al, 2014).

We treat two polarization modulation conditions provided by:

$$(1): \quad \text{beam 1} = a_1 \cos(2\pi \times 29 \times 10^{12} \times t); \text{ beam 2} = a_2 \cos(2\pi \times 29 \times 10^{12} \times t + \pi/2); a_1 = a_2 = 1.$$

$$(2): \quad \text{beam 1} = a_1 \cos(2\pi \times 32 \times 10^{12} \times t); \text{ beam 2} = a_2 \cos(2\pi \times 29 \times 10^{12} \times t); a_1 = a_2 = 1..$$

The amplitudes of two constituent beams forming a combined beam can be changed, but for purposes of exposition, they are not here.

The basis of geometric algebra is the geometric product, and the inner and outer products are derived constructions. For example:

$$\text{the geometric product of two vectors: } xy = x \wedge y + x \cdot y,$$

where “ $\cdot$ ” signifies the inner (dot) product and the symmetric part of the geometric product:

$$\text{the inner product of two vectors: } x \cdot y = 1/2(xy + yx)$$

and “ $\wedge$ ” signifies the outer product and the anti-symmetric part of the geometric product:

$$\text{the outer product of two vectors: } x \wedge y = 1/2(xy - yx).$$

Whereas the inner and outer products are not invertible, the geometric product is.

We seek an algebra that describes not just positions on the Poincaré sphere (static polarizations), but movements on the sphere (polarization modulation). Geometric algebra provides this algebra, because the geometric product is an operator for both a rotation and a dilation of one vector to another, and the rotation is defined as:

$$R = y/x = \frac{yx}{x \cdot y}.$$

Thus, given a combined wave, instantaneous polarization defined as  $x$  at instant  $t$ , and a combined wave instantaneous polarization defined as  $y$  at instant  $t + 1$ , we make the substitution in this instant, i.e.,  $x = y$ , repeating the process for  $t + 2$ , etc., then  $R$  defines the polarization modulation trajectory of the combined beam.

For the *steady state*, the polarization field,  $P$ , and the electric field,  $E$ , are related by the electric susceptibility tensor,  $\chi$ :

$$\begin{pmatrix} P_x \\ P_y \\ P_z \end{pmatrix} = \epsilon_0 \begin{pmatrix} \chi_{xx} & \chi_{xy} & \chi_{xz} \\ \chi_{yx} & \chi_{yy} & \chi_{yz} \\ \chi_{zx} & \chi_{zy} & \chi_{zz} \end{pmatrix} \begin{pmatrix} E_x \\ E_y \\ E_z \end{pmatrix}.$$

But this is for the steady state, and as the tests will involve plane waves, we can neglect the  $z$  spatial plane, and substitute sampling time,  $t$ , and molecular orientation time,  $\tau$ :

$$\begin{pmatrix} P_x \\ P_y \\ P_t \end{pmatrix} = \epsilon_0 \begin{pmatrix} \chi_{xx} & \chi_{xy} & \chi_{x\tau} \\ \chi_{yx} & \chi_{yy} & \chi_{y\tau} \\ \chi_{tx} & \chi_{ty} & \chi_{\tau\tau} \end{pmatrix} \begin{pmatrix} E_x \\ E_y \\ E_t \end{pmatrix}.$$

A similar relation exists between the magnetization, or magnetic dipole moment,  $M$ , the volume magnetic susceptibility,  $\chi^m$ , and the magnetic induction field,  $B$ :

$$\begin{pmatrix} M_x \\ M_y \\ M_t \end{pmatrix} = \mu_0^{-1} \begin{pmatrix} \chi_{xx}^m & \chi_{xy}^m & \chi_{x\tau}^m \\ \chi_{yx}^m & \chi_{yy}^m & \chi_{y\tau}^m \\ \chi_{tx}^m & \chi_{ty}^m & \chi_{\tau\tau}^m \end{pmatrix} \begin{pmatrix} B_x \\ B_y \\ B_t \end{pmatrix}.$$

Whereas the  $\mathbf{E}$  field is a conventional polar vector, the  $\mathbf{B}$  field is an axial vector, or bivector, that is, it is a directed area. The algebra of conventional electromagnetic theory is inappropriate for describing this difference. In the Figs 6.1.1-9 are shown the polar  $\mathbf{E}$  field and the accompanying axial (bivector)  $\mathbf{B}$  field *which arises when the  $\mathbf{E}$  field departs from linear polarization*. It is the rapid rate of change in the  $E$  and  $B$  fields that challenges the orientation and relaxation times of the electric susceptibility tensor,  $\chi$ , and the volume magnetic susceptibility,  $\chi^m$ .

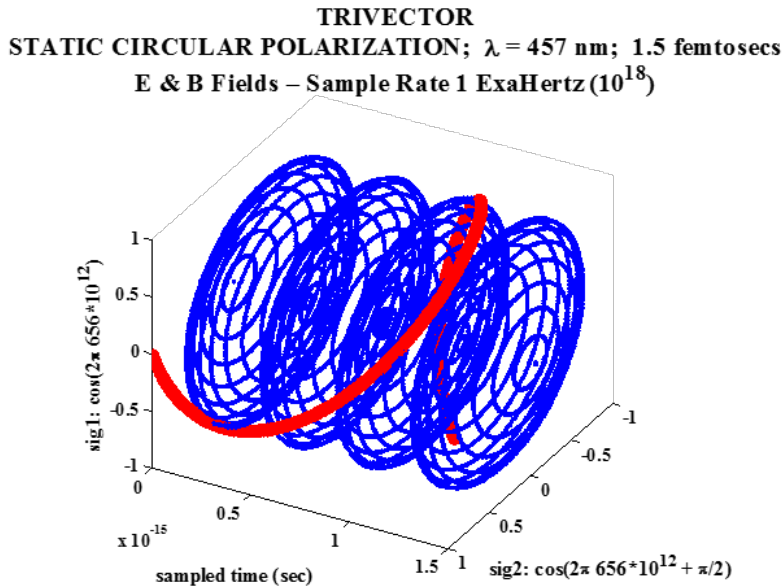


Fig 6.1.1.1 Representation of a trivector, which is formed by the outer product (or wedge product) of three independent vectors: e.g.,  $e_1 \wedge e_2 \wedge e_3$ , and is a directed volume element or oriented volume. In the present instance, a first linearly polarized  $\mathbf{E}$  beam (signal 1) is represented along  $e_1$ ; a second linearly  $\mathbf{E}$  polarized beam (signal 2) but orthogonally polarized to the first is represented along  $e_2$ ; and time, or the number of sampling intervals is represented along  $e_3$ . The combined static circularly polarized  $\mathbf{E}$  beam is shown in red – *the beam is not polarization modulated*. The  $\mathbf{B}$  field is shown as bivector areas in blue. A signed scalar denotes the volume of a trivector. There are 4 expansions and contractions of the  $\mathbf{B}$  field corresponding to one Lissajous pattern cycle of the  $\mathbf{E}$  field.

STATIC CIRCULAR POLARIZATION;  
 $\lambda = 457 \text{ nm}$ ; 1.5 femtoseconds  
E & B Fields – Sample Rate 1 ExaHertz ( $10^{18}$ )

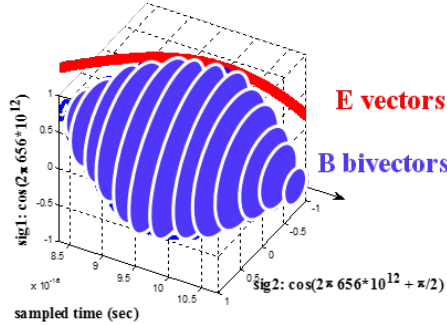


Fig 6.1.1.2 Partial representation of a trivector showing one expansion and contractions of the **B** field corresponding to one Lissajous pattern cycle of the **E** field.

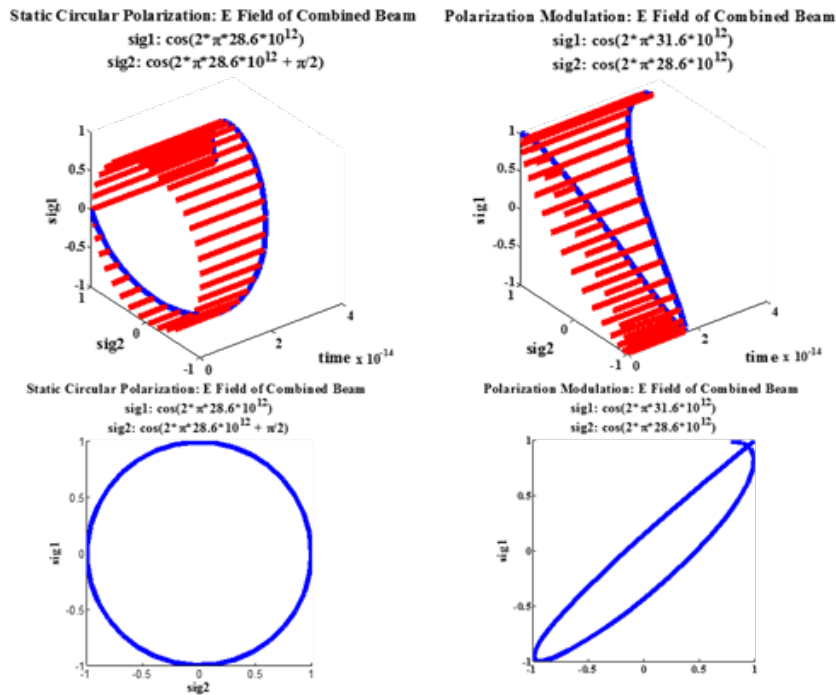


Fig 6.1.2: The combined beam **E** field trajectory in the x,y,t trivector (upper); viewed head-on (lower). In both A & B are shown 36 sampling points (= 36 femtoseconds) of the resultant summed trajectory of two orthogonally polarized beams (blue) with the amplitude of the 1<sup>st</sup> beam represented on the x-axis, and the amplitude of the 2<sup>nd</sup> beam on the y-axis. The red lines indicate the build over time of so-called polarization ellipses (or x-y plots, or Lissajous figures), and that are shown in Fig. 6.4. In A, the orthogonal beams are of the same frequency but offset by 90° – therefore, there is *static circular polarization*. In B, the orthogonal beams are of different frequencies resulting *polarization modulation*.

In A:  $beam 1 = a_1 \cos(2\pi \times 29 \times 10^{12} \times t)$ ;  $beam 2 = a_2 \cos(2\pi \times 29 \times 10^{12} \times t + \pi/2)$ ;  $a_1 = a_2 = 1$ .  
In B:  $beam 1 = a_1 \cos(2\pi \times 32 \times 10^{12} \times t)$ ;  $beam 2 = a_2 \cos(2\pi \times 29 \times 10^{12} \times t)$ ;  $a_1 = a_2 = 1$ .

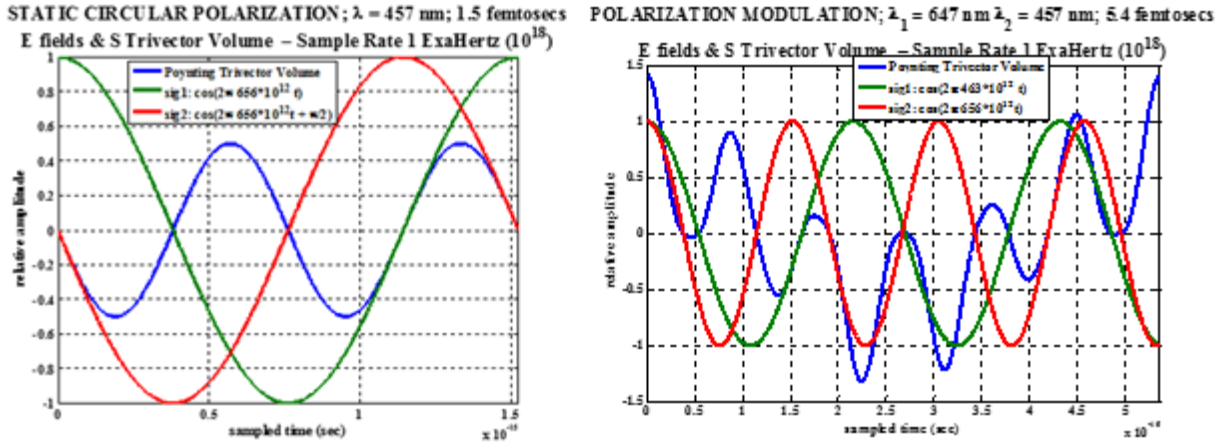


Fig 6.1.3 Two E fields and the S trivector volume for left: static circular polarization; and right: polarization modulation. (geometric\_algebra\_06(a0,a1,a3,a4); POLMOD\_MATLAB\_GEOMETRIC\_ALGEBRA\_03)

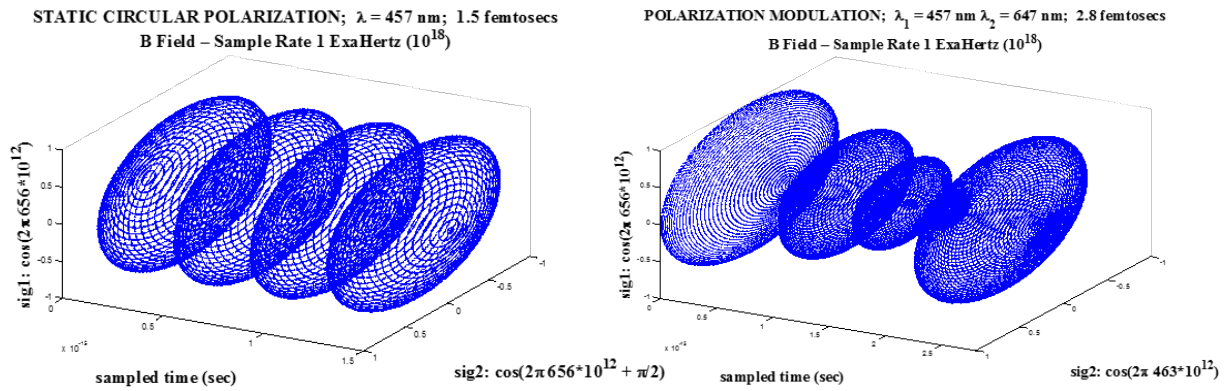


Fig 6.1.4 The **B** field in the  $x, y, t$  trivectors sampled at 1 ExaHertz ( $10^{18}$  Hz). The magnetic field, **B**, is a bivector and represented as a surface,  $\mathbf{B} = \mathbf{e}_1 \wedge \mathbf{e}_2$ , where, in the present instance, the 1<sup>st</sup> beam is represented along the  $\mathbf{e}_1$  axis, and the 2<sup>nd</sup> beam along the  $\mathbf{e}_2$  axis and orthogonal to 1<sup>st</sup>. The **B** field surface geometry is arbitrary and is shown here with a circular boundary. In A (static circular polarization) the representation is over 1.5 femtoseconds; in B (polarization modulation) the representation is over 2.8 femtoseconds.

In A:  $\text{beam 1} = a_1 \cos(2\pi \times 29 \times 10^{12} \times t)$ ;  $\text{beam 2} = a_2 \cos(2\pi \times 29 \times 10^{12} \times t + \pi/2)$ ;  $a_1 = a_2 = 1$ .  
 In B:  $\text{beam 1} = a_1 \cos(2\pi \times 32 \times 10^{12} \times t)$ ;  $\text{beam 2} = a_2 \cos(2\pi \times 29 \times 10^{12} \times t)$ ;  $a_1 = a_2 = 1$ .

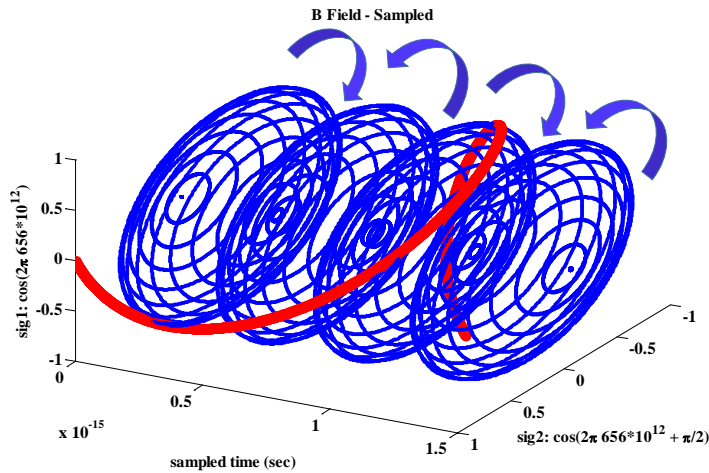


Fig 6.1.5 Representation of one cycle of the E field during which the B field progresses from (1) circularly polarized corotating; (2) controtating; (3) corotating; and (4) contrarotating. (PP POLMOD\_MATLAB\_GEOMETRIC\_ALGEBRA)

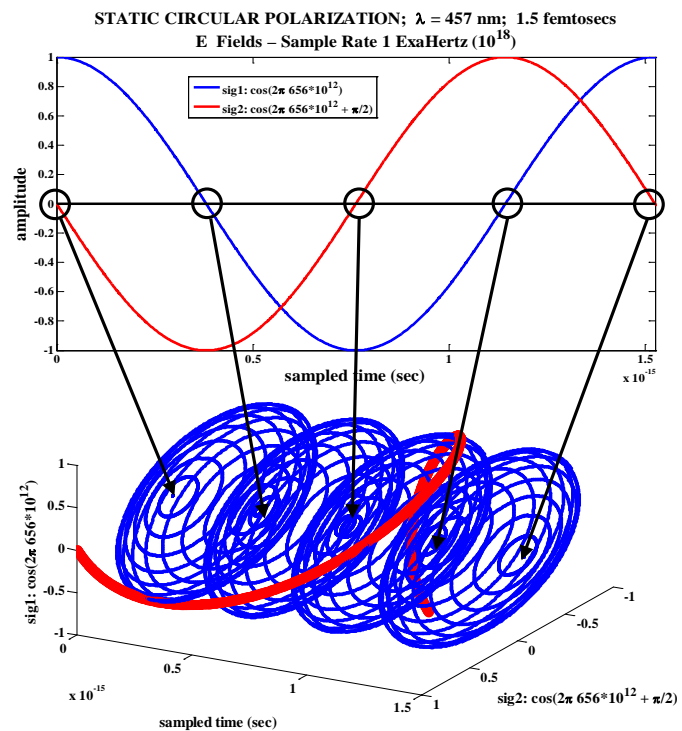
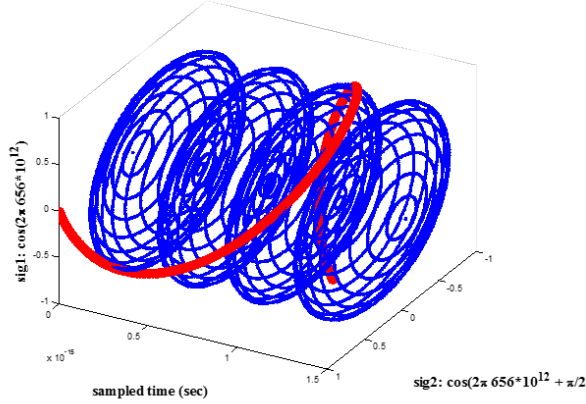


Fig 6.1.6 The progression from (1) circularly polarized corotating; (2) controtating; (3) corotating; and (4) contrarotating, shown in Fig 6.5, is made explicit from and examination of the two orthogonally polarized constituent beams of the combined beam.

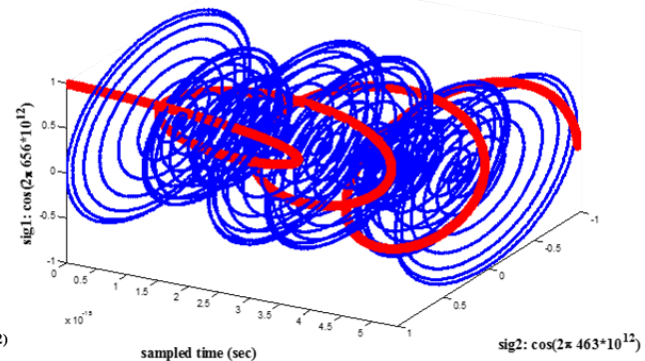
(PP POLMOD\_MATLAB\_GEOMETRIC ALGEBRA & POLMOD\_MATLAB\_GEOMETRIC\_ALGEBRA\_3)

STATIC CIRCULAR POLARIZATION;  $\lambda = 457 \text{ nm}$ ; 1.5 femtoseconds  
E & B Fields – Sample Rate 1 ExaHertz ( $10^{18}$ )



A

POLARIZATION MODULATION;  $\lambda_1 = 457 \text{ nm}$   $\lambda_2 = 647 \text{ nm}$ ; 5.4 femtoseconds  
E & B Fields – Sample Rate 1 ExaHertz ( $10^{18}$ )



B

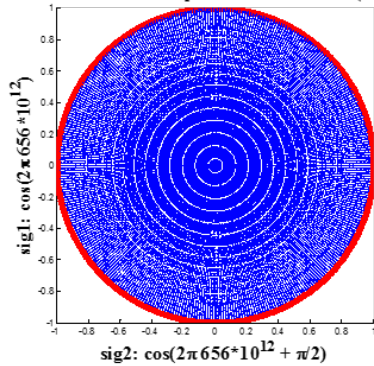
Fig 6.1.7 **E** and **B** field representations. The termination of the **E** vector is shown in red. The extent of the area of the **B** bivector is shown in blue. Sample rate is 1 ExaHertz ( $10^{18}$  Hz).

In A (*a static circular polarization*) the representation is over 1.5 femtoseconds; in B (*a polarization modulation*) the representation is over 5.4 femtoseconds.

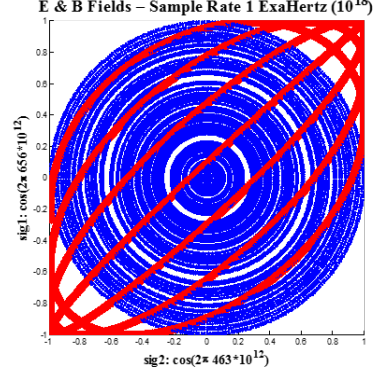
In A:  $\text{beam 1} = a_1 \cos(2\pi \times 29 \times 10^{12} \times t)$ ;  $\text{beam 2} = a_2 \cos(2\pi \times 29 \times 10^{12} \times t + \pi/2)$ ;  $a_1 = a_2 = 1$ .

In B:  $\text{beam 1} = a_1 \cos(2\pi \times 32 \times 10^{12} \times t)$ ;  $\text{beam 2} = a_2 \cos(2\pi \times 29 \times 10^{12} \times t)$ ;  $a_1 = a_2 = 1$ .

STATIC CIRCULAR POLARIZATION;  $\lambda = 457 \text{ nm}$ ; 1.5 femtoseconds    POLARIZATION MODULATION;  $\lambda_1 = 457 \text{ nm}$   $\lambda_2 = 647 \text{ nm}$ ; 5.4 femtoseconds  
E & B Fields – Sample Rate 1 ExaHertz ( $10^{18}$ )



A



B

Fig 6.1.8 **E** and **B** fields of Fig 6.1.7 shown head-on as Lissajous patterns. The termination of the **E** vector is shown in red. The extent of the area of the **B** bivector is shown in blue. Sample rate is 1 ExaHertz ( $10^{18}$  Hz).

In A (*a static circular polarization*) the representation is over 1.5 femtoseconds; in B (*a polarization modulation*) the representation is over 5.4 femtoseconds.

In A:  $\text{beam 1} = a_1 \cos(2\pi \times 29 \times 10^{12} \times t)$ ;  $\text{beam 2} = a_2 \cos(2\pi \times 29 \times 10^{12} \times t + \pi/2)$ ;  $a_1 = a_2 = 1$ .

In B:  $\text{beam 1} = a_1 \cos(2\pi \times 32 \times 10^{12} \times t)$ ;  $\text{beam 2} = a_2 \cos(2\pi \times 29 \times 10^{12} \times t)$ ;  $a_1 = a_2 = 1$ .

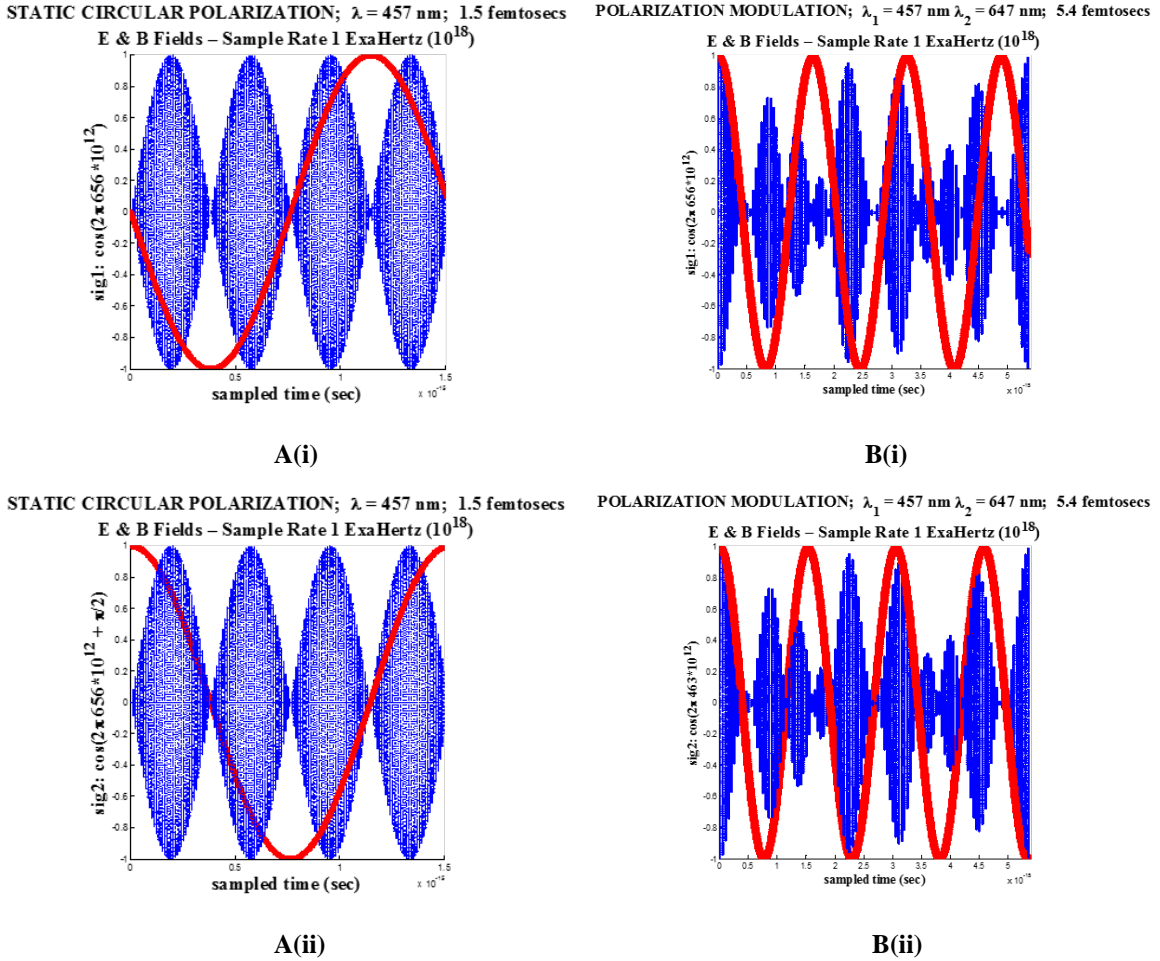


Fig 6.1.9 **E** and **B** fields of Fig 6.1.7 shown side-on. In (i) side-on to beam 1. In (ii) side-on to beam 2. The termination of the **E** vector is shown in red. The extent of the area of the **B** bivector is shown in blue. Sample rate is 1 ExaHertz ( $10^{18}$  Hz).

In A (*a static circular polarization*) the representation is over 1.5 femtosecs; in B (*a polarization modulation*) the representation is over 5.4 femtosecs.

In A:  $\text{beam 1} = a_1 \cos(2\pi \times 29 \times 10^{12} \times t); \text{beam 2} = a_2 \cos(2\pi \times 29 \times 10^{12} \times t + \pi/2); a_1 = a_2 = 1.$

In B:  $\text{beam 1} = a_1 \cos(2\pi \times 32 \times 10^{12} \times t); \text{beam 2} = a_2 \cos(2\pi \times 29 \times 10^{12} \times t); a_1 = a_2 = 1.$

## 6.2 KNOTTED BEAMS

We seek to establish a correspondence between one algebra – the Clifford/Geometric algebra which is coordinate free – and another algebra – tensor algebra which is coordinate specific. The knotted beam approach is based on a tensor algebra (Rañada, 1989, 1992a&b; Rañada & Trueba, 1995-1998, 2001; Irvine, 2010; Irvine & Bouwmeester, 2008; Kleckner & Irvine, 2013; Kedia et al, 2013).

It seems it is critical to acknowledge that the pair of complex scalar fields of the knotted beam approach,  $\varphi, \theta$ , are a pair of complex scalar fields considered to be dual, as there exists in 3D a duality between a vector basis which is contravariant, and a bivector basis which is covariant. (However, in 4D the duality is between vectors and trivectors.) If that is acknowledged, then it is possible to compare and contrast the two algebras, the one based on quaternion numbers ( $S^3$ , the SU(2) group and geometric algebra) and the other based on complex numbers ( $S^2$ , the U(1) group and knotted beam). It is this strong form of duality (vector-to-bivector) in which the fields **E** and **B** are dual.

But the concept of duality has multiple meanings besides this strong form. We show that it is possible to create knotted structures commencing with two orthogonal beams (as in POLMOD) that are dual in a weak sense – e.g., theorems, concepts applied to one beam, equally apply to the other beam. As an exercise, we proceed to create a trefoil knot on the extended Poincaré sphere – i.e., the  $S^2$  sphere extended to an  $S^3$  sphere by indicated movement, demonstrating that knotted structures can be created from *two fields* that are dual in the weak sense. Therefore, a knotted theory does not provide necessarily a relation of **E** to **B**, which are dual in the strong sense.

Fig 6.2.1.A shows a continuous beam in 3D constructed from the two orthogonal signals:

$$\begin{aligned} 4 \cos(2t) + 2 \cos(t), \\ 4 \sin(2t) - 2 \sin(t). \end{aligned}$$

Viewed head-on (Fig 6.2.1.B), the trefoil knot is apparent. The two constituent signals are shown in Fig 6.2.1.C.

Represented on an  $S^3$  Poincaré sphere (i.e., movements are indicated across the  $S^3$  sphere), Figs 6.2.2.A-C, the trefoil knot is also apparent. Knotted structures can therefore be created from fields that are dual in the weak sense. One might state therefore, that the linking number is conserved (conservation of helicity) for fields defined by:

$$\int \mathbf{E}_1 \cdot \mathbf{E}_2 = 0,$$

where  $\mathbf{E}_1$  and  $\mathbf{E}_2$  are two orthogonal **E** (polar vector) fields. The bivector **B** field is derived from these **E** fields.

$$4 \cos(2t) + 2 \cos(t), \\ 4 \sin(2t) - 2 \sin(t).$$

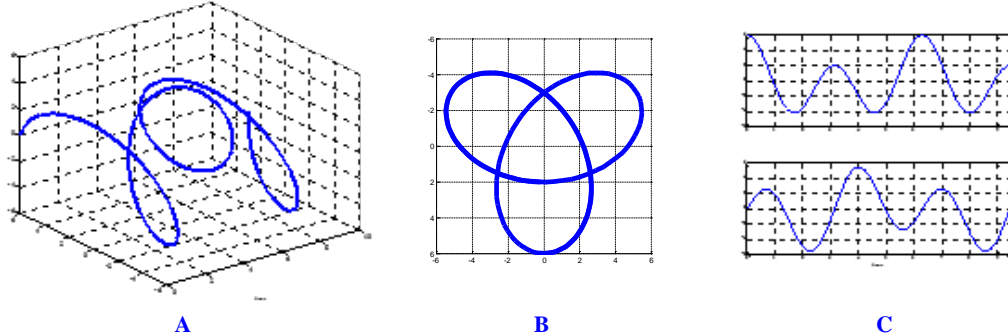


Fig 6.2.1.A A trefoil knot created from 2 orthogonal signals:

$$4 \cos(2t) + 2 \cos(t), \\ 4 \sin(2t) - 2 \sin(t).$$

Fig 6.2.1B The trefoil knot of A viewed head-on (azimuth & elevation = (90,90), i.e., a Lissajous pattern with time suppressed). (Report 29 – POLMOD\_MATLAB\_KNOTS\_03)

Fig 6.2.1C The 2 orthogonal signals of Fig 7A:

$$4 \cos(2t) + 2 \cos(t) , \text{upper} \\ 4 \sin(2t) - 2 \sin(t) \text{ lower.}$$

(Report 29 – POLMOD\_MATLAB\_KNOTS\_03)

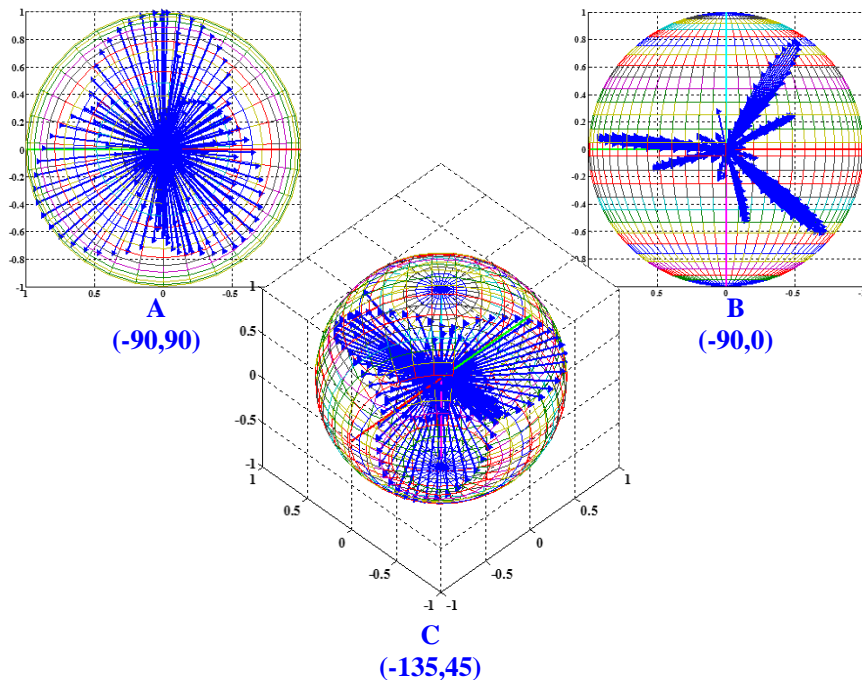


Fig 6.2.2

A: The composite modulated signal of Fig 6.2.1A projected on the Poincaré sphere and viewed (azimuth & elevation) (-90,90). Notice the trefoil knot.

B: The composite modulated signal of Fig 6.2.1A projected on the Poincaré sphere and viewed (azimuth & elevation) (-90, 0).

C: The composite modulated signal of Fig 6.2.1A projected on the Poincaré sphere and viewed (azimuth & elevation) (-135, 45). Again, notice the trefoil knot.

(Report 29 – POLMOD\_MATLAB\_KNOTS\_03; POLMOD\_POWP\_GEOMETRIC\_ALGEBRA\_03)

The goal of the series of tests was to demonstrate optimum propagation through disturbed atmospheres/ionospheres by means of polarization modulation (POLMOD) and axial modulation (AXMOD) techniques using two polarized continuous beam lasers of different wavelength,  $\Delta\lambda = \lambda_2 - \lambda_1$ , such that the polarization or rotational compatibility with induced polarizations in media is of a duration  $\tau = 1/\Delta f$ ,  $\Delta f = (f_1 - f_2)/2$ ,  $f_1 = c/\lambda_1$ ,  $f_2 = c/\lambda_2$ , that is less than the electronic, vibrational or rotational relaxation times of such media.

Such continuous beams rapidly changing in polarization or rotation find a description in geometric and Clifford algebras (Hestenes & Sobczyk, 1984; Chisholm & Common, 1986; Baylis, 1999; Doran & Lasenby, 2003; Arthur, 2011; Chappel, et al, 2014) that are coordinate-free. In such algebras a distinction is made between the electric field,  $\mathbf{E}$ , represented as a vector, or directed line segment, and the magnetic field,  $\mathbf{B}$ , represented as a bivector or 2-vector, or oriented line segment.

Here we address two aspects of the optimum propagation project: (1) development of a *steady state* geometric algebra description of the electromagnetic field-medium interaction; and (2) commences an extension of that description to the *transient state* by addressing a model system – a liquid crystal medium – the transient state (onset and offset times) of which a considerable literature exists.

We show a relation of the angle,  $\theta$ , between the electric field,  $\mathbf{E}$ , and the electric displacement,  $\mathbf{D}$ , adequately described in the geometric algebra description of electromagnetism to the angle,  $\theta$ , defined with respect to a unit vector angle of incident radiation and to media with induced dipoles. The latter is related to the optical response times ( $T_{\text{rise}}$  and  $T_{\text{decay}}$ ) that are linearly proportional to media director reorientation times ( $t_{\text{rise}}$  and  $t_{\text{decay}}$ ).

A first observation is that there is a direct geometrical interpretation of anisotropy without the intervention of any coordinate system. In Art. 794 (p. 443) of his 1873 Treatise James Clerk Maxwell stated that:

“in certain media the specific capacity for electrostatic induction is different in different directions, or in other words, the electric displacement, instead of being in the same direction as the electromotive intensity, and proportional to it, is related to it by a system of linear equations.”

With this definition of an electrically anisotropic medium, there have been three approaches to the description of anisotropic media: (1) the tensor method; (2) differential forms; and (3) Clifford geometric algebra method. Here, we implement the geometric algebra method, adopting the recent application of this method by Matos et al (2007), which, in turn, builds on the work of Hestenes and others, as well as the founders: Grassmann, Hamilton and Clifford.

If a medium is electrically anisotropic, an angle between the electric field vector,  $\mathbf{E}$ , (in the present instance  $\mathbf{E}$  being a laser beam), and the electric displacement vector,  $\mathbf{D}$ , depends on the direction of the Euclidean space along which  $\mathbf{E}$  is directed. This observation amounts to the impossibility of writing  $\mathbf{D} = \epsilon_0 \epsilon \mathbf{E}$ , where  $\epsilon_0$  is the permittivity of the vacuum, and  $\epsilon$  is the relative permittivity of the medium. Whereas this problem is addressed by tensor algebra by introducing a  $3 \times 3$  permittivity tensor, in geometric algebra, the anisotropy is written as:

$$\mathbf{D} = \epsilon_0(\boldsymbol{\epsilon} \mathbf{E}),$$

where  $(\boldsymbol{\epsilon}\mathbf{E})$  is a linear function that maps vectors to vectors and  $\boldsymbol{\epsilon}$  is a dielectric function that is defined along a particular direction for a particular medium<sup>6</sup>. The following definitions are required to develop the algebra.

The geometric product is defined as the graded sum:

$$u = \mathbf{ED} = \mathbf{E} \cdot \mathbf{D} + \mathbf{E} \wedge \mathbf{D} = \alpha + \mathbf{F},$$

where:

$\alpha = \mathbf{E} \cdot \mathbf{D}$  is the dot or inner product and symmetric,

$\mathbf{F} = \mathbf{E} \wedge \mathbf{D}$  is the outer exterior product, is antisymmetric, associative, is a bivector and a directed plane segment<sup>7</sup>.

The outer product of a vector and a bivector produced a trivector,  $\mathbf{V}$ , which is an oriented volume element.

A multivector is a sum of a scalar, a vector, a bivector and a trivector, e.g.:

$$u = \alpha + \mathbf{a} + \mathbf{F} + \mathbf{V}.$$

The reverse of  $u$  is defined as  $\tilde{u}$ , so that:

$$\tilde{u} = \mathbf{DE} = \mathbf{D} \cdot \mathbf{E} - \mathbf{D} \wedge \mathbf{E} = \alpha + \mathbf{F},$$

$$\alpha = \mathbf{E} \cdot \mathbf{D} = (u + \tilde{u})/2,$$

$$\mathbf{F} = \mathbf{E} \wedge \mathbf{D} = (u - \tilde{u})/2,$$

$$|u|^2 = u\tilde{u} = \mathbf{EDDE} = \mathbf{E}^2 \mathbf{D}^2 = (\alpha + \mathbf{F})(\alpha - \mathbf{F}) = \alpha^2 - \mathbf{F}^2 = \alpha^2 + \beta^2 = \rho^2,$$

If the unit bivector is such that  $\hat{\mathbf{F}}^2 = -1$ , then:

$$u = \alpha + \beta \hat{\mathbf{F}} = \rho \cos(\theta) + \hat{\mathbf{F}} \rho \sin(\theta),$$

$$\rho = |\mathbf{E}| |\mathbf{D}| = \sqrt{\alpha^2 + \beta^2}, \text{ and}$$

$$\mathbf{F} = \beta \hat{\mathbf{F}}.$$

Any bivector is the dual of a vector.

In geometric algebra,  $\mathcal{C}\ell_3$ , a multivector is an operation that projects onto a chosen grade  $k$ , where  $k = 0, 1, 2, 3$ , giving the structure:

$$\mathcal{C}\ell_3 = \mathbb{R} \oplus \mathbb{R}^3 \oplus \Lambda^2 \mathbb{R}^3 \oplus \Lambda^3 \mathbb{R}^3.$$

---

<sup>6</sup> A dielectric tensor coordinate system can be recaptured by defining:  $\epsilon_{ij} = \mathbf{e}_j \cdot \boldsymbol{\epsilon}(\mathbf{e}_k)$ .

<sup>7</sup> In contrast, the Gibbs cross product is:  $\mathbf{E} \times \mathbf{D}$  which is a vector, not associative, and is a directed line segment.

A  $k$ -blade of  $\mathcal{C}\ell_3$  is an element  $u_k$  such that  $u_k = \langle u_k \rangle_k$ , where  $\langle u_k \rangle_k$  is a homogeneous multivector of grade  $k$ .

Any trivector can be written as  $\mathbf{V} = \beta \mathbf{e}_{123}$ , where  $\beta \in \mathbb{R}$  and  $\mathbf{e}_{123} = \widehat{\mathbf{V}}$  is the unit trivector such that  $\mathbf{e}_{123}^2 = -1$ . With these definitions, two vectors,  $\mathbf{a}$  and  $\mathbf{b}$  ( $\mathbf{a}, \mathbf{b} \in \mathbb{R}^3$ ) are related by outer and cross products:

$$\mathbf{a} \wedge \mathbf{b} = (\mathbf{a} \times \mathbf{b}) \mathbf{e}_{123},$$

$$\mathbf{a} \times \mathbf{b} = -(\mathbf{a} \wedge \mathbf{b}) \mathbf{e}_{123}.$$

Geometric algebra  $\mathcal{C}\ell_3$  is a linear space of dimensions  $1 + 3 + 3 + 1 = 2^3 = 8$ , with  $\{\mathbf{e}_1, \mathbf{e}_2, \mathbf{e}_3\}$  as an orthonormal basis for vector space  $\mathbb{R}^3$ . The  $\mathcal{C}\ell_3$  space is characterized by:

$$\left\{ \underbrace{1}_{\text{scalars}}, \underbrace{\mathbf{e}_1, \mathbf{e}_2, \mathbf{e}_3}_{\text{vectors}}, \underbrace{\mathbf{e}_{12}, \mathbf{e}_{31}, \mathbf{e}_{23}}_{\text{bivectors}}, \underbrace{\mathbf{e}_{123}}_{\text{trivectors}} \right\}$$

where:

$$\mathbf{e}_{12} = \mathbf{e}_1 \wedge \mathbf{e}_2 = \mathbf{e}_1 \mathbf{e}_2,$$

$$\mathbf{e}_{31} = \mathbf{e}_3 \wedge \mathbf{e}_1 = \mathbf{e}_3 \mathbf{e}_1, \text{ and}$$

$$\mathbf{e}_{23} = \mathbf{e}_2 \wedge \mathbf{e}_3 = \mathbf{e}_2 \mathbf{e}_3,$$

is the basis for the subspace  $\wedge^2 \mathbb{R}^3$  of bivectors or 2-blades.

A medium is anisotropic if the angle,  $\theta$ , between the electric field,  $\mathbf{E}$ , and the electric displacement,  $\mathbf{D}$ , is different for different directions of  $\mathbf{E}$ . Therefore, with the above definitions:

$$\beta = \beta(\theta) = \rho \sin(\theta), \text{ or}$$

$$\beta = |\mathbf{F}| = |\langle \mathbf{E} \mathbf{D} \rangle_2| = |\mathbf{E} \wedge \mathbf{D}|,$$

definitions which depend on the direction in which  $\mathbf{E}$  is applied –  $\mathbf{E}$  being, in the present circumstances, the incident laser beam.

With:

$$\mathbf{E} = |\mathbf{E}| \mathbf{s},$$

$$\mathbf{D} = |\mathbf{D}| \mathbf{t}, \text{ and}$$

$$\mathbf{s}^2 + \mathbf{t}^2 = 1, \text{ then}$$

$$\hat{\mathbf{F}} = \mathbf{s} \wedge \mathbf{t} / \sin(\theta) = \mathbf{s} \mathbf{r}$$

$$\mathbf{r}^2 = 1.$$

It follows that:

$$\mathbf{D} = \mathbf{D}_{||} + \mathbf{D}_{\perp},$$

$$D_{||} = \mathbf{s} \cdot \mathbf{D}_{||} = |\mathbf{D}| \cos(\theta),$$

$$D_{\perp} = \mathbf{r} \cdot \mathbf{D}_{\perp} = |\mathbf{D}| \sin(\theta).$$

These relations are shown in Fig 1 (Matos et al, 2007).

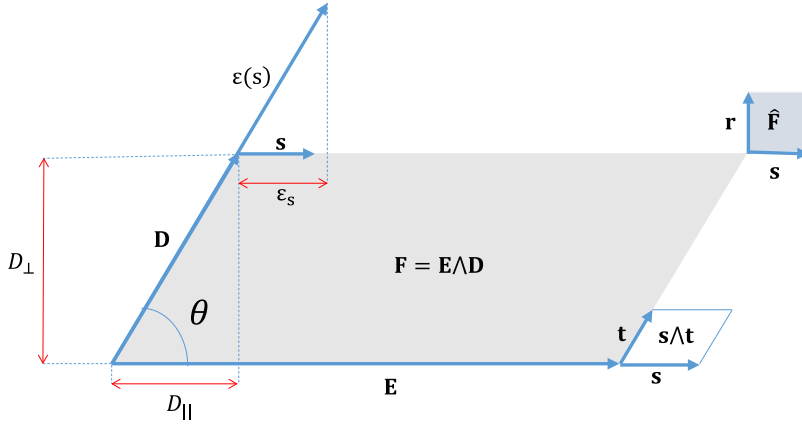


Fig 6.2.3 From Matos, S.A., Ribeiro, M.A. & Paiva, C.R., Anisotropy without tensors: a novel approach using geometric algebra. *Optics Express*, 15, 15175-15186, 2007. (Report 30)

These relations permit a definition of relative permittivity:

$$\epsilon_s = \mathbf{s} \cdot \epsilon(\mathbf{s}),$$

with  $\epsilon_s = 0$  if  $\mathbf{E} \perp \mathbf{D}$ .

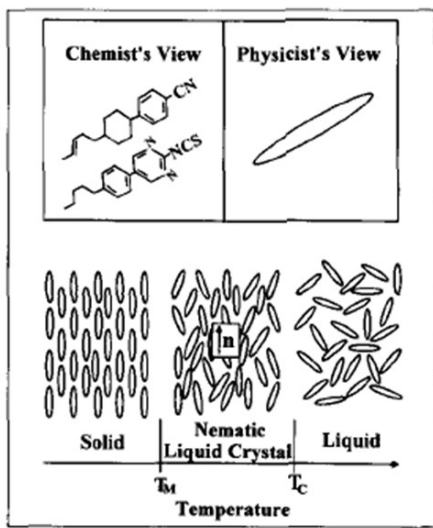
In the case of a lossless nonmagnetic medium,

$$\epsilon(\mathbf{a}) = \lambda \mathbf{a},$$

which provides three positive eigenvalues,  $\epsilon_1$ ,  $\epsilon_2$  and  $\epsilon_3$  corresponding to the three unit eigenvectors  $\mathbf{e}_1$ ,  $\mathbf{e}_2$  and  $\mathbf{e}_3$ .

### 6.3 TEMPORAL DEPENDENCE OF ANISOTROPY

We now turn to the temporal dependence of  $\theta$ , using liquid crystals (LCs) as a model system displaying temporal dependence of dielectric anisotropy. As Fig 6.3.1 shows, an LC will align perpendicular or parallel to incident radiation, and the angle  $\theta$  is defined as the angle between the unit vector of the incident radiation and the orientation of the LC (Fig 6.3.2). From the molecular point of view, the origin of the dielectric anisotropy is the anisotropic distribution of the molecular dipoles in the liquid crystal phases.



### Characteristic

- Organic substance in the state between solid and Liquid state
- Temperature between  $T_m$  and  $T_c$
- Thin and Elongated structure
- Strong dipoles or easily polarizable substituents

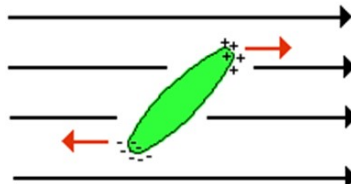


Fig 6.3.1 In the case of positive dielectric anisotropy, the liquid crystal will align parallel to the electric field. Upon application of an electric field, the positive charge is displaced to one end of the molecule and the negative charge to the other end, thus creating an induced dipole moment. This results in the alignment of the longitudinal axis of liquid crystal molecules mutually parallel to the electric field direction. In the case of negative dielectric anisotropy, the liquid crystal will align perpendicular to the electric field. The index of refraction is larger along with the long axis of the molecules, then the perpendicular to it. (After Kai Chung Wong). (Report 30)

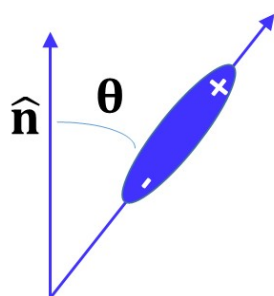


Fig 6.3.2 Angle,  $\theta$ , defined with respect to unit vector angle of incident of radiation and LC. The unit vector is referred to as “the director”. (Report 30)

Maier and Meier (1961) extended Onsager theory to nematic LC. In their theory, a molecule is represented by an anisotropic polarizability  $\alpha$  with principal elements  $\alpha_1$  and  $\alpha$  in a

spherical cavity of radius  $a$ . Denoting the dipole moment with  $a_1$  at an angle  $\theta$ , the LC dielectric components  $\varepsilon_{||}$ ,  $\varepsilon_{\perp}$  and  $\Delta\varepsilon$ , can be expressed as:

$$\begin{aligned}\varepsilon_{||} &= NhF\{\langle\alpha_{||}\rangle + (F\mu^2/3kT)[1 - (1 - 3\cos^2\theta)S]\}, \\ \varepsilon_{\perp} &= NhF\{\langle\alpha_{\perp}\rangle + (F\mu^2/3kT)[1 + (1 - 3\cos^2\theta)S/2]\}, \\ \Delta\varepsilon &= NhF\{\langle\alpha_1 - \alpha_t\rangle + (F\mu^2/2kT)(1 - 3\cos^2\theta)\},\end{aligned}$$

where:

$N$  is the molecular packing density,

$\mu$  is the dipole moment,

$F$  is the Onsager reaction field,

$S$  is an order parameter described by:  $S = (1 - T/T_c)^{\beta}$ ,

$\beta$  is a coefficient dependent on molecular structure,

$T_c$  is the clearing temperature,

$\langle n \rangle$  is the average refractive index,

$\langle \varepsilon \rangle$  is the average dielectric constant,

and

$$\begin{aligned}h &= \frac{3\langle \varepsilon \rangle}{2\langle \varepsilon \rangle + 1}, \\ F &= \frac{(2\langle \varepsilon \rangle + 1)(\langle n \rangle^2 + 2)}{3(2\langle \varepsilon \rangle + \langle n \rangle^2)},\end{aligned}$$

Indicating that the dielectric anisotropy of a LC is a function of three factors: molecular structure, temperature and frequency.

Overall LC performance can be characterized by a figure-of-merit (FoM) (Khoo & Wu, 1993):

$$FoM = \frac{\Delta n^2}{\gamma_1/K_{11}},$$

where:

$K_{11}$  is the splay elastic constant,

$\Delta n$  is the birefringence,

$\gamma_1$  is the rotational viscosity.

All three parameters are temperature dependent and the viscosity and elastic constants are dependent on the order parameter  $S$ .

When the applied voltage exceeds the Freedericksz transition voltage  $V_{th}$ , the LC molecules will rotate and be reoriented by the electric field, causing the change of the permittivity of substrate. The electric energy under the applied voltage is given by (Wang, 2005):

$$f_{Electric} = \iiint \left( \frac{1}{2} D \cdot E \right) dv = \iiint \left( \frac{1}{2} \varepsilon \nabla V \cdot \nabla V \right) dv,$$

where  $V$  is the voltage distribution and  $\varepsilon$  is the dielectric tensor of the LC medium.

The relative dielectric tensor is:

$$\varepsilon_r = \begin{bmatrix} \varepsilon_{xx} & \varepsilon_{xy} & \varepsilon_{xz} \\ \varepsilon_{yx} & \varepsilon_{yy} & \varepsilon_{yz} \\ \varepsilon_{zx} & \varepsilon_{zy} & \varepsilon_{zz} \end{bmatrix},$$

and, referring to Fig 6.3.3:

$$\begin{aligned} \varepsilon_{xx} &= n_o^2 + (n_e^2 - n_o^2)\cos^2\theta\cos^2\phi, \\ \varepsilon_{yy} &= n_o^2 + (n_e^2 - n_o^2)\cos^2\theta\sin^2\phi, \\ \varepsilon_{zz} &= n_o^2 + (n_e^2 - n_o^2)\sin^2\theta, \\ \varepsilon_{yz} &= \varepsilon_{zy} = (n_e^2 - n_o^2)\sin\theta\cos\phi\sin\phi, \\ \varepsilon_{xy} &= \varepsilon_{yx} = (n_e^2 - n_o^2)\cos^2\theta\sin\phi\cos\phi, \\ \varepsilon_{xz} &= \varepsilon_{zx} = (n_e^2 - n_o^2)\sin\theta\cos\theta\cos\phi, \end{aligned}$$

$n_o$  is the ordinary refractive index of the LC medium,

$n_e$  is the extraordinary refractive index of the LC medium,

$\theta$  is the tilt angle of the LC director (Fig 6.3.3),

$\phi$  is the azimuthal angle between projection of the LC director on the x-y plane and the x-axis (Fig 6.3.3).

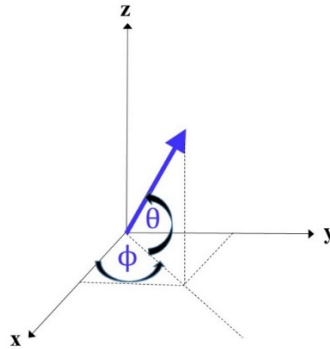


Fig 6.3.3 The coordinate system of a LC director. (Report 30)

The optical response time for amplitude modulation and phase response time for phase modulation is related to the LC director reorientation time. The dynamics of the LC director reorientation is described by (Erickson, 1961; Leslie, 1968):

$$\begin{aligned} & (K_{11}\cos^2\phi + K_{33}\sin^2\phi) \frac{\partial^2\phi}{\partial z^2} + (K_{33} - K_{11})\sin\phi\cos\phi \left( \frac{\partial\phi}{\partial z} \right)^2 \\ & + \varepsilon_o\Delta\varepsilon E^2\sin\phi\cos\phi = \gamma_1 \frac{\partial\phi}{\partial t}, \end{aligned}$$

where:

$\gamma_1$  is the rotational viscosity,

$K_{11}$  and  $K_{33}$  are the splay and bend elastic constants,  
 $\varepsilon_0 \Delta \varepsilon E^2$  is the electric field energy density,  
 $\Delta \varepsilon$  is the dielectric anisotropy, and  
 $\phi$  is the tilt angle of the LC directors.

If the tilt angle is small ( $\sin \phi \sim \phi$ ) and  $K_{33} \sim K_{11}$  (small angle approximation), then a reduction is possible to (Wang, 2005):

$$K_{33} \frac{\partial^2 \phi}{\partial z^2} + \varepsilon_0 \Delta \varepsilon E^2 \phi = \gamma_1 \frac{\partial \phi}{\partial t}.$$

With  $\alpha$  defined as the pretilt angle or the angle of the LC directors deviated from the LC normal, so that if  $\alpha = 0$  the LC directors are aligned perpendicular to the incident beam, the optical rise time (10%→90%) as a function of  $V/V_{th}$  at four different pretilt angles,  $\alpha = 1^\circ, 2^\circ, 3^\circ$ , and  $5^\circ$  can be calculated<sup>10</sup> (Fig 5). Optical response times ( $T_{rise}$  and  $T_{decay}$ ) are linearly proportional to the LC director reorientation times ( $\tau_{rise}$  and  $\tau_{decay}$ ).

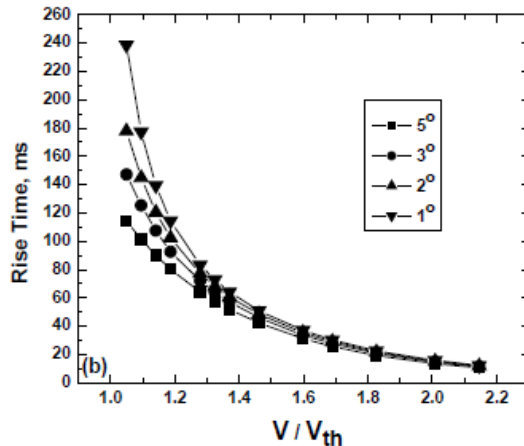


Fig 6.3.4: Optical rise time (10%→90%) as a function of  $V/V_{th}$  at four different pretilt angles,  $\alpha = 1^\circ, 2^\circ, 3^\circ$ , and  $5^\circ$ . From Wang, H., *Studies of Liquid Crystal Response Time*, Ph.D. dissertation Department of Electrical and Computer Engineering in the College of Engineering and Computer Science the University of Central Florida, Orlando, Florida. (Report 30)

Thus we have shown a relation of the angle,  $\theta$ , between the electric field,  $\mathbf{E}$ , and the electric displacement,  $\mathbf{D}$ , adequately described in the geometric algebra description of electromagnetism to the angle,  $\theta$ , defined with respect to a unit vector angle of incident radiation and to media with induced dipoles. The latter is related to the optical response times ( $T_{rise}$  and  $T_{decay}$ ) that are linearly proportional to media director reorientation times ( $t_{rise}$  and  $t_{decay}$ ).

## **7.0 SELF-INDUCED TRANSPARENCY (SIT), ELECTROMAGNETICALLY-INDUCED TRANSPARENCY (EIT) and POLMOD**

### **7.1 SIT**

*Self-induced transparency* is defined as follows:

"Above a critical power threshold for a given pulse width, a short pulse of coherent traveling-wave optical radiation is observed to propagate with anomalously low energy loss while at resonance with a two-quantum-level system of absorbers. The line shape of the resonant system is determined by inhomogeneous broadening, and the pulse width is short compared to dissipative relaxation times. A new mechanism of self-induced transparency, which accounts for the low energy loss, is analyzed in the ideal limit of a plane wave which excites a resonant medium with no damping present. The stable condition of transparency results after the traversal of the pulse through a few classical absorption lengths into the medium. This condition exists when the initial pulse has evolved into a symmetric hyperbolic-secant pulse function of time and distance, and has the area characteristic of a "2 $\pi$  pulse." Ideal transparency then persists when coherent induced absorption of pulse energy during the first half of the pulse is followed by coherent induced emission of the same amount of energy back into the beam direction during the second half of the pulse. The effects of dissipative relaxation times upon pulse energy, pulse area, and pulse delay time are ... to first order in the ratio of short pulse width to long damping time. The analysis shows that the 2 $\pi$  pulse condition can be maintained if losses caused by damping are compensated by beam focusing." (McCall & Hahn, 1969)

Self-induced transparency (SIT) of propagating coherent light pulses in absorbing media (McCall & Hahn, 1965, 1967, 1969; Lamb, 1971) is now well proven. SIT has been demonstrated in gases, e.g., in gaseous SF<sub>6</sub> and SF<sub>6</sub>-He (Patel & Slusher, 1967). In the case of gases, the molecular dephasing relaxation time is longer than the pulse temporal length.

### **7.2 EIT**

Another induced transparency effect is *Electromagnetically-induced transparency* (EIT), which is a coherent optical nonlinearity that renders a medium transparent over a narrow spectral range within an absorption line. Extreme dispersion is also created within this transparency "window" which leads to "slow light" (Kocharovskaya & Khanin, 1986).

Observation of EIT involves two optical fields (highly coherent light sources, such as lasers) which are tuned to interact with three quantum states of a material. The "probe" field is tuned near resonance between two of the states and measures the absorption spectrum of the transition. A much stronger "coupling" field is tuned near resonance at a different transition. If the states are selected properly, the presence of the coupling field will create a spectral "window" of transparency which will be detected by the probe. The coupling laser is sometimes referred to as the "control" or "pump", the latter in analogy to incoherent optical nonlinearities such as spectral hole burning or saturation.

EIT is based on the destructive interference of the transition probability between atomic states. Closely related to EIT are coherent population trapping (CPT) phenomena. EIT requires a coherently prepared media which has long quantum memory. The mechanism underlying EIT is described in the following protocol:

“...one applies two laser wavelengths whose frequencies differ by a Raman (non-allowed) transition of the medium...the electrons must be stopped from moving at the frequencies of the applied fields. If the electrons do not move, then they do not contribute to the dielectric constant. Non-movement will occur if, at each applied frequency, the electron is driven by two sinusoidal forces of opposite phase... In quantum mechanical terms... what happens is that the probability amplitude of ... a state is driven by two terms of equal magnitude and opposite sign. One driving term is proportional to the probability amplitude of the ground state. The other terms is oppositely phased and proportional to the probability amplitude of a third state and the expected value of the amplitude of the sinusoidal motion at each of the applied frequencies is zero.” (Harris, 1997)

The difference between EIT and SIT is that in the case of SIT only a single pulse is required whose area is  $2\pi$  and only a ground and an excited state are involved (Fig 7.2.1).

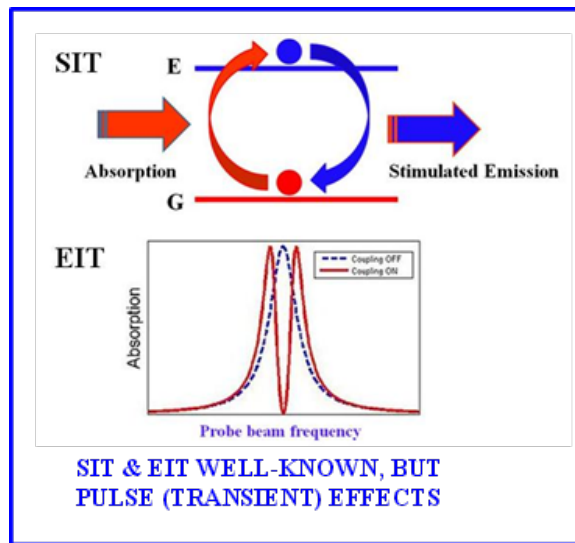


Fig 7.2.1 SIT and EIT mechanisms.

### 7.3 POLMOD

Polarization modulation induced transparency addresses the mechanisms also addressed by SIT, although but achieves transparency with a continuous (modulated) wave so that polarization dipole matching or polarization compatibility is less than the dephasing relaxation time.

Both SIT and POLMOD achieve excitation durations that are less than the relaxation time of a detector or medium: SIT in the sense of the exciting pulse being shorter in duration than the relaxation time of a medium; POLMOD in the sense of the polarization compatibility of the exciting cw wave with induced dipoles being of duration, again, less than the relaxation time of the medium. The great advantage of POLMOD is that beams of any duration can be used, whereas SIT is restricted to short, area  $2\pi$ , pulses carrying much less energy, as well being more difficult to generate.

The selectivity of induced dipoles to linear versus circular polarization in solid state media was reported by the principal investigator (Barrett et al, 1983; Barrett, 1983; Barrett, 1987a-c).

The present project extended the POLMOD approach to dielectric media with the objective of defeating atmospheric/ionospheric propagation losses.

## 8.0 REFERENCES

Allen, L., Beijersbergen, M.W., Spreeuw, R.J.C. & Woerdman, J.P., Orbital angular momentum of light and the transformation of Laguerre-Gaussian laser modes. *Physical Review A*, 45, 8185-9, 1992.

Allen, L. & Padgett, M.J., The Poynting vector in Laguerre-Gaussian beams and the interpretation of their angular momentum density. *Optics Communications*, 184, 67-71, 2000.

Arthur, J.W., *Understanding Geometric Algebra for Electromagnetic Theory*, Wiley IEEE Press, 2011.

Barrett, T.W., Modulation of electrical conductance of phthalocyanine films by circularly polarized light. *Thin Solid Films*, 102, 231-244, 1983.

Barrett, T.W., Wohltjen, H., and Snow, A., A new method of modulating electrical conductivity in phthalocyanines using light polarization. Chapter 24, pp. 475-505 in *Molecular Electronic Devices II*, F.L. Carter (ed), Marcel Dekker, New York, NY, 1987a.

Barrett, T.W., Physical Properties of Ordered Ultrathin Organic Films. NSF Workshop "The Molecular Engineering of Ultrathin Polymeric Films", University of California at Davis, *Thin Solid Films*, 152, 67-98, 1987b.

Barrett, T.W., Physical properties of ordered ultrathin organic films. Chapter 5, pp. 67-98 in P. Stroeve & E. Ranses (eds) *Molecular Engineering of Ultrathin Polymeric Films*, Elsevier, New York, 1987c.

Barrett, T.W., A Polarization-Rotation Modulated, Spread Polarization-Rotation, Wide-Bandwidth Communications System. U.S. Patent 5,592,177 dated January 7th, 1997.

Barrett, T.W., Topology and the physical properties of the electromagnetic field. *Apeiron* 7, 3-11, 2000.

Barrett, T.W., Topological foundations of electromagnetism. *Annales de la Fondation Louis de Broglie*, special edition: *en hommage à George Lochak pour son 70ème anniversaire*, 26, 55-79, 2001.

Barrett, T.W., Topological approaches to electromagnetism. Pp. 699-734 in M. Evans (Ed.) *Modern Nonlinear Optics*, 2<sup>nd</sup> edition, Wiley Interscience, NY, 2001.

Barrett, T.W., *Topological Foundations of Electromagnetism*, World Scientific, 2008.

Barrett, T.W., Wohltjen, H., and Snow, A., A new method of modulating electrical conductivity in phthalocyanines using light polarization. *Nature*, 301, 694-5, 1983.

Barron, L.D., pp. 271-331, Chap. 6 in R.J.H. Clark & R.E. Hester (eds) *Advances in Infrared and Raman Spectroscopy*, Vol 4, Heyden, London, 1978.

Barron, L.D., *Molecular Light Scattering and Optical Activity*, Cambridge U Press, 1982.

Baylis, W.E., *Electrodynamics: A Modern Geometric Approach*, Birkhäuser, Boston, 1999.

Beth, R.A., Mechanical detection and measurement of angular momentum of light. *Physical Review*, 50, 115-125, 1950.

Bloch, F. Nuclear induction. *Phys. Rev.* 70, 7-8, 1946.

Buckingham, A.D., Permanent and induced molecular moments and long-range intermolecular forces. *Adv. Chem. Phys.*, 12, 107-142, 1967.

Chappel, J.M., Drake, S.P., Seidel, C.L., Gunn, L.J., Iqbal, A., Allison, A. & Abbott, D., Geometric algebra for electrical and electronic engineers. *Proc. IEEE*, 102, 1340-1363, 2014.

Child, M.S. & Longuet-Higgins, H.C., *Phil. Trans. Roy. Soc.*, A254, 259, 1961.

Chisholm, J.S.R. & Common, A.K., *Clifford Algebras and Their Applications in Mathematical Physics*, NATO Advanced Science Institutes Series, Reidel, 1986.

Djordjevic, I.B., Deep-space and near-Earth optical communications by coded orbital angular momentum (OAM) modulation. *Optics Express*, 19, 14277-14289, 2011.

Djordjevic, I.B. & Arabaci, M., LDPC-coded orbital angular momentum (OAM) modulation for free-space optical communication. *Optics Express*, 18, 24722-24728, 2010.

Djordjevic, I.B. & Djordjevic, G.T., On the communication over strong atmospheric turbulence channels by adaptive modulation and coding. *Optics Express*, 17, 18250-18262, 2009.

Djordjevic, I.B., Vasic, B. & Neifeld, M.A., LDPC coded OFDM over the atmospheric turbulence channel. *Optics Express*, 15, 6336-6350, 2007.

Doran, C. & Lasenby, A., *Geometric Algebra for Physicists*, Cambridge U Press, 2003.

Erickson, J.L., Conservation laws for liquid crystals, *Trans. Soc. Rheol.* **5**, 23 (1961).

Fiutak, J., *Can. J. Phys.*, 41, 12, 1963.

Gibson, G., Courtial, J., Padgett, M., Vasnetsov, M., Pas'ko, V., Barnett, S. & Franke-Arnold, S., Free-space information transfer using light beams carrying orbital angular momentum, *Opt. Express* 12, 5448-5456, 2004.

Göppert-Mayer, M., Über Elementarakte mit zwei Quantensprüngen. *Ann. Physik*, 9, 273-294, 1931.

Harris, S.E., Electromagnetically induced transparency. *Physics Today*, 50, 7, July, 36-42, 1997.

Herzfeldt, K.F. & Göppert-Mayer, M., On the theory of dispersion. *Phys. Rev.*, 49, 332-339, 1936.

Hestenes, D. & Sobczyk, G., *Clifford Algebra to Geometric Calculus*, Reidel, 1984.

Hirschfelder, J.O., Curtiss, C.F. & Bird, R.B., *Molecular Theory of Gases and Liquids*, Wiley, 1954.

Irvine, W.T.M, Linked and knotted beams of light, conservation of helicity and the flow of null electromagnetic fields. *J. Phys. A: Math. Theor.* 43 385203, 1-9, 2010.

Irvine, W.T.M. & Bouwmeester, D., Linked and knotted beams of light. *Nature Physics*, 4, 716-720, 2008.

Kedia, H., Bialynicki-Birula, I., Peralta-Salas, D. & Irvine, W.T.M., Tying Knots in Light Fields. *Phys. Rev. Lett.*, PRL 111, 150404, 2013.

Khoo, I.C. & Wu, S.T., *Optics and Nonlinear Optics of Liquid Crystals*, World Scientific, Singapore, 1993.

Kleckner, D. & Irvine, W.T.M., Creation and dynamics of knotted vortices. *Nature Physics*, 9, 253-8, 2013.

Kocharovskaya, O. & Khanin, Ya. I., *Sov. Phys. JETP*, 63, 945, 1986.

Kolmogorov, A.N. The local structure of turbulence in incompressible viscous fluid for very large Reynolds numbers. *Proceedings of the USSR Academy of Sciences* 30: 299-303, 1941a. (Russian), translated into English by V. Levin: Kolmogorov, Andrey Nikolaevich (July 8, 1991). "The local structure of turbulence in incompressible viscous fluid for very large Reynolds numbers". *Proceedings of the Royal Society A* 434 (1991): 9-13. Bibcode:1991RSPSA.434....9K. doi:10.1098/rspa.1991.0075.

Kolmogorov, A.N. Dissipation of Energy in the Locally Isotropic Turbulence. *Proceedings of the USSR Academy of Sciences* 32: 16-18, 1941b. (Russian), translated into English by Kolmogorov, Andrey Nikolaevich (July 8, 1991). "The local structure of turbulence in incompressible viscous fluid for very large Reynolds numbers". *Proceedings of the Royal Society A* 434 (1991): 15-17. Bibcode:1991RSPSA.434...15K. doi:10.1098/rspa.1991.0076.

Kolmogorov, A.N., A refinement of previous hypotheses concerning the local structure of turbulence in a viscous incompressible fluid at high Reynolds number. *J. Fluid Mech.*, 13, 82-85, 1962.

Lamb, G.L., Jr., Analytic descriptions of ultrashort optical pulse propagation in a resonant medium. *Rev. Mod. Phys.*, 43, 99, 1971.

Leach, J., Courtial, J., Skeldon, K., Barnett, S.M., Franke-Arnold, S. & Padgett, M.J., Interferometric methods to measure orbital and spin, or the total angular momentum of a single photon, *Phys. Rev. Lett.* **92**, 013601, 2004.

Leslie, F.M., Some constitutive equations for liquid crystals, *Arch. Ration. Mech. Anal.* **28**, 265-283 (1968).

Maier, W. & Meier, G., A simple theory of the dielectric characteristics of homogeneous oriented crystalline-liquid phases of the nematic type, *Z. Naturforsch. Teil A* **16**, 262 (1961).

Matos, S.A., Ribeiro, M.A. & Paiva, C.R., Anisotropy without tensors: a novel approach using geometric algebra. *Optics Express*, 15, 15175-15186, 2007.

Maxwell, J.C., *A Treatise on Electricity and Magnetism*, Volume 2, 1873 (Dover, New York, 1954).

McCall, S.L. & Hahn, E.L., *Bull. Am. Phys. Soc.*, 10, 1189, 1965.

McCall, S.L. & Hahn, E.L., Self-induced transparency by Pulsed Coherent Light, *Phys. Rev. Lett.*, 18, 908-911, 1967.

McCall S.L. & Hahn, E.L., Self-induced transparency. *Physical Review*, 183, 457-485, 1969.

McClain, W.M., Polarization dependence of three-photon phenomena for randomly oriented molecules. *J. Chem. Phys.*, 57, 2264-2272, 1972.

Milner, V. & Prior, Y., Biaxial spatial orientation of atomic angular momentum, *Phys. Rev. A* **59**(3), R1738, 1999.

Milner, V., Chernobrod, B.M. & Prior, Y., Arbitrary orientation of atoms and molecules via coherent population trapping by elliptically polarized light", *Phys. Rev. A* **60**(2), 1293, 1999.

Mortensen, S. & Hassing, S., pp. 1-60 in *Advances in Infrared and Raman Spectroscopy*, Vol. 6, R.T.H. Clark & R.E. Hester (eds), Heyden, London, 1980.

Mortensen, S. & Konigstein, J.S., *J. Chem. Phys.*, 48, 3971, 1968.

Obukhov, A.M., Some specific features of atmospheric turbulence. *J. Fluid Mech.*, 13, 77-81, 1962.

Oesch, D.W. & Sanchez, D.J., Creating well-defined orbital angular momentum states with a random turbulent medium. *Optics Express*, 20, 12292-12302, 2012.

Oesch, D.W. & Sanchez, D.J., Tewksbury-Christle, C.M., Aggregate behavior of branch points – persistent pairs. *Optics Express*, 2-, 1046-1059, 2012.

Oesch, D.W., Sanchez, D.J., Gallegos, A.L., Holzman, J.M., Brennan, T.J., Smith, J.C., Gibson, W.J., Farrell, T.C. & Kelly, P.R., Creation of photonic orbital angular momentum by distributed volume turbulence. *Optics Express*, 21, 5440-5, 2013.

Patel, C.K.N. & Slusher, R.E., Self-induced transparency in gases. *Phys. Rev. Lett.*, 19, 1019-1022, 1967.

Paterson, C. Atmospheric turbulence and orbital angular momentum of single photons for optical communication, *Phys. Rev. Lett.* 94, 153901, 2005.

Plazcek, G., in *Rayleigh and Raman Scattering*, UCRL Trans. No. 526L, *Handbuch der Radiologie* (E. Marx, ed.) Leipzig, Akademische Verlagsgesellschaft VI, 2, 209, 1934.

Primmerman, C.A., Price, T.R., Humphreys, R.A., Zollars, B.G., Barclay, H.T. & Herrmann, J. Atmospheric-compensation experiments in strong-scintillation conditions. *Applied Optics*, 34, 2081-2088, 1995.

Rañada, A.F., A topological theory of the electromagnetic field. *Letters in Mathematical Physics*, 18, 97-106. 1989.

Rañada, A.F., Knotted solutions to the Maxwell equations in vacuum. *J. Phys. A: Math. Gen.* 23, L815-L820, 1990.

Rañada, A.F., On the magnetic helicity. *Eur. J. Phys.*, 13, 70-76, 1992a.

Rañada, A.F., Topological electromagnetism. *J. Phys. A: Math. Gen.* 25, 1621-1641, 1992b.

Rañada, A.F., Interplay of topology and quantization: topological energy quantization in a cavity. *Physics Letters A* 310, 434-444, 2003.

Rañada, A.F. & Trueba, J.L., Electromagnetic knots. *Physics Letters A* 202, 337-342, 1995.

Rañada, A.F. & Trueba, J.L., Ball lightning an electromagnetic knot? *Nature*, 383, 32, 1996.

Rañada, A.F. & Trueba, J.L., Two properties of electromagnetic knots. *Physics Letters*, 232, 25-33, 1997.

Rañada, A.F. & Trueba, J.L., A topological mechanism of discretization for the electric charge. *Physics Letters*, B 422, 196-200, 1998.

Rañada, A.F. & Trueba, J.L., Topological electromagnetism with hidden nonlinearity. In *Modern Nonlinear Optics, Part 3, Second Edition, Advances in Chemical Physics, Volume 119*, Myron W. Evans (Ed), John Wiley, 2001.

Sanchez, D.J. & Oesch, D.W., Localization of angular momentum in optical waves propagating through turbulence. *Optics Express*, 19, 25388-25396, 2011a.

Sanchez, D.J. & Oesch, D.W., Orbital angular momentum in optical waves propagating through distributed turbulence. *Optics Express*, 19, 24596-24608, 2011b.

Wang, H., *Studies of Liquid Crystal Response Time*. Ph.D. dissertation, Department of Electrical and Computer Engineering, University of Central Florida, Orlando, Florida, 2005.